Binary Nano-structuring: Concept, Strategies, Features and Devices

Dissertation

zur Erlangung des Doktorgrades

Dr. rer. nat.

vorgelegt der
Fakultät für Mathematik und Naturwissenschaften der
Technischen Universität Ilmenau

von
M. Sc. Liaoyong Wen
Ilmenau

TECHNISCHE UNIVERSITÄT
ILMENAU

Doktorvater und 1. Gutachter: Prof. Dr. Yong Lei
2. Gutachter: Prof. Dr. Gerhard Wilde
3. Gutachter: Prof. Dr. Heiko Jacobs

Tag der Einreichung: 20.10.2015
Tag der wissenschaftlichen Aussprache: 08.02.2016

urn: nbn: de: gbv: ilm1-2016000096

Abstract

Nanostructure arrays, composed by two subdivisions of ‘nanostructure’ and ‘array’, are the fundamental for many modern and future devices or systems. Binary nanostructure arrays, in which both of the ‘nanostructure’ and the ‘array’ can be freely manipulated and utilized, could raise a new horizon by introducing the interactions between the sub-arrays that are inaccessible for the single ‘array’s. A general technique is developed to fabricate diverse binary nanostructure arrays (e.g., nanowire/nanowire, nanotube/nanowire, nanotube/nanotube, nanodot/nanodot) with morphologic versatility and highly structural controllability for each of the sub-array individually. The key of this technique is based on a distinctive binary-pore anodic aluminum oxide template, possessing double side barrier oxide layers located at the opposite sides of the template. Under the same mechanism, the template can be further upgraded to multi-pore template (e.g., ternary and quadruple) in one matrix with even higher pore densities and more morphologic options. The versatility of binary-nanostructuring is being explored to realize innovative devices, such as macroscopic ‘titanium dioxide/cuprous oxide’ Z-scheme photosynthesis unit and nanoscopic ‘zinc oxide/aluminum doped zinc oxide’ addressable vertical nanowire transistor. Furthermore, nanoengineering of single ‘array’s are conducted to pursuit high-performance supercapactior based on platinum/manganese oxide core/shell nanotube array and photoelectrochemical cell based on nano-gold/Pb(Zr,Ti)O_3 hybrid, in which the optimal structure and composition of the single ‘array’s could provide valuable guidance for addressing multi-functionalized devices based on the binary nanostructure arrays.

Zusammenfassung

Nanostrukturarrays, bestehend aus den zwei Unterteilungen „Nanostruktur“ und „Array“, sind elementar für viele moderne und zukünftige technologische Anwendungen oder Systeme. Binäre Nanostrukturarrays, in denen beide, die „Nanostruktur“ und die „Array“, unabhängig voneinander eingestellt und genutzt werden können, könnten einen neuen Horizont durch Interaktionen zwischen den Sub-Arrays, welche unter Einfach-Arrays unzugänglich sind, eröffnen. Eine allgemeine Methode wird entwickelt um verschiedene Nanostrukturarrays (z.B. Nanowire/Nanowire, Nanotube/Nanowire, Nanotube/Nanotube, Nanodot/Nanodot) mit struktureller Flexibilität und hoher Steuerbarkeit für jedes der Sub-Arrays individuell herzustellen. Der Schlüssel zu dieser Methode basiert auf den charakteristischen binären Poren von anodischen Aluminium Templaten, welche beidseitig entgegengesetzte Barriere-Oxid-Schichten besitzen. Mittels desselben Mechanismus kann das Templat zu einem Viel-Array-Templat (z.B. dreifach oder vierfach) in einer Matrix mit noch höheren Porendichten und weiteren morphologischen Möglichkeiten erweitert werden. Die Vielseitigkeit der binären Nanostrukturierung wird untersucht für die Realisierung innovativer Anwendungen, wie zum Beispiel makroskopische Titandioxid/Kupfer(I)-oxid Z-Schema Photosyntheseeinheiten und nanoskopisch große adressierbare Zinkoxid/Aluminiumzinkoxid vertikale Nanodraht-Transistoren. Des Weiteren wird Nanoengineering von Einfacharrays durchgeführt, dazu werden leistungsstarke Superkondensatoren basierend auf Platin/Manganoxid-Core/Shell-Nanotubearrays und photoelektrochemische Zellen basierend auf Nano-Gold/Pb(Zr,Ti)O_3 Hybriden nachgegangen durch welche die optimale Struktur und Zusammensetzung der Einfacharrays wichtige Informationen für multifunktionale Anwendungen basierend auf binären Nanostrukturarrays liefern.

Acknowledgement

This work was carried out from January 2012 to September 2015 under the supervision of Prof. Dr. Yong Lei at the Institute of Physics and the Institute of Micro- and Nanotechnologies (IMN MacroNano®), Technische Universität Ilmenau.

First and foremost, I wish to acknowledge and deeply thank my advisor, Prof. Dr. Yong Lei for his steadfast encouragement, guidance, and support during my academic research in his group. He has been actively supervised my projects and has always provided fruitful advice when the projects face dilemmas. Besides the academic matters, he also has encouraged me to be more positive in lab management and communication during the conferences, as well as participating more teaching activities. I sincerely thanks for the enjoyable and precious experiences and memories that I shared together with him in the past four years.

Moreover, I would like to thank all the colleagues from our group for their kind help in the aspects of not only academic matters but also everyday life in Ilmenau. My special thanks to Mrs. Yan Mi for her help about the ALD technique, and also the collaboration work related to parts of the Binary nanostructures, Supercapacitor, and PEC. Many thanks to Mr. Rui Xu, Dr. Zhijie Wang, and Dr. Dawei Cao for the collaboration work related to parts of the Binary nanostructures and PEC projects. Many thanks to Dr. Huaping Zhao, Mr. Fabian Grote, Dr. Chengliang Wang, Mr. Yaoguo Fang, Mr. Max Sommerfeld, Dr. Min Zhou, Dr. Yang Xu, Ms Liying Liang, Mr. Ahmed Shukur Hameed Al-Haddad, Mrs Moumou Li and Mr. Stefan Bösemann for their fruitful discussions, exchange of ideas, and many kinds of technique support. It was a great pleasure to work in such an active atmosphere group. Priceless memories shared with each of you will be in my heart for the rest of my life.

For the FIB, Ion milling, EBL and MTSTM systems, I want to thank Dr. Henry Romanus, Ms. Diana Roßberg, Mrs. Elvira Remdt, Prof. Dr. Heiko Jacobs, Mr. Lars Hiller, Prof. Dr. Thomas Hannappel and Mr. Weihong Zhao for their effort and precious time. I also want to

thank Prof. Dr. Puxian Gao for the help of TEM measurements as well as the invaluable discussion and suggestion during his visit in our group.

Moreover, I want to thank Prof. Dr. Changming Li from the Southwest University for inviting me into his group. The welcoming atmosphere has inspired me and the collaborating work has resulted in excellent scientific results. It was also a precious and unforgettable experience to have a few times of fruitful discussions with Prof. Dr. Zhonglin Wang from Georgia Institute of Technology and Prof. Dr. Shu-Hong Yu from the University of Science and Technology of China.

Finally, I would like to thank my dear family members for their supports and sacrifices shown not only through my PhD studies but also the moment I am not recognized during my life.

Table of Content

List of Figures

List of Abbreviations

AAO	anodic aluminum oxide
ALD	atomic layer depostion
AZO	aluminum doped zinc oxide
BCP	block copolymer
CA	cyclic anodization
CdS	cadmium sulfide
Cu_2O	cuprous oxide
C cm^{-3}	volumetric energy capacity
CVD	chemical vapor deposition
CV	cyclic voltammetry
CS	core/shell
D_{int}	interpore distance
D_p	pore diameter
DL	diffusion length
DEZn	diethylzinc
E	electric field
EBL	electron beam lithography
ED	electrochemical deposition
EDX	energy-dispersive detector X-rays
EDLS	electrical double-layer supercapacitors
E_{DP}	depolarization electric field
ES	electrochemical supercapacitors
FDTD	finite difference time domain
FS	faradaic supercapacitors
j	current density
J-V	current–voltage
HA	hard anodization
IPCE	incident photon to charge carrier efficiency
j_{limit}	limiting current
LIL	laser interference lithography
MA	mild anodization
MIM	metal/insulator/metal
MTSTM	multi-tip scanning tunneling microscopy
MnO_2	manganese oxide

NIL	nanoimprint lithography
NT	nanotube
P	porosity
PA	pulse anodization
PBR	Pilling Bedworth ratio
PDMS	poly-dimethylsiloxane
PEC	photoelectrochemical
$Pt(MeCp)Me_3$	trimethyl(methylcyclopentadienyl)platinum(IV)
PZT	ferroelectric $Pb(Zr,Ti)O_3$
R	series resistance
SEM	scanning electron microscopy
$SnCl_4$	tin (IV) chloride
T	temperature
TEM	transmission electron micrograph
TE	thermal evaporation
t_b	barrier layer thickness
t_w	pore wall thickness
$TiCl_4$	titanium (IV) chloride
TMAl	trimethylaluminum
U	anodizing potential
UV-Vis	ultraviolet–visible spectroscopy
UTAM	ultra-thin alumina mask
ρ_p	pore density
1D	One-dimensional

1 Introduction

As nanotechnologies progressing, a series of nanostructure arrays can be fabricated by 'top-down' and 'bottom-up' approaches in a large scale and has been widely adopted in nearly every kind of nano-devices or -systems, including photonics,[1] metamaterials,[2] electronics,[3] optoelectronics,[4] piezoelectric,[5, 6] energy conversions,[7-9] and energy storages.[10-12] The entire nanostructure arrays are composed by two subdivisions of 'nanostructure' and 'array'. For the 'nanostructure', intensive investigations have been conducted for the desirable purpose, such as the nanoparticles,[2] nanowires,[1, 5-7] or nanotubes[10, 12] with different materials, sizes, and crystal orientation. Furthermore, for the trend of multi-functional integration, advanced 'nanostructures', like core/shell[3, 9, 11] and heterojunction,[4] are successfully explored by a few high-resolution techniques. However, though all those great progresses, the other key subdivision of 'array' is barely touched because of technique constraints. Therefore, the nanostructure arrays only contain unchangeably single 'array' in one matrix, in other words, all components inside the matrix are identical or similar from each other.

Binary nanostructure arrays, which comprise two sets of spatially discernable sub-arrays in one matrix, could raise a new horizon by releasing the unchangeable subdivision of 'array'. Thereby, taking the interactions between each other, both of the sub-arrays can work simultaneously as functional components, or as controlling and functional components, respectively. For instance, binary metal arrays, benefiting from the coupling effects between each other, could possess additive effects or exotic optical properties.[13, 14] On the other hand, binary semiconductor arrays, introducing additional band gaps to widen the spectral absorption range, could be beneficial for solar cells and photodectors, or that with one suitable p type and one suitable n type could be favorable to act a wireless artificial photosystem that generates H_2 and O_2 simultaneously.[15, 16] Furthermore, by integrating the advanced 'nanostructure' in each sub-array, more superior devices are highly expected.

Considering all those benefits, few 'top down' and 'bottom up' fabrication techniques are exploited recently, such as two-step electron beam lithography (EBL),[14] angle-resolved colloidal lithography[13, 17-19] and two-step block copolymer (BCP).[20] Unfortunately, all of them are limited to certain types of processes, materials, and always result in zero-dimensional binary nanostructure arrays.

The anodic alumina oxide (AAO) template, taking the advantages of cost-effective and scalable process, has been widely used to prepare ordered nanostructure arrays from low-aspect ratio nanoparticle arrays[21-28] to high-aspect ratio nanowire,[29-31] nanotube[32-34] and nanopore arrays.[35, 36] Furthermore, the advanced AAO templates with complex nanopore structures and the resultant nanostructures were obtained with careful engineering of `mild anodization´ and `hard anodization´,[37, 38] and on the other hand, the complex heterogeneous 'nanostructures' were also synthesized with the assistance of on-wire lithography,[39-52] coaxial lithography,[53] or other methods.[36, 54] Notwithstanding that, the AAO template and the accordingly nanostructure arrays are still restricted to single 'array's. The key barriers to realize binary nanostructure arrays with flexible material options and tailor-made of dimensions are still beyond the current techniques.

One major aim of this dissertation is to develop a general technique for realizing binary nanostructure arrays, in which both of the 'nanostructure' and the 'array' can be freely manipulated and utilized. The key achievements in this dissertation include the following aspects:

(1) Binary-pore AAO template, containing two sets of highly ordered pore arrays in one matrix, is successfully obtained in centimeter-scale. Owing to the distinctive double side barrier layers located at the opposite side of the template, the profile of each sub-pore array, such as the pore size and shape, can be modulated individually or simultaneously to a wide range.

(2) The mechanism of binary-pore template formation is being investigated in detail with microstructure analyzation and COMOSL simulation.

(3) High-throughput binary nanostructure (e.g., nanowire/nanowire, nanowire/nanotube, nanotube/nanotube, and nanodot/nandot) arrays are created with the assistance of binary-pore template combining with the well-established growth or deposition techniques.

(4) The evolution of AAO template from a single-pore array to a multi (ternary and quadruple)-pore array is being successfully demonstrated, which possesses even more morphologic options and higher pore densities.

(5) The versatility of the innovative technique could be utilized for preparing new devices by introducing the interactions between the sub-arrays, such as the macroscopic 'TiO_2/Cu_2O Z-scheme unit' based on binary functional-functional nanostructure arrays, and the nanoscopic 'addressable ZnO/AZO vertical nanowire transistor' based on binary controlling-functional nanostructure arrays.

(6) Nanoenginnering of single 'array's are conducted to pursuit high-performance supercapactior and PEC devices, in which the optimal structure and composition of the single 'array's could provide a useful guidance for achieving superior devices based on binary nanostructure arrays.

2 Background

2.1 General structure of AAO template

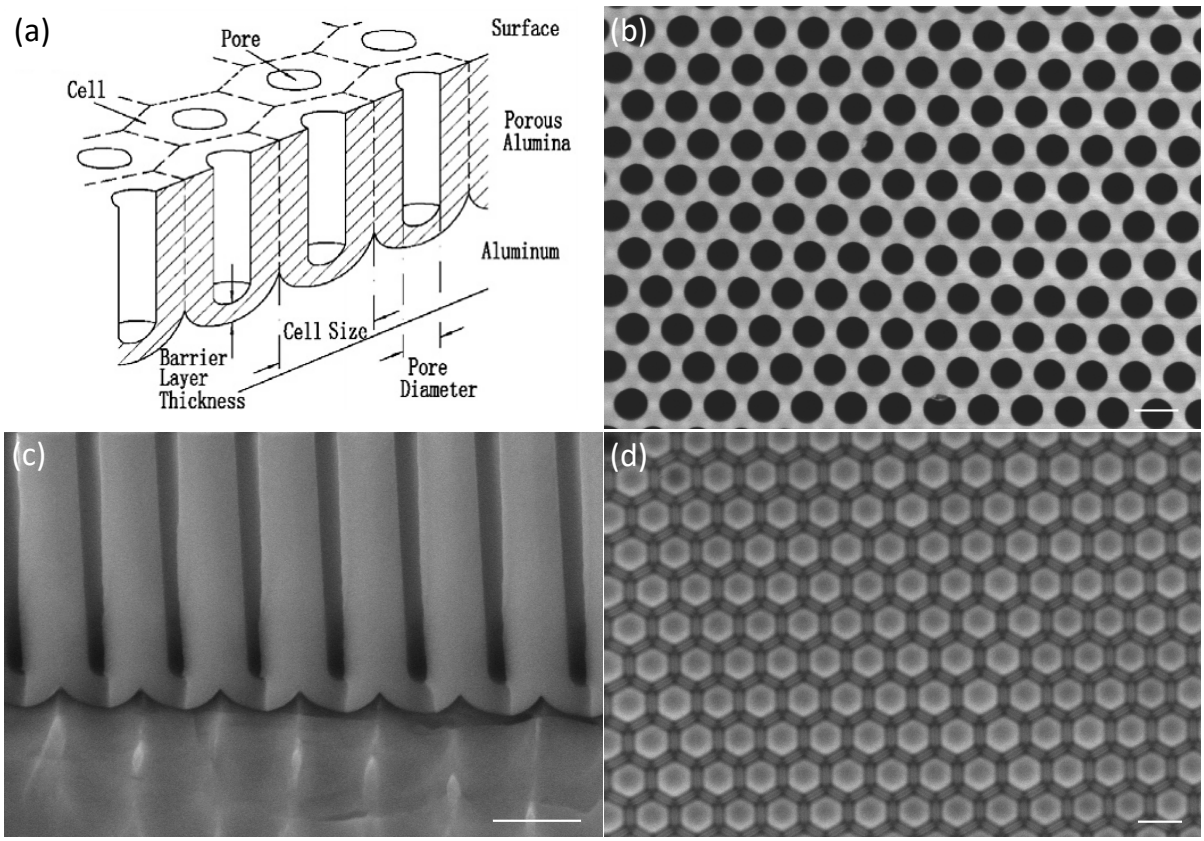

Figure 2-1. (a) Schematic structure of AAO template after the anodization on Al foil. SEM images of AAO template: (b) top surface, (c) barrier layer, and (d) bottom surface, respectively. Scale bar: 400 nm.

Figure 2-1 show a representative schematic structure of AAO template, together with scanning electron microscopy (SEM) images of key features of the AAO template, including top surface, barrier layer and bottom surface. AAO template has a large number of mutually honeycomb-like nanopores. Each cylindrical nanopore and its surrounding oxide constitute a hexagonal cell aligned normal to the metal surface. At the metal/oxide interface, a thin barrier oxide layer with an approximately hemispherical morphology closes the nanopore. Under proper anodization conditions, the oxide cells are self-organized to form a hexagonally close-packed structure. On the other hand, the surface of the aluminum after complete

removal of the porous oxide layer is textured with arrays of concave features. The thickness of the AAO template on aluminum is proportional to the total charge (Q_c) involved in the electrochemical oxidation. Therefore, the depth of nanopores is easily tunable from a few tens of nanometers up to hundreds of micrometers by controlling anodization time (t). In general, the structure of self-ordered AAO template is often defined by several structural parameters, such as interpore distance (D_{int}), pore diameter (D_p), barrier layer thickness (t_b), pore wall thickness (t_w), pore density (ρ_p), and porosity (P). For ideally ordered porous AAO, the following relationships can be drawn by simple geometric consideration:

$$D_{\text{int}} = D_p + 2t_w (\text{in nm}) \tag{2-1}$$

$$\rho_p = \left(\frac{2}{\sqrt{3} D_{\text{int}}^2} \right) \times 10^{14} cm^{-2} \tag{2-2}$$

$$P(\%) = \left(\frac{\pi}{2\sqrt{3}} \right) \left(\frac{D_p}{D_{\text{int}}} \right) \times 100 \tag{2-3}$$

These structural parameters of AAO template are known to be dependent on the anodizing conditions: the type of electrolyte, anodizing potential (U), current density (j), temperature (T), etc. Among those, anodizing potential (U) and current density (j) are the most important electrochemical parameters.[55]

2.2 Formation of AAO template

2.2.1 Initial-stage porous growth

In general, potentiostatic anodization is widely utilized for fabricating self-ordered porous AAO template, because of the linear dependence between the applied potential (U) and the structural parameters of the resultant AAO template. Figure 2-2a and 2-2b show a typical current (j) − time (t) curve for constant-potential anodization, and potential (U) − time (t)

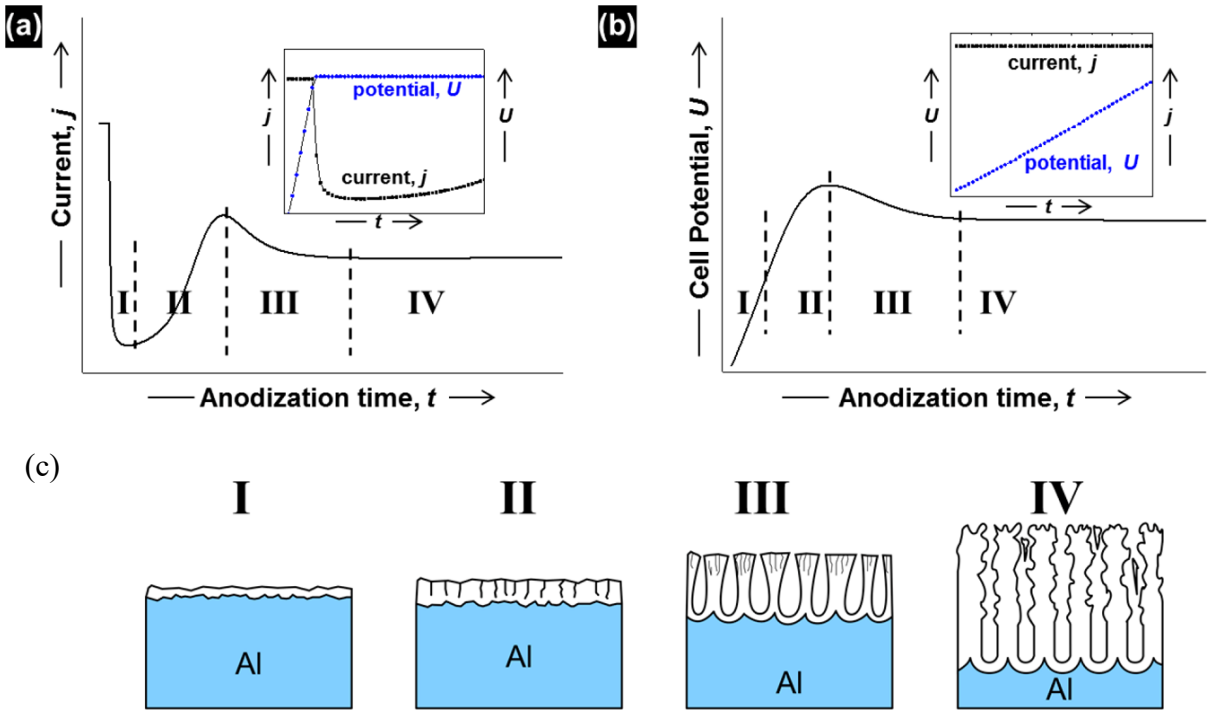

Figure 2-2. Schematic diagram of the kinetics of porous growth in potentiostatic (a): current (j) − time (t) curves, and galvanostatic (b): potential (U) − time (t) curve, together with stages of AAO template development (c). (Figures are taken from ref[55]).

curve for constant current anodization, together with schematic illustrations of the stages of porous structure formation (Figure 2-2c). When a constant-potential (U) is applied, a thin compact barrier oxide starts to grow over the entire aluminum surface (stage I). Thickening of the initial barrier oxide over time (t) results in an increase of series resistance (R) of the anodization circuit. Current (j) is initially maintained at the limiting current (j_{limit}) of the power supply, and correspondingly potential ($U = jR$) increases linearly with time (t) (see the inset of Figure 2-2a). When the thickness (or the resistance, R) of the compact barrier oxide layer reaches a certain value, current (j) drops rapidly to hit the minimum value (stage II). For this stage, O'Sullivan and Wood[56] suggested that current (i.e., electric field) concentrates on local imperfections (e.g., defects, impurity, pits) existing on the initial barrier oxide, resulting in non-uniform oxide thickening and pore initiation at the thinner oxide areas. Thompson and co-workers[57-59] have proposed that local cracking of the initial barrier oxide due to

accumulated tensile stress (PBR < 1) may develop the paths for electrolyte penetration. Local increase in field strength at the penetration paths effectively polarizes the Al−O bonds, facilitating field-assisted oxide dissolution there, and eventually leads to development of individual penetration paths into embryo pores.[59] Accordingly, further anodization leads to a gradual increase in current (j) to a local maximum due to the ready diffusion of electrolyte (stage III). After that, current (j) reaches a steady value after passing through an overshoot (stage IV). The appearance of current overshoot has been related to the decrease of the initial pore density with the steady-state growth of major pores: pores increase in size by persistent merging with adjacent pores.[60] For a given set of anodization conditions, the rate of potential increases at the very beginning of anodization, the value of the minimum current, the time needed for anodizing current to reach a steady value, and the appearance of the current overshoot has been known to be directly dependent on the anodizing potential (U), electrolyte pH and temperature, and the initial surface state of the aluminum.[60, 61]

For the case of galvanostatic anodization, a similar progression can be observed for stages I−IV, while the potential (U) changes as a function of time (Figure 2-2b). Under constant-current conditions, the oxide growth rate should be proportional to the applied current density (j) and constant according to the Faraday's law. In addition, a constant electric field ($E = U/t_b$) is required to sustain the applied constant current (j).[62] Accordingly, the potential (U) increases with the thickness of the growing barrier oxide (t_b), as shown in the inset of Figure 2-2b. However, in practice, the evolution of potential (U) deviates from a simple linear increase with time increasing (Figure 2-2b). For convenience, various mechanisms governing such a deviation have been referred to as growth instabilities, which include, for example, mechanical breakdown during zirconium anodization, and surface undulation/pore initiation during aluminum anodization.[63] Figure 2-2b shows a gradual retardation of potential (U) increase at stage II. Such a potential evolution can be attributed to a morphological

instability, that is, transition from the stage of barrier oxide growth to the stage of porous oxide growth.

2.2.2 Steady-state porous growth

Up to date, a few models are proposed to explain the porous development during the steady-state growth, such as, joule's heat-induced chemical dissolution, field-assisted oxide dissolution, average field model, direct cation ejection model, and oxide plastic flow.[55] Among them, the field-assisted oxide dissolution and oxide plastic flow are the most popular models, and the related details are briefly summarized as below.

2.2.2.1 Field-assisted oxide dissolution

Hoar and Mott[64] proposed that the thickness of the barrier layer is maintained by the dynamic rate balance between the following two processes occurring at the oxide electrolyte interface: (1) the oxide formation by the reaction between O^{2-} ions and Al^{3+} ions migrated from the metal/oxide interface, as in the formation of barrier-type oxide, and (2) the oxide dissolution. The author assumed that oxide formation takes place both at the metal/oxide interface and at the oxide/electrolyte interface, as in the barrier-type oxide formation. In their model, oxide at the oxide/electrolyte interface is decomposed to Al^{3+} and O^{2-} ions. The resulting Al^{3+} ions go into the electrolyte. Meanwhile, O^{2-} ions in contact with acid electrolyte become OH^- and move through the oxide to form new oxide at the metal/oxide interface. The proton (H^+) released by the oxide formation reaction would then diffuse back to the electrolyte by proton transfer between the lattice O^{2-} ions. Since the oxide ions from the oxide/electrolyte interface are spread over a larger area at the metal/oxide interface, the oxide dissolution occurs at a greater rate compared to oxide formation at the metal/oxide interface. In other words, the net result of process (2) is the progressive thinning of the barrier oxide layer due to the requirement of oxygen volume conservation in the oxide, which is

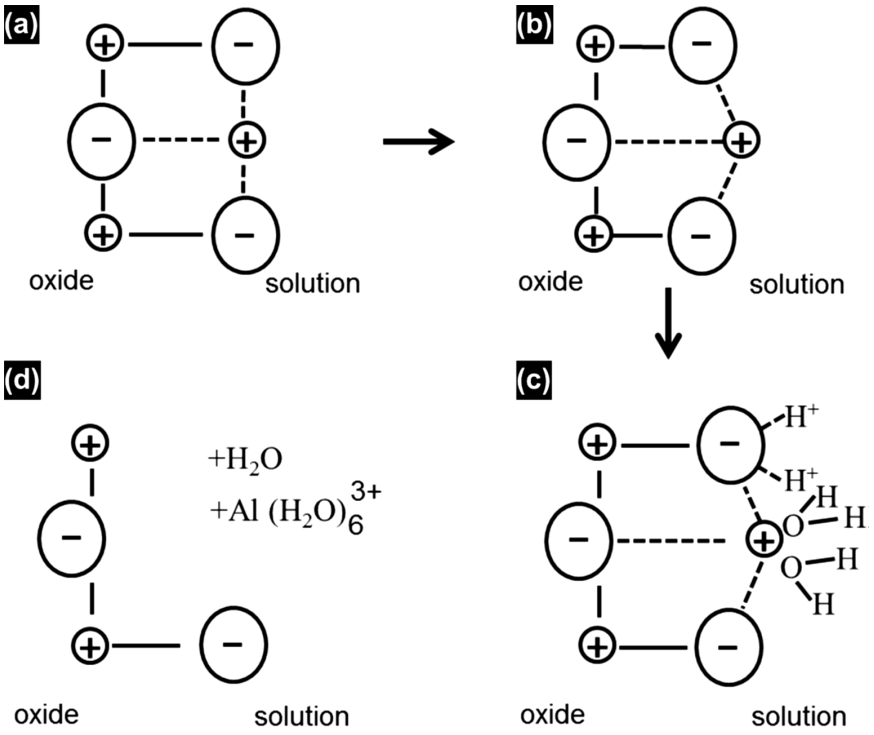

Figure 2-3. Schematics of field-assisted dissolution mechanism by O'Sullivan and Wood:[56] (a) before polarization, (b) after polarization, (c) removal of Al^{3+} and O^{2-} ions, and (d) remaining oxide. (Figures are taken from ref[56]).

compensated by the oxide formation through process (1) to keep the thickness of the barrier layer constant during electric field across the barrier oxide can effectively polarize (i.e., stretch) the Al−O bond along the applied field direction, lowering the effective activation energy for bond dissociation. Solvation of Al^{3+} ions by water molecules via activated complex (i.e., $Al(H_2O)_6^{3+}$) and the removal of O^{2-} ions by H_3O^+ ions as H_2O are facilitated. Because the electric field is concentrated on the pore base, the oxide dissolution rate is the greatest there, and a dynamic equilibrium between the oxide formation and the oxide dissolution can be established.[56] This model has popularly been cited in the literature to explain the growth and morphology of porous AAO.

2.2.2.2 Oxide plastic flow model

Skeldon et al.[65-68] have investigated the development of porous by performing tracer studies. They anodized Al/W-tracer/Al substrates (W-tracer layer; 3−5 nm thick, Al−30 at. % W,

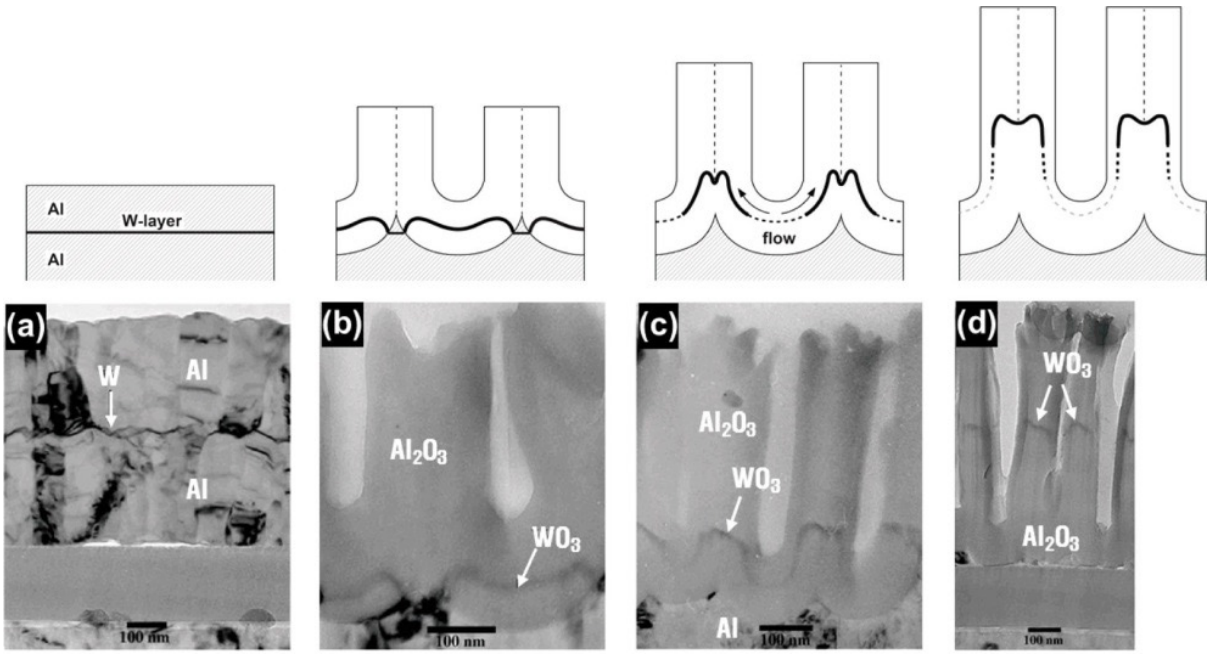

Figure 2-4. Cross-section transmission electron micrographs (TEM) of (a) the sputter-deposited aluminum containing a tungsten tracer layer, and following anodization for (b) 180 s, (c) 240 s, and (d) 350 s at 5 mA cm^{-2} in 0.4 M H_3PO_4 at 293 K. The distributions of tungsten tracer in anodic oxide are schematically illustrated above the respective TEM images. (Figures are taken from ref[65]).

Figure 2-4a) in H_3PO_4 solution and investigated the movement of the tracer band (WO_3) by TEM and RBS. During anodic oxidation, tungsten species incorporated into the anodic oxide migrated toward the oxide/electrolyte interfaces at about 0.38 of the rate of Al^{3+} ions. It was observed that the incorporated tracer band immediately beneath the pores initially lies slightly below the adjacent tracer near cell wall regions (Figure 2-4b). Upward displacement of the tracer band at the cell wall regions became pronounced upon further anodizations, as compared to the tracer below the pores, where the band is getting fainter because of a reduced tungsten concentration (Figure 2-4c, d). It was suggested that the fine-tungsten lines along the

cell boundaries beneath the tracer layer are associated with the tungsten enrichment in the aluminum adjacent to the aluminum/film interface, because formation of WO_3 requires higher Gibbs free energy as compared to Al_2O_3.[65] The authors pointed out that the observed behavior of the tracer band is contrary to what one would expect from the conventional dissolution-based model of porous AAO growth as follows. According to the conventional model of pore formation, tungsten tracer should be incorporated into the anodic oxide first at the regions immediately below the pores and then near the cell boundary regions because of the scalloped geometry of the barrier oxide layer. Thus, the tracer band at the pore regions should lie ahead of the tracer at the pore wall regions because of the outward migration of tungsten species, contrary to the experimental observations. If field assisted oxide dissolution occurred at the oxide/electrolyte interface, to maintain a constant t_b, a tungsten-rich layer with a sharp image contrast (instead of diminished contrast, as in Figure 4c) would have been observed by TEM at the pore bases due to preferential dissolution of Al^{3+} ions of a higher mobility in anodic oxide.

On the basis of the results of tracer experiments, Skeldon and co-workers[65, 66] proposed the flow mechanism of pore generation, as an alternative process to conventional field assisted oxide dissolution. According to the new model, the constant thickness of the t_b during porous AAO formation is maintained by viscous flow of oxide materials from the pore base to the cell boundary. It was suggested by the authors that the displacement of oxide materials is driven by large compressive stresses (~100 MPa) from electrostriction due to a high electric field ($E \approx 10^6$ V cm^{-1}) and also by volume expansion due to oxidation of aluminum, and that can be facilitated by the involvement of most of the oxide constituents in ionic transport (i.e., the plastic flow of oxide materials).

2.3 Milestone of AAO template development

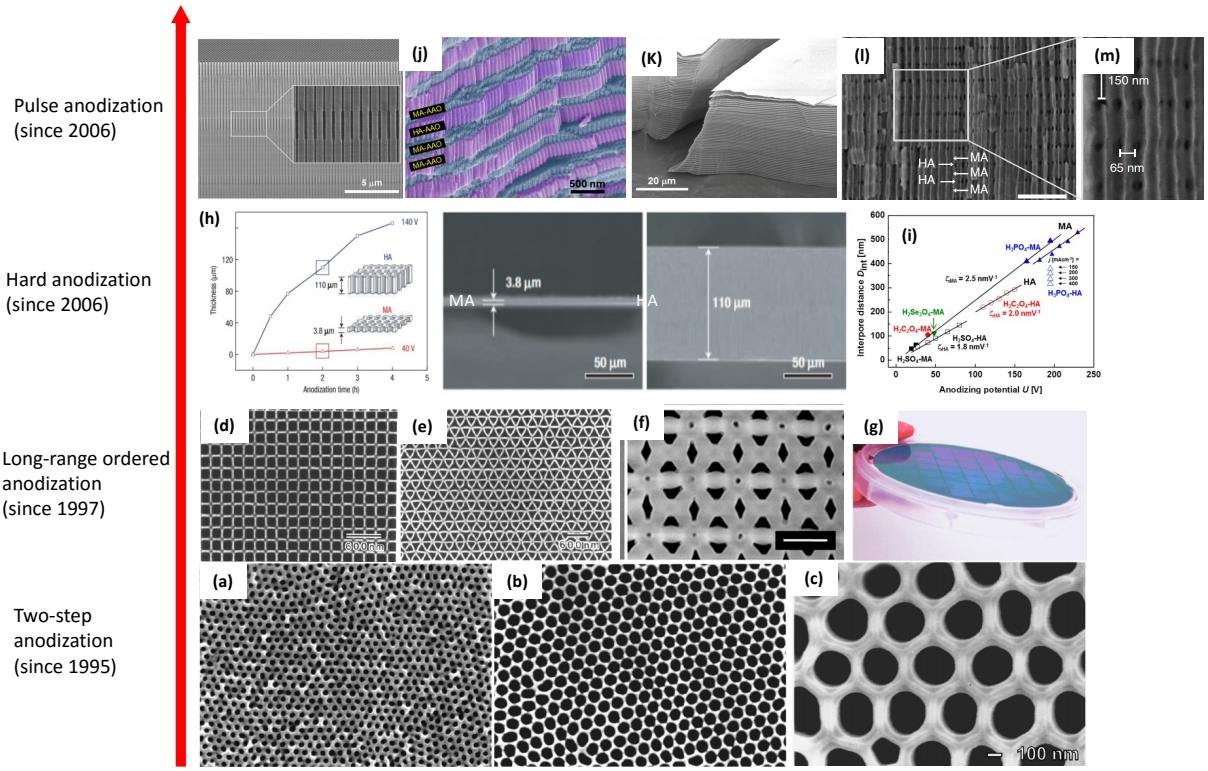

Figure 2-5. Summaries of the important development of AAO templates: (a-c) typical SEM images of AAO templates with the interpore distance from 50 to 420 nm;[69] (d-g) typical long-range ordered pore AAO templates with different arrangements (square, triangle, and hybrid circular-diamond-triangle);[70-72] (h) a comparison between HA and MA;[37] (i) Self-ordering regimes in MA (filled symbols) and HA (open symbols) by using H_2SO_4 (black symbols), $H_2C_2O_4$ (red symbols), H_2SeO_4 (green symbol), and H_3PO_4 (blue symbols);[55] (j) false-colored SEM images of AAO templates formed by H_2SO_4 PA and (k) 3D stacks of MA-AAO slabs;[38] (l) and (m) cross-sectional SEM images of a 3D AAO template.[73] (Figures are taken from [69],[70-72], [37], [55], [38], [73])

In 1995, Masuda and co-workers[74] developed the so-called 'two-step anodization' process, by which AAO template could be obtained with a highly ordered arrangement of uniform nanopores. In general, AAO template formed by two-step mild anodization (MA) process exhibits a polydomain structure. The lateral size of the defect-free domain increases with the

anodizing time, but is limited to several micrometers. Since the development of the two-step process from oxalic acid-based anodization, a lot of studies have been conducted not only to produce AAO template with different pore sizes and densities with an improved arrangement of pores, but also to understand the mechanism responsible for the growth and self-organizing behavior of pores during anodization. Particular efforts have been devoted to exploring the optimum conditions for pore ordering, mainly with sulfuric, oxalic, or phosphoric acid (Figure 2-5a to c).[69] Studies have indicated that the self-organized growth of ordered pores occurs within a relatively narrow window (known as the "self-ordering regime") of anodizing conditions.

For most nanotechnology applications, AAO template with uniform pore size and long-range ordering of pores are required. Masuda et al.[75] first reported fabrication of ideally ordered AAO template with a single-domain configuration over a few mm^2 area at 1997. The process involved pre-patterning of the aluminum surface by transferring the pattern of a hard SiC stamp (mold) onto the aluminum by mechanical pressure (i.e., nanoimprinting), followed by anodization. The SiC imprint stamps were fabricated with an array of convex features of desired arrangements in a limited dimension by electron beam lithography (EBL) technique. Each shallow indentation formed on the aluminum surface defined the position of pore growth by initiating pore nucleation at the initial stage of anodization, and thus led to a perfect arrangement of pores within the patterned area. Masuda et al.[70] further extended the method to fabricate pore array architectures with square- or triangle-shaped pore openings in square or triangular arrangements (Figure 2-5 d and e). Inspired by the work of Masuda and co-workers, several groups have developed various surface pre-patterning methods to fabricate single-domain AAO templates with tunable interpore distances (Figure 2-5f).[71, 76-82] Earlier research in this direction was mostly devoted to the development of an economic way of producing hard imprint stamps with large lateral dimensions. Surface pre-patterning

by mechanical nanoindentations using optical diffraction grating,[83] Si_3N_4 mold fabricated by deep-UV lithography,[77] wafer-scale Ni mold fabricated by laser interference lithography (LIL),[78] and self-assembled mono-or multi-layer of nanospheres[84] is effective in terms of process cost and pre-patterning area. Recently, soft lithography utilizing elastomeric poly-dimethylsiloxane (PDMS) stamp or nanoimprint lithography (NIL) on polymeric resist has been demonstrated as a versatile method for multiple transfers of a master pattern onto various substrates (Figure 2-5g).[72, 85]

Beside the mild anodization (MA), Lee et al.[37] showed that the self-ordering regimes can be extended by implementing hard anodization (HA) of aluminum (Figure 2-5h). The HA process was originally developed in the surface finishing industry in the early 1960s, and has been widely used for various industrial applications by taking advantage of the high-speed oxide growth (50-100 μmh^{-1}). However, the process has not been employed in current nanotechnology research due to the difficulties involved in controlling important structural parameters, such as pore size, interpore distance, and the aspect ratio of the nanopores of the resulting AAO template. By introducing a thin protective oxide layer on aluminum prior to performing HA process and carefully controlling the reaction heat during HA, Lee et al.[37] could suppress the burning event and grow self-ordered AAO template using oxalic acid at anodization potentials U > 100 V, establishing a new self-ordering regime with a widely tunable interpore distance (D_{int} = 200 - 300 nm). The rate of oxide growth in HA was found to be 25 to 35 times faster than that in MA. The newly developed method turned out to be applicable to other electrolyte systems.

By combing the conventional MA and the newly developed HA, pulse anodization (PA) was developed by Lee et al.,[37] which could offer a new degree of freedom for periodically modulating nanopore diameters along the pore axes of AAO template by taking the advantages of the two anodization processes. In their method, each step for modulation of

pore diameter required a tedious manual exchange of the anodizing electrolytes to satisfy both MA and HA conditions. In an attempt to avoid this problem, they have proposed an approach for continuous modulations of internal pore structure of AAO template by PA of aluminum under a potentiostatic condition using sulfuric or oxalic acid solution, in which a low potential and a high potential are alternately pulsed to achieve MA and HA conditions, respectively (Figure 2-5j).[38] The concept of structural engineering of AAO has been put forward by Losic et al.,[86] who developed a new anodizing process, called cyclic anodization (CA). They employed periodically oscillating current signals with different cyclic parameters (i.e., period, amplitude, and profile) during anodization of aluminum to achieve structural modulations in porous AAO template. Porous AAO template with modulated pores of different shapes (circular- or ratchet-type), diameters, and lengths were prepared by applying current signals of deliberately chosen cyclic parameters. Very recently, a well-defined and homogeneous periodic 3D nanotubular network was realized by a modified PA,[73] in which the voltage is maintained constant during MA steps, while during HA pulses the current is limited to a fixed value. This current limitation is responsible for the high uniformity of the 3D nanostructure over the macroscopic piece, which yields a real 3D ordered nanostructure (Figure 2-5 l and m).

During the last three decades, AAO template has been intensively exploited for synthesizing diverse nanostructure arrays in the forms of nanodots,[23-26, 28, 87-89] nanowires,[29-31, 90-97] nanotubes,[98-104] and nanopores.[105, 106] Such nanostructure arrays have already been applied in various fields including optics, electronics, optoelectronics and sensing. More importantly, AAO templates are also very efficient tool for realizing advanced heterogeneous 1D nanostructures that could have great advantages in energy conversion and storage applications.[107]

3 Designing principle and progress of heterogeneous 1D nanostructure arrays based on AAO template for energy applications

3.1 Designing principle of advanced heterogeneous 1D nanostructure arrays

The term 'heterogeneous 1D nanostructure array' generally consists of three distinctive features: structures with *1D nano-configuration*; *large-scale array*; *heterogeneous* 1D structure.[54]

First, the nanostructure should be confined to one dimension at nanoscale and a high aspect ratio is concomitantly yielded, indicating the coexistence of large surface-to-volume ratio and the longitudinal continuity of the materials. The large surface-to-volume ratio enables the relevant structure with a huge-area surface where the energy conversion/storage reactions could occur extensively and rapidly. The one unconfined dimension provides a continuous passway to efficiently transfer the charge carriers. In this case, the key disadvantage of short carrier diffusion length (DL) relative to the depth of visible light absorption in semiconductors could be well resolved (Left image in Figure 3-1a). For instance, the optical absorptivity of GaP near the band gap absorption is small and requires a minimal thickness of 28 μm for the bulk material to capture the light at 540 nm. The minority-carrier DLs in single crystalline GaP wafers are usually observed in the range of 10-100 nm, indicating a high possibility for photo-generated charge carriers in the bulk of GaP to recombine uselessly before travelling to surface and being collected.[108] When we transform the material configuration to 1D nanoscale, the photo-generated charge carriers just need to travel a short distance to the surface and the unconfined dimension of the structure can provide sufficient absorption of the incident light, besides the advantage of the absorption amplifying effect derived from the scattering and antireflection of 1D nanostructures. Consequently, the external quantum yield (at 500 nm) of the GaP PEC electrodes is dramatically enhanced

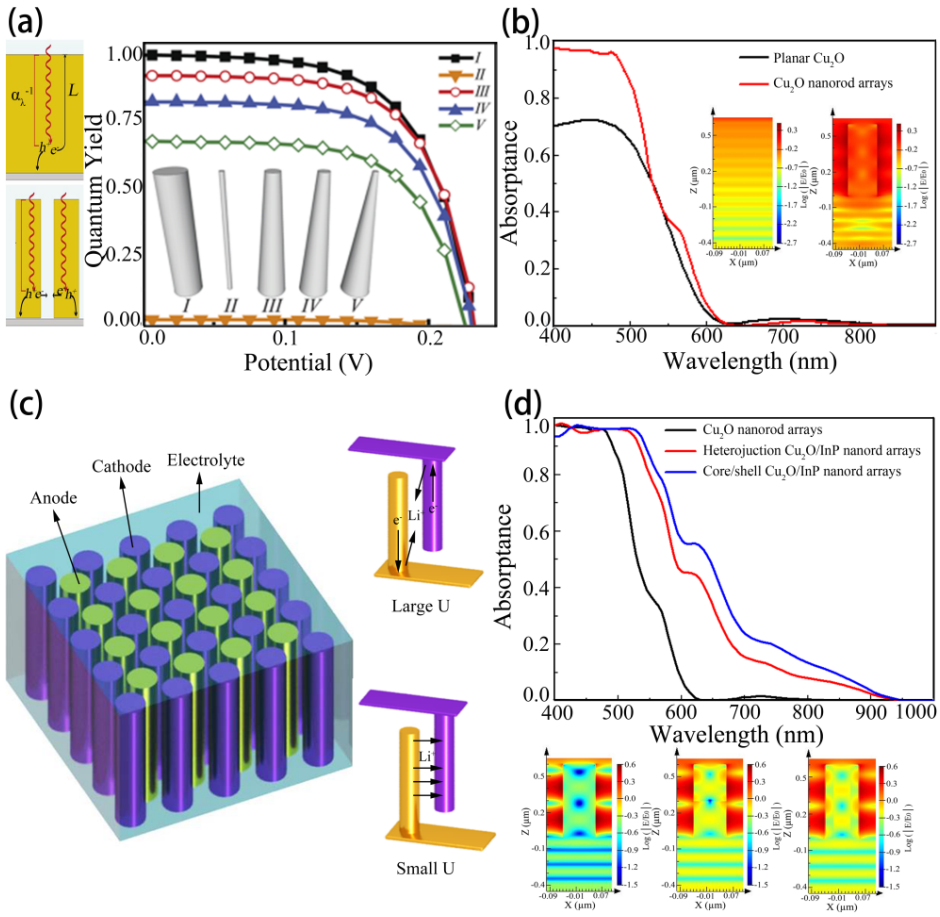

Figure 3-1. (a) Left: comparison of photogenerated charge carrier collection at planar and high aspect ratio photoelectrodes. The gray bottom represents the back contact for majority carrier collection. Right: comparison of the simulated quantum yield–potential photoresponse under AM 1.5 illumination from five different high aspect ratio morphologies.[109] (b) FDTD simulated absorptance spectrum of Cu_2O nanorod arrays with length L = 600 nm, diameter d = 100 nm on the Cu_2O substrate with thickness of 400 nm. The absorptance spectrum of a Cu_2O thin film with thickness of 1 μm is included as a reference. The inset shows the comparison of FDTD simulated spatial distribution of the electric field intensity between the planar and 1D nanostructured Cu_2O in a cross-sectional view. (c) Left: array of interdigitated cylindrical cathodes and anodes. Right: dependence of electrode utilization on electrode conductivity σ and ion diffusivity D. (d) FDTD simulated absorptance spectra (top) and spatial distribution of the electric field intensity (bottom) of Cu_2O nanorod arrays, Cu_2O/InP longitudinal heterojunction nanorod arrays and Cu_2O/InP core/shell nanorod arrays illuminated by the photons at 650 nm. (Figures are taken from[107]).

approximately from 0 to 1, when a 1D GaP nanostructure is utilized to replace the planar counterpart.

Although 1D nanostructures could reduce the diffusion length of the photo-generated charge carriers in semiconductors, it doesn't mean that a thin 1D nanostructure always results in a higher charge collection efficiency. The cross-section of a very thin 1D nanostructure might be too short to support the full internal electric field dictated by the interfacial equilibrium contact. And hence the driving force for separating the photo-generated electrons and holes is greatly crippled, which induces substantial majority carrier recombination at the contact. Only when the radius is bigger than the thickness of the depletion layer, could the internal field be large enough to separate the photo-generated charges and to conduct them to the electrodes. The quantum yield of the PEC electrodes featured by 1D nanostructure arrays has been illustrated to be largely determined by the cross-sectional profile of nanowire. As displayed in the right curve of Figure 1a, the three tapered GaP nanowires III, IV, and V show lower attainable quantum yield values than that of nanowire I due to the morphology difference and nanowire II presents the lowest quantum yield attributed to the thinnest section.[110]

With the term as "rocking chair" battery, lithium ion batteries employ the insertion processes for both the anodes and cathodes.[111] The transport of Li ions between the electrodes that are always arranged in parallel is one dimensional in nature. To minimize specific power losses originated from slow ionic transportation, the thickness of the insertion electrodes and the inter-electrode distance should be as small as possible. However, when the thickness of the electrodes is reduced, the specific energy and operating time of the device will accordingly become smaller and shorter, leading to a dilemma that limits the further performance improvement for the planar batteries. To break this morphologic limit, 1D nanostructure

proves to be a good solution. In this regard, large areal energy capacities can be realized without thickening the insertion electrodes and sacrificing the power density. The low power density and substantial Ohmic potential losses associated with the small area-to-volume ratio and long ion transport distances in the planar devices could be improved fundamentally.

The dimensionless number $U = (r^2/L^2)(\mu/\sigma)(1/C)$, where r and L is the radius and length of nanowire respectively, μ is the ionic mobility of cations, σ is the electronic conductivity of electrode materials and C is the volumetric energy capacity (C cm^{-3}), could be used to quantitatively estimate the uniformity of current across the surfaces of 1D nanostructured electrode and whether the electrode material is uniformly utilized during cell charging and discharging processes.[112] Decreasing U corresponds to a more uniform current distribution around the 1D nanostructured electrode. This scenario is a desired one, since the decrease in U usually results from high electronic conductivity in the electrodes instead of low ionic conductivity in the electrolyte. Increasing U is related to a more non-uniform discharge of the electrodes, which probably results in underutilization of the electrode materials during rapid discharge and increasing stress along the length of the electrodes.

Second, 1D nanostructures should be assembled to large areas, extending millions of nano-units to large-scale arrays for macroscopic energy applications. After the distribution of the nanostructure array is well controlled; scattering and anti-reflection effects arise and incident radiations could be easily collected, enabling it as an advantageous component in solar energy conversion devices.[113] To investigate it more convincingly, we performed finite difference time domain (FDTD) simulation for a conventional semiconductor Cu_2O. As shown in the insets of Figure 3-1b, when illuminated by photons at 500 nm, the electric field distribution around the planar Cu_2O film (thickness: 1 μm) is concentrated on the surface. As to the Cu_2O nanorod arrays, the electric field distributing scope is greatly enlarged and the

high electric field surrounds the entire nanowires arrays. As a result, Cu_2O nanorod array exhibits a dramatic improvement in absorption capability in comparison with the Cu_2O film below 480 nm, the absorbance of the 1D nanostructured specimen is nearly 1, while the value is only 0.7 for the planar sample, as displayed in Figure 3-1b.

For the energy storage applications, the available void volume between adjacent nanostructures results in a fast ion transportation, easy electrolyte accessibility to electrode and tolerance for volume expansion of the active materials. The ideal architecture for electrochemical energy storing devices is proposed as two sets of interdigitated 1D nanowire arrays in Figure 3-1c.[111] The spacing between the anodic nanowire and cathodic nanowire that accommodates a large volume change during the charging/discharging process shall be well controlled. Consequently, the deterioration problems in the planar batteries as the cycles of charging/discharging increasing could be largely alleviated by using 1D nanowire arrays. In addition, the distance for the ion transportation in discharging is dramatically reduced by adopting the interdigitated 1D nanowire and such structure is significantly less susceptible to Ohmic losses and other transport limitations. Specifically, highly ordered 1D nanostructure arrays are more performance repeatable and more compatible with the adjacent elements as compared with the irregular counterparts.

Third, according to specific requirements, the nanostructures could be constructed by multiple materials to overcome the shortcomings of the single component. For solar energy absorption, the complementary usage of the semiconductors with different band gaps in heterogeneous 1D nanostructure is of great benefit for amplifying the absorption capability of the entire device. As shown in Figure 3-1d, we have simulated the absorbing capabilities for Cu_2O/InP 1D nanowire arrays with core/shell and longitudinal heterojunction morphologies, respectively. Both heterogeneous structures present an optimized electric field distribution at

650 nm and hence an outstanding enhancement in absorbance, particularly in the region beyond the absorption limit of Cu_2O. The absorption range can be extended to near-infrared region with more than 70% of solar spectrum covered. On the other hand, the internal field at the interface of Cu_2O/InP is also profitable for separating the photo-generated charge carriers and reducing the recombination possibility. In electrochemical energy storing applications, the electrodes are usually constructed by coating the insertion electrodes on the metallic 1D nanostructure arrays. The metallic core could transport the electric energy efficiently and supply a large area for the insert electrodes.

Based on the above recognitions, three key features are crucial for realizing high-efficient energy conversion and storage devices: i) *1D nano-configuration*: its large surface area largely facilitates energy conversion/storage reactions, and the elongated longitudinal dimension provides an efficient passway for transferring charge carriers or ions. ii) The interaction and/or collecting behavior (*e.g.*, optical scattering and anti-reflection) of *large-scale arrayed* 1D nanostructures could improve the overall energy conversion and storage performance; iii) *heterogeneous* 1D nanostructure combines the advantages of different materials, resulting in *e.g.* '1+1>2' property optimization.

3.2 Progress of heterogeneous 1D nanostructure arrays based on AAO template for energy applications

3.2.1 Core/shell 1D nanostructure arrays for solar energy conversions

Despite of the antireflection effect in single componential 1D nanostructures, the core/shell 1D nanostructures can integrate the advantages of all components. For semiconductor/semiconductor core/shell nanostructures, the formation of PN junction in nanoscale supplies a large contact area for photogenerated charge separation and collection. In the case of semiconductor/metal core/shell contacts, the nanostructured metal cores or shells

could introduce the well-known surface plasmon resonance effect to the relevant devices, offering another opportunity to enhance harvesting solar energy and collecting the generated charge carriers. With regard to the semiconductor/polymer contacts, the nanostructure provides a good platform to modulate the polymer morphology and make it beneficial for charge transport and collection. Thus, these advanced core/shell 1D nanostructure arrays have been applied in most categories of photovoltaic and PEC cells.

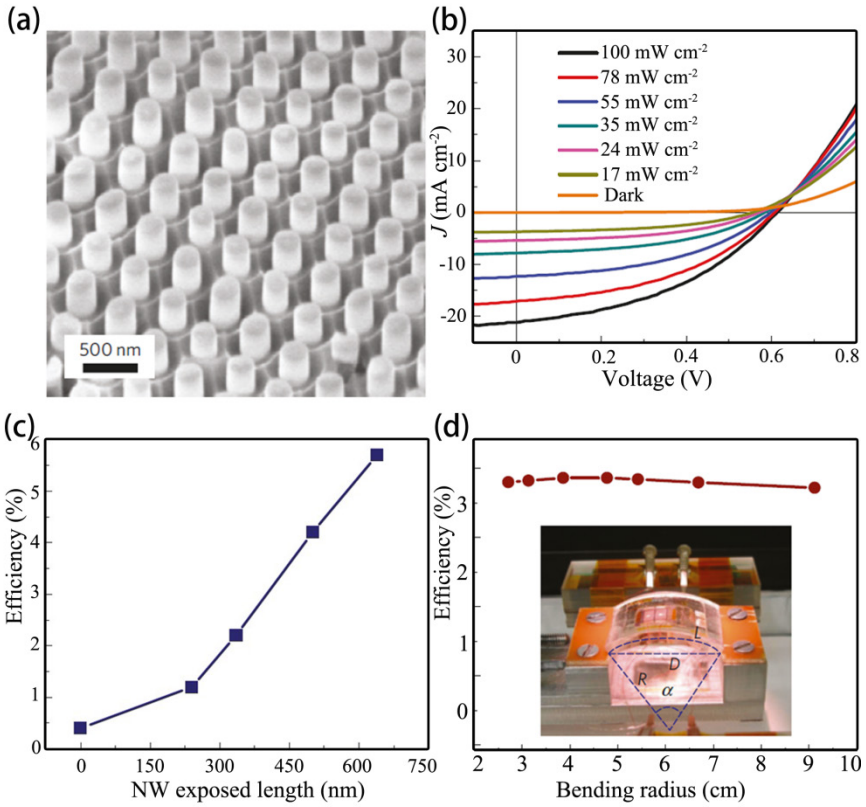

Figure 3-2. (a) SEM images of a CdS nanopillar array after partial etching of the AAO. (b) Current–voltage (J-V) characteristics at different illumination intensities. (c) Experimentally obtained efficiency of the solar cells as a function of the embedded nanopillar height. (d) Performance characterization of a flexible solar cell based on PDMS substrate. The inset shows a picture of the set-up for bending the flexible modules.[7] (Figures are taken from[7]).

As to the traditional inorganic solar cells, core/shell structure has already shown a promising merit in improving the overall efficiency. Results of selected studies are summarized in Table 1. Through simulation, Kapadia *et al*.[114] claimed that the core/shell CdS/CdTe nanopillar array solar cells could get the optimal overall efficiency over 20%, with minimal short circuit current dependence on bulk minority carrier diffusion length and thus the efficient collection of photo-generated carriers. Fan *et al*.[7] proposed such solar cells based on CdS/CdTe nanopillar arrays experimentally. The core CdS was prepared by chemical vapor deposition (CVD) procedure (Figure 3-2a). And after partly removing the AAO, another CVD process was conducted for growing the CdTe shell. By manipulating the morphological parameters, the solar energy conversion efficiency was obtained as 6%, displayed in Figure 3-2b and c. To be noteworthy, the authors also transferred the device to a flexible substrate. Though the efficiency was lowered to 4%, the flexible device can sustain large bending without degradation in structure and performance (Figure 3-2d). Liu *et al*.[115] combined an electrochemical deposition route with thermal evaporation to grow CdS/CdTe core/shell structure for photovoltaic applications and the best performance of the relevant devices was close to 6.5%. Afterwards, the same group developed a modified strategy, in which the prepared CdS nanowire and the CdS/CdSe PN junction were further treated by multi-step $CdCl_2$ soaking and annealing procedures.[116] With graphite paste as the electrode, the device presented a power conversion efficiency value of 9.8%, which was the highest value of the nanowire-based solar cells. The above structures are based on the deposition of active materials into AAO template to form 1D nanostructures like nanorods and nanotubes, however, through the manipulation on the anodizing and pore opening, the inverted nanocone structure could also be interesting. Using such novel architecture, Lin *et al*.[117] fabricated multiple core/shell structure AAO/Ag/AZO/ a-Si:H/ITO for solar energy conversion. Due to

the purposely prepared antireflection structure, the absorption efficiency was improved and thus high energy conversion efficiency was attained as 7.6%.

Regarding the semiconductor/polymer hybrid solar cells, semiconductor 1D nanostructure arrays are usually embedded in the polymer films. As the renowned electron acceptor, TiO_2 nanorod arrays were fabricated by AAO template with sol-gel technique and P3HT was prepared by spin-coating to form the hybrid cell.[118] The resultant energy conversion efficiency of the relevant device was around 0.51%, almost five folds larger than the device using planar TiO_2. Alternatively, TiO_2 nanotube arrays were also synthesized by the technique integrating AAO template and ALD[119] (or liquid ALD[120]) to construct photovoltaic devices with P3HT. Similar results were gained, indicative of the superiority of the 1D core/shell nanostructures. Attributing to the large band gap of TiO_2 (3.2 eV) that could inhibit the absorption in visible range, CdTe nanorod arrays synthesized by electrochemical deposition procedures with AAO template, were adopted to obtain core/shell structure with P3OT and the energy conversion efficiency was obtained as 1.06%.[121] An improvement for this structure was achieved by building CdSe/P3HT core/shell nanorod arrays and the efficiency of 1.38% was realized by increasing the length of the CdSe nanorods to 612 nm.[122] Replacing the P3HT with PEDOT:PSS to form Schottky junction instead of PN junction with CdSe, a further enhancement in efficiency was claimed as 3.22%.[123]

Besides, AAO template can also be used as the scaffold to regulate the growth of polymer nanorods. Kim *et al.*[124] placed an AAO template on a P3HT coated ITO substrate. By annealing at 250 ^{o}C under vacuum, the molten P3HT chains readily entered the nanopores by capillary action. Well-ordered polymer nanorod arrays were achieved after removing the template (Figure 3-3a). The chain alignment in the P3HT nanorods could facilitate the charge

transfer in each nanorod (Figure 3-3b and c). Compared with planar devices, the resultant P3HT nanorods/C60 polymer solar cells showed a great improvement in energy conversion

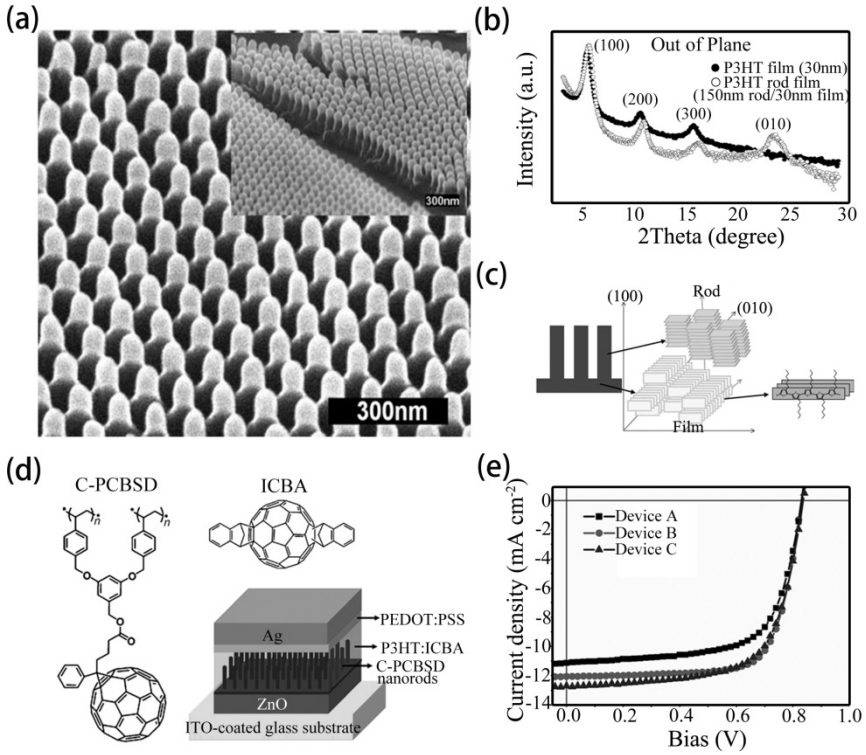

Figure 3-3. (a) SEM images of P3HT nanorods prepared using the AAO template, after removal of the Al/Al_2O_3 layer. (b) Out-of-plane grazing incidence angle X-ray diffraction intensities as a function of scattering angle 2θ for planar P3HT films. (c) Schematic representation of P3HT chain conformation in nanorods and thin film.[124] (d) Chemical structure of C-PCBSD and ICBA. Schematic representation of the nanostructured device architecture. (e) J–V characteristics of the as-fabricated C-PCBSD/P3HT/ICBA devices: A: P3HT/ICBA without C-PCBSD nanorods; B: P3HT/ICBA with 170 nm C-PCBSD nanorods; C: P3HT/ICBA with 360 nm C-PCBSD nanorods.[125] (Figures are taken from[124], [125]).

efficiency to 1.12%. Actually, C60 is not a good candidate as the electron acceptor in polymer solar cells. Chen *et al*.[126] made a further improvement by using spin-coated PCBM to replace

the C60 and the overall efficiency was enhanced to 2.4%. Instead of spin-coating PCBM into the P3HT nanorods, in other work, PCBM was mixed with P3HT in the solution and then spin-coated on the ITO substrate.[127] After placing AAO on the top, the sample was annealed at a temperature higher than the melting points of both materials under vacuum conditions. Owing to the different diffusion rate in the AAO pores, P3HT/PCBM core/shell structure formed naturally in the annealing procedure.[128] The optimal conversion efficiency was around 3.6% for the devices with nanorods of about 200 nm in length. This unique procedure for realizing core/shell polymer heterojunction structure was proven to be advantageous over the procedure of spin-coating PCBM into P3HT nanorods arrays. In that case, the morphology of the architecture was not optimized for exciton separation and charge conduction. A further progress was made by constructing cross-linkable fullerene material [6, 6]-phenyl-C61-butyric styryl dendron ester (PCBSD) nanorod arrays to collaborate with P3HT:IBCA (indene–C60 bisadduct), as shown in Figure 3-3d.[125] This novel structure integrates the advantages of both bulk heterojunction and core/shell 1D nanostructure, enabling the relevant devices with unprecedented overall efficiency of 7.3% in area of polymer solar cells (Figure 3-3e).

The huge surface area and efficient charge conducting in 1D nanostructure arrays also provide a good platform for PEC reactions. According to the roles in the PEC reactions, different core/shell 1D nanostructures have been fabricated particularly as the PEC electrodes. Based on AAO template, Martinson *et al*.[129] prepared AAO/ITO/TiO_2 core/shell structure as the photoanode, where AAO behaved as the scaffold, ITO nanoshell arrays were used as the electron collector and TiO_2 was the active material for PEC reactions. In this design, electrons can diffuse radially through the wall of semiconducting tubes and be efficiently collected by the adjacent and concentric ITO tube. The yielded conversion

Table 1. The development of heterogeneous solar cell based on AAO template

Material	Configuration	Synthetic approach	Efficiency	Material	Configuration	Synthetic approach	Efficiency
CdS/CdTe[7]	CS[a] PN junction	CVD[b] and TE[c]	6%	P3HT /C60[124]	CS Schottky junction	Annealing and spin-coating	1.12%
CdS/CdTe[116]	CS PN junction	ED[d] and TE	9.8%	P3HT /PCBM[126]	CS polymer junction	Annealing and spin-coating	2.4%
AZO/a-Si:H/ITO[117]	CS PN junction	Sputtering and CVD	7.6%	P3HT /PCBM[128]	CS polymer junction	Mixture and Annealing	3.6%
TiO_2/P3HT[118]	CS hybrid PN junction	Sol-gel and spin-coating	0.51%	PCBSD/ P3HT:IBCA[125]	CS polymer junction	Spin-coating and Annealing	7.3%
CdTe/ P3OT[121]	CS hybrid PN junction	ED and spin-coating	1.06%	ITO/TiO_2[129]	CS photoanode of DSSC	ALD[e]	1.1%
CdSe/P3HT[122]	CS hybrid PN junction	ED and spin-coating	1.38%	Au/TiO_2[130]	CS photoanode of DSSC	ED and sol-gel	5.4%
CdSe/PEDOT:PSS[123]	CS hybrid PN junction	ED and spin-coating	3.22%				

a) core/shell; [b]chemical vapor deposition; [c]thermal evaporation; [d]electrochemical deposition; [e]atomic layer deposition.

efficiency was dramatically enhanced to 1.1%, much higher than that of the planar devices. Similar structures were acquired by using Au nanowires as electron collector to replace the ITO in the above design.[130] The conversion efficiency was gauged as 5.4% by soaking the relevant Au/TiO_2 core/shell photoanode in $TiCl_4$ solution. Maijenburg *et al.*[131] adopted the sol-gel and electrodeposition methods for synthesizing Ag/TiO_2 isolated core/shell autonomous nanowires and applied it as the photoanode for water splitting. It was demonstrated that the as prepared device showed a higher efficiency than bare TiO_2 nanotubes and TiO_2 nanotubes with attached Ag, respectively. A high H_2 generation range as 1.23×10^{-3} mol g^{-1} h^{-1} was achieved. In consideration of the large band gap of conventional photoanode materials like ZnO and TiO_2, other materials with the absorption capability in the visible region have to be employed. Lee *et al.*[132] designed a plasmonic water splitting cell. The cell was functioned by illuminating a dense array of aligned gold nanorods capped with TiO_2, forming a Schottky metal/semiconductor interface which collected and conducted the hot electrons to an unilluminated platinum counter-electrode where hydrogen gas evolved. The result demonstrated that 95% of the effective charge carriers derived from surface plasmon

decay to hot electrons (Figure 3-4a to c). Furthermore, by removing the squarely ordered AAO template to leave an Al nanospike array behind, Qiu *et al.*[133] fabricated Al/Ti/Pt/FTO/α-Fe_2O_3 core/shell array on this peculiar architecture (Figure 3-4d). The absorption efficiency of the corresponding photoanode approached to 100% at 700 nm. After ED of CoPI onto the nanostructures, the photocurrent was measured as high as 4.36 mA cm^{-2} at 1.60 V vs RHE, about three times of that for a planar photoelectrode (Figure 3-4e to f). Meanwhile, the short hole diffusion length in α-Fe_2O_3 cannot limit the active layer thickness by this design.

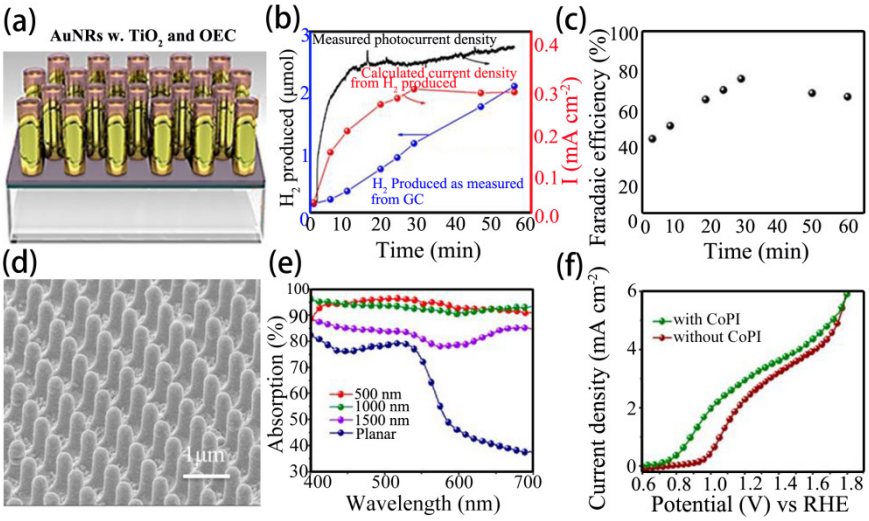

Figure 3-4. (a) Schematic of core/shell 1D nanostructures of Au/TiO_2/OEC. (b) The quantity of evolved hydrogen as a function of time, the photocurrent simultaneously recorded at 1 V vs RHE with visible light illumination and the photocurrent calculated from the evolved H_2. (c) Faradaic efficiency of the process.[132] (d) SEM image of the Ti/Pt/FTO/Fe_2O_3 nanospike array. (e) UV−vis optical absorption spectra of device on nanospike substrate with different pitches. (f) Comparison of the J−V curves between electrodes with and without CoPI.[133] (Figures are taken from[132], [133])

As to photocathode in water splitting, core/shell 1D nanostructure arrays still exhibit impressive merits. Huang *et al.*[134] fabricated photocathode with complex Cu_2O/CuO/TiO_2

core/shell structure based on AAO technique. In this case, the suffer of Cu_2O from significant photo-induced reductive decomposition with the electronic state of copper transferred from Cu(I) to Cu(0) could be well alleviated by modifying the surface of the Cu_2O nanowires with protecting layers of CuO and TiO_2. The photocathodes with $Cu_2O/CuO/TiO_2$ were found to gain a 74% higher photocurrent and 4.5 times higher stability, compared to that with bare Cu_2O nanowires array.

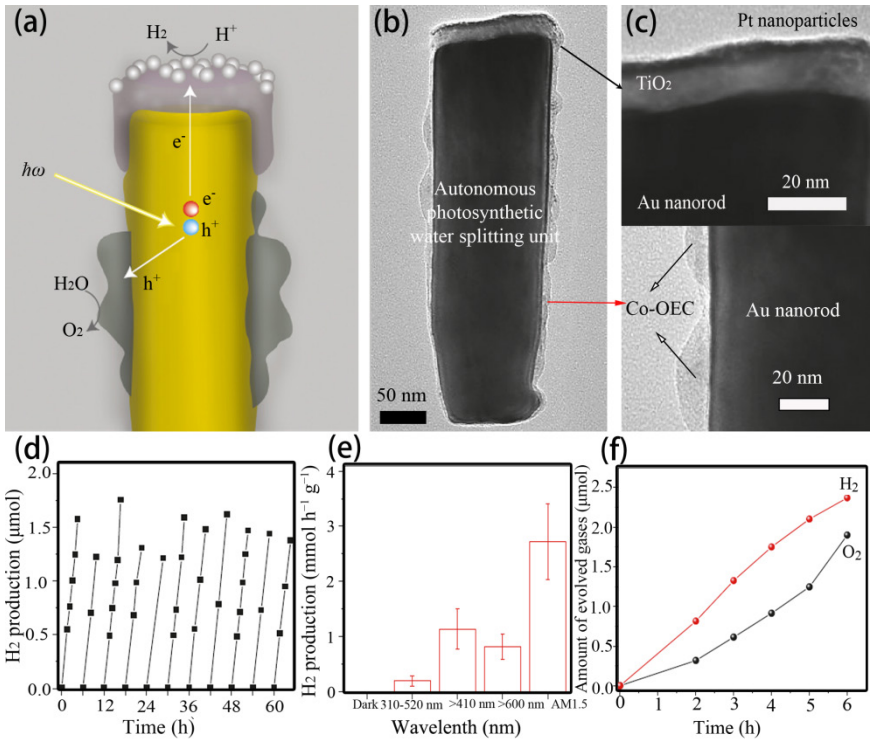

Figure 3-5. (a) Schematic of a cross-section of an individual photosynthetic unit. (b) The corresponding transmission electron micrograph. (c) Magnified TEM views of the platinum/TiO_2 cap (top right) and the Co-OEC (bottom right). (d) Hydrogen evolution under visible-light illumination (λ>410 nm) as a function of time. (e) Hydrogen produced per hour with various illumination wavelengths. (f) Measured O_2 and H_2 photoproducts as a function of time.[8] (Figures are taken from[8])

Extending the concept from ref 94, the architecture of core/shell nanostructure arrays has another alternative design; a core and a shell with discontinuously distributed multiple

components. Each shell component is in charge of an individual function as that the core/shell nanostructure is of great potential to accomplish an integrated application. As portrayed in Figure 3-5a to c, the Au nanorods prepared by AAO template have a purposely deposited shell consisting of a thin layer of Pt decorated TiO_2 on the top and Co-OEC on the sides.[8] In this regard, the hot electrons in the stimulated Au nanorods could inject to the conduction band of TiO_2. The Pt nanoparticles on the surface of TiO_2 facilitate the injected electrons transferring to the interface with the electrolyte to drive the water reduction reactions therein for H_2 generation, producing 5×10^{13} H_2 molecules per cm^2 per second under 1 sun illumination, with long-term operational stability (Figure 3-5d to f). On the other hand, the remained holes in the Au nanorods transfer to the contact zone of Au/Co-OEC. The Co-OEC acts as the oxidation catalyst and initiates water oxidation reaction for O_2 generation utilizing the holes therein. Accordingly, such unique core/shell nanorod is integrated with both a photocathode and a photoanode. Getting rid of external wires, this architecture is of great significance for improving the energy conversion efficiency and reducing fabrication cost, since the relevant nanorod arrays can be dispersed in the electrolyte and generates H_2 and O_2 synchronously without any circuit connection and external bias.

3.2.2 Longitudinal heterojunction 1D nanostructure arrays for solar energy conversions

Rather than core/shell nanostructures that extend components cross-sectionally, longitudinal heterojunction 1D nanostructure contains multiple segments in the longitudinal direction, meaning that each 1D nanostructured unit could be served as an individual photovoltaic device. Such device is of high advantage as the power supply for microelectronic circuits that do not need a large driving current. To be exciting, the elongated straight pores in AAO template provide an irreplaceable mold for growing the multiple segmental nanostructure

arrays. For the inorganic/organic heterostructures, CdS/PPy nanowires show a strong photo-dependent rectifying effect and the conducting property of the organic/inorganic P-N junction nanowire can be tuned by changing the intensities of incident light.[135] Meanwhile, the structure still possesses an obvious photovoltaic performance, a power conversion efficiency of 0.018% under an illumination intensity of 6.05 mW cm^{-2} was detected.[136] Yoo *et al*.[137] employed Au/CdSe/PPy structure as a segment buried in the porous Au nanowires. The complicated structure gained a 1.1% power conversion efficiency, almost 100 folds larger than that of the CdS/PPy devices. An even higher energy conversion efficiency of 1.62% was acquired using P3HT:PCBM bulk heterojunction structure to form in the nanowire.[138] In addition, nanowires with even more segments like Ni/Au/PEDOT/CdSe:P3HT/Au could be realized by AAO template,[139] current-voltage characterization of a single nanowire exhibited p-n diode behavior with a significant photoconductive effect under illumination. Such single nanowire device maintained a remarkable 280 fold on/off ratio under 70 mW cm^{-2} excitation at 3.75 V potential, which at that time was comparable to that for the best P3HT/CdSe thin film photodetector.

Macroscopically, the longitudinal heterojunction 1D nanostructure arrays could be utilized as significant components in large scaled energy conversion devices. Mubeen *et al*.[140] reported a scalable design and molecular level fabrication strategy to create PEDOT/CdSe/Ni/Au/Pt heterostructure nanowire, as displayed in Figure 3-6a and b. Without removing AAO template, each nanowire was isolated from its neighbor by the transparent electrically insulating oxide cellular enclosure and the architecture could be used as free floating devices for water splitting. When illuminated by light, the devices were demonstrated to produce hydrogen at a stable rate for over 24 h in corrosive hydroiodic acid electrolyte without

applying any external bias (Figure 3-6c). The yielded quantum efficiency for absorbed photons-to-hydrogen conversion was 7.4% and solar-to-hydrogen energy efficiency of

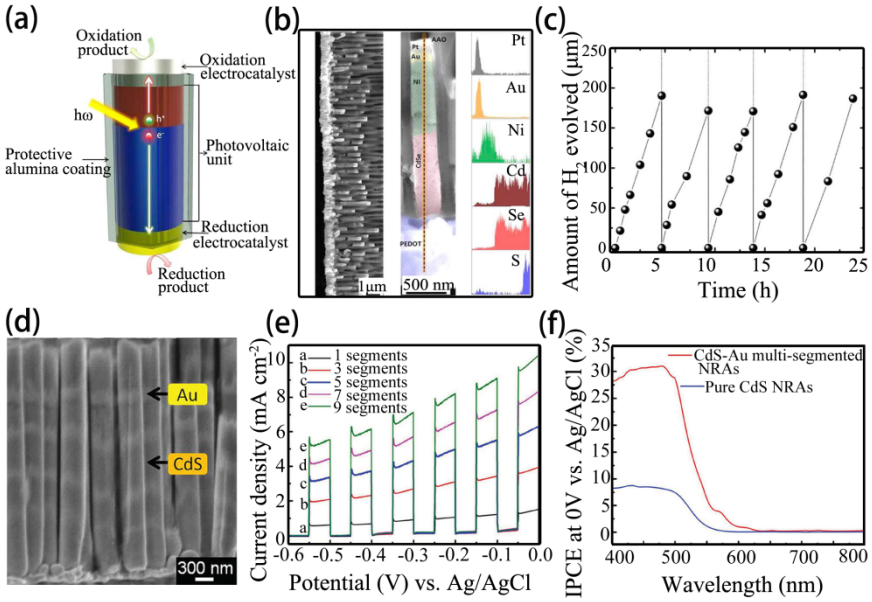

Figure 3-6. (a) Schematic of an individual nanowire unit with semiconductor absorber layer protected inside a nonabsorbing insulating AAO pore. (b) Cross-sectional SEM image and High-magnification SEM image of the multiple component nanowires.[140] (c) Artificial photosynthetic performance of the structures. (d) SEM images of the multi-segmented CdS-Au nanorod arrays. (e) Linear sweep voltammogram curves of the multi-segmented CdS-Au nanorod arrays with different number of segments under simulated AM 1.5G illumination. (f) Measured IPCE (external quanum yield) spectra of the multi-segmented CdS-Au and pure CdS nanorod arrays collected at the incident wavelength range from 400 to 800 nm at a potential of 0 V vs Ag/AgCl.[141] (Figures are taken from[140], [141])

incident light was 0.9%. Figure 3-6d shows another impressive example proposed by Wang *et al.*,[141] in which multi-segmented CdS-Au nanowire array with a sequential and highly tunable configuration was particularly employed as photoanodes. When the multi-segmented CdS-Au nanowires were implemented as a photoanode in the PEC cell and a positive bias

was applied, a series of forward-bias and reverse-bias Schottky barriers was generated at the Au/CdS and CdS/Au interfaces, respectively. In combination with the surface plasmon effect of each Au nano-unit that could greatly enhance the absorption efficiency of the photoanode, the photocurrent at 0 V vs Ag/AgCl was as high as 10.5 mA cm^{-2}.

3.2.3 Core/shell 1D nanostructure arrays for supercapacitors

Electrochemical supercapacitors (ES) owing to their high power density and long cycle life play important roles in various energy storage devices and have been applied particularly in hybrid vehicles and backup power supplies. Considering the constraints from low energy densities in the current supercapacitors, it is extremely crucial to develop supercapacitors with high energy densities.[142] Generally, there are two types of ES in developing. One is the electrical double-layer supercapacitors (EDLS), in which the electrode material like carbon is electrochemically inert. In this scenario, there are no electrochemical reactions happening on the electrode material during the charging and discharging processes and pure physical charge accumulation occurs at the electrode/electrolyte interface. The other type is the faradaic supercapacitors (FS), in which the electrode materials (*e.g.,* metal oxides and electronically conducting polymers) are electrochemically active.[143-146] These electrode materials can directly store and release charges during the charging and discharging processes. For both types, configuring the electrodes into 1D nanostructure arrays are currently considered as one of the most promising plans. In this section, thus, we mainly concentrate on the recent progresses in core/shell 1D nanostructure arrays based on AAO template for supercapacitor applications.

A series of core/shell nanostructure arrays, like Ni/V_2O_5,[147] MnO_2/PEDOT,[148-150] RuO_2/PEDOT,[151] Pt/RuO_2,[152] Au-MnO_2/CNT,[153] MnO_2/TiN,[154]; and Ni/NiO[155] were realized. Typically, MnO_2/PEDOT core/shell nanowire arrays were synthesized by a one-step

electrochemical deposition process using AAO template, as portrayed in Figure 3-7a.[148] The composition of the nanowires was able to be adjusted by the different deposition potentials

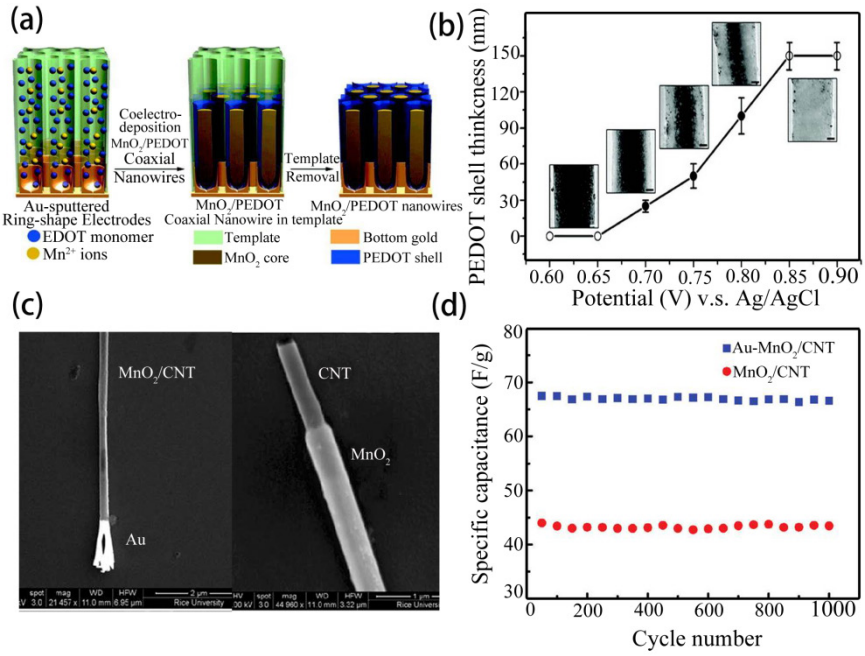

Figure 3-7. (a) One-step synthesis of MnO_2/PEDOT core/shell nanowires. (b) PEDOT shell thickness variation with applied potential from 0.6 to 0.9 V.[148] (c) SEM images of Au segmented CNT/MnO_2 (left) and CNT/MnO_2 core/shell structures (right). (d) Specific capacitance versus cycle number plots of supercapacitors with symmetric assembly of CNT/MnO_2 and Au-CNT/MnO_2 electrodes.[153] (Figures are taken from[148], [153])

(Figure 3-7b). In this architecture, the MnO_2 core was utilized for achieving a high energy density and the PEDOT shell was employed attributing to its highly conductive, porous and flexible nature. As a consequence, the corresponding devices yielded high specific capacitances (180 F g^{-1}) at high current densities (25 mA cm^{-2}), much higher than the devices containing pure MnO_2 nanowires, PEDOT nanowires, and MnO_2 thin films, respectively. Afterwards, by carefully tuning the electrochemical deposition potential, it was found that the MnO_2/PEDOT core/shell nanowires were preferred to be gained between 0.6 and 0.9 V. An

optimal specific capacitance of 270 F g^{-1} was measured under an ideal potential of 0.7 V.[150] In other efforts, the same authors loaded finely dispersed MnO_2 nanoparticles into PEDOT nanowires by simply soaking PEDOT nanowires into a potassium permanganate solution, which yielded an enhancement of up to 4 times in the energy storage capacity and caused only a minimal volume expansion in the polymer.[150] Alternatively, RuO_2/PEDOT core/shell nanotube arrays were also approved as a good example. Such nanotubular composites were synthesized by a step-wise method.[151] The PEDOT nanotubes were grown in AAO template by electropolymerization and then RuO_2 was deposited into this porous PEDOT nanotube matrix electrochemically. The relevant electrode presented a specific capacitance up to 640 F g^{-1} even at a high power demand of 20 kW kg^{-1}. In other attempts, the multi-segmented Au-MnO_2/CNT core/shell arrays were fabricated in AAO templates using a method integrating electrochemical deposition, infiltration, and CVD.[153] In this structure, CNTs served as an additive for improving the electrical conductivity of the manganese oxide electrodes and can also be a host for charge storage due to the active electrode characteristics. The well-adhered interface between Au and MnO_2/CNT core/shell segments led to nanoscale electrical contacts between the electrode and current collectors, favorable for reducing the Ohmic loss (Figure 3-7c). Noteworthily, integrating CNTs and metal oxide nanowires, the electrode possessed a dual storage mechanism of EDLC and FS and exhibited a maximum specific capacitance of 68 F g^{-1}, a power density of 33 kW kg^{-1}, and an energy density of 4.5 W h kg^{-1} (Figure 3-7d). Though many efforts were placed on increasing the length of the 1D nanostructures to load more active materials, practically, the length cannot be prolonged unlimitedly. As the length of 1D nanostructures increases, the agglomeration of the 1D nanostructures becomes more serious and this will jeopardize the performance and stability of electrodes. On the other hand, the AAO template can sustain the depth of the pore to a large scale. Thus, it is wise to

duplicate such structure from insulative AAO temple to other functional materials. Recently, our group copied the insulative AAO template to a Ni template precisely through two

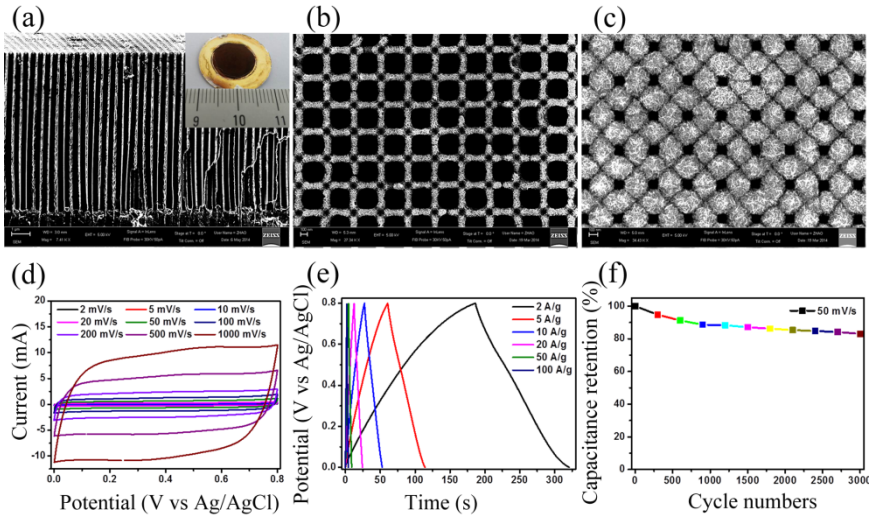

Figure 3-8. (a) Cross-sectional SEM image of a bare Ni nanopore array and the inset is photography of the relevant Ni nanopores. (b) and (c) The Ni nanopore arrays after loaded with 80 μg cm^{-2} and 400 μg cm^{-2} MnO_2, repectively. (d) CV curves of the sample in b at different scan rates. (e) Galvanostatic charge-discharge profiles of the sample in b. (f) Cycling stability of the sample in b as a function of cycle number with a scan rate of 50 mV s^{-1}.[156] (Figures are taken from[156])

replication processes.[156] In the first step, ordered array of PMMA nanopillars was obtained after removing the AAO template that acted as the initial template. Then the PMMA nanopillar array was adopted as the template for the electrochemical deposition of Ni nanopore array with a gold film as the working electrode in the second step (Figure 3-8a). The resultant was used to form a Ni/MnO_2 core/shell electrode for supercapacitor (Figure 3-8b and c). Accordingly, the electrode presented a symmetrically rectangular shape of CV curves without any significant distortion, even when a scan rate of 1000 mV s^{-1} was applied (Figure 3-8b). The specific capacitance was measured as 672 F g^{-1} at 2 mV s^{-1} with a MnO_2 mass loading of 80 μg cm^{-2} and it could still reach up to 382 F g^{-1} at 2 mV s^{-1} when the

loading was increased to 400 μg cm^{-2} (Figure 3-8d to f). Moreover, such metallic nanopore array with tunable structural parameters can be further exploited as an alternative 1D nanostructure array for various other applications, such as electrodes for batteries, water-splitting devices and so on.

Apart from electrochemical supercapacitors, AAO template is also of great potential for fabricating conventional metal/insulator/metal (MIM) electrostatic capacitors. One of the characteristic features for electrostatic capacitors is high power density, which is largely limited by surface charge. To achieve a dense packing of active interfaces in a large surface area, 1D nanostructure arrays that offer a huge internal surface turn out to be a good choice. Using CVD, composite MIM nanotubes with alternating conductive (carbon) and insulating (boron nitride) layers were created within 200 nm AAO templates by Shelimov *et al*.[157] For the 50 μm thick templates, specific capacitances as high as 2.5 μF cm^{-2} were attained. Additionally, Al/Al_2O_3 barrier layer/CNTs MIM capacitors were fabricated by growing CNTs through thermal CVD process in AAO template with 30 nm pore size. The results yielded a specific capacitance of 174 nF cm^{-2} at 100 kHz.[158] A further significant improvement in specific capacitance was achieved by Banerjee *et al.*,[10] who fabricated TiN/Al_2O_3/TiN MIM structures through three-step continuous ALD process by the assistance of AAO template with 100 nm pore size. These highly regular arrays possessed a specific capacitance of 10 μF cm^{-2} for 1 μm thick AAO template and 100 μF cm^{-2} for 10 μm thick AAO template, significantly exceeding previously reported values for MIM capacitors in porous templates. Afterwards, the same group carried out a careful chemical pore widening treatment on AAO template, which resulted in a sharp and smooth AAO nanotopography.[159] The according breakdown field for the MIM layer was then increased from about 4 MV cm^{-1} to about 10 MV cm^{-1}. The expected energy densities were 1.5 Wh kg^{-1}, the highest ever

reported for electrostatic MIM nanocapacitors and 2 times larger than that of their previous work.

4 Experiments and instrumentations

All experiments and methods throughout this dissertation are performed and carried out according to the procedures described in this section. The nanostructures and devices are prepared from a combination of *synthesis techniques* and *imprinted AAO templates*. The morphology, geometry and composition of the nanostructures are confirmed by *Field emission scanning electron microscopy (SEM)*, *Transmission electron microscopy (TEM), Energy-dispersive X-ray spectroscopy (EDX).* The device characterization and measurement are conducted with *electrochemical workstation, solar simulator, transient absorption spectroscopy, room-temperature UV-Vis absorption spectroscopy, and incident photon to charge carrier efficiency (IPCE) tester*. The simulations are carried out with *COMSOL Multiphysics* and *Finite Difference Time Domain (FDTD).*

4.1 Synthesis techniques

4.1.1 Atomic layer deposition

Atomic layer deposition (ALD) has drawn much attention as a versatile methodology for thin film deposition due to conformal and uniform deposition of thin films on substrates with complicated 3D morphology.[160, 161] In ALD, a thin film of desired material is grown in a layer-by-layer manner by repeating a reaction cycle composed of four consecutive steps: (i) reactant A exposure, (ii) purge (or evacuation) of unreacted excess gas molecules and reaction byproducts, (iii) reactant B exposure, and (iv) subsequent purge. So far, a wide range of materials has been grown by ALD.[162] The materials encompass metals (Pt, Ru, Pd, Ir, et al.), insulators (Al_2O_3, HfO_2, et al.) and semiconductors (ZnO, TiO_2, TiN, CuS, et al.) in both crystalline and amorphous phases. In this dissertation, six kinds of materials, including TiO_2, ZnO, Al_2O_3, SnO_2, and Pt, are prepared for the different purpose. All of the ALD reactions in this dissertation are carried out in Picosun SUNALETM R150 ALD System.

4.1.1.1 Atomic layer deposition of TiO_2

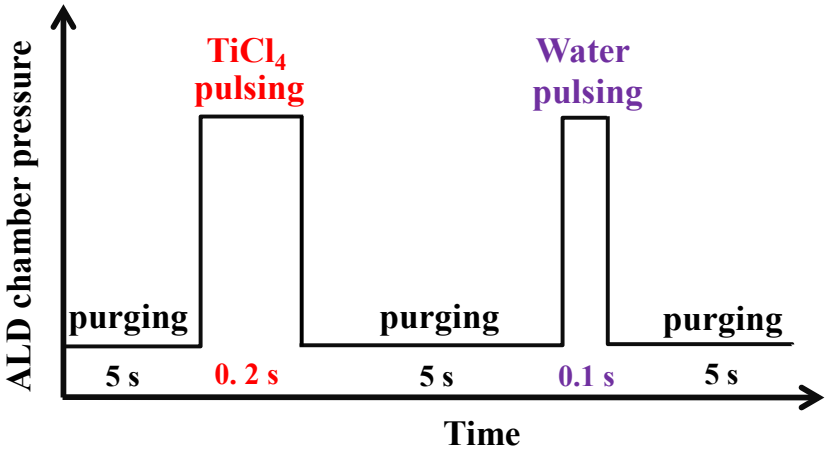

Figure 4-1. One cycle of TiO_2 growth, including the N_2 purging, $TiCl_4$ pulsing, and H_2O pulsing times.

Titanium (IV) chloride ($TiCl_4$, Sigma-Aldrich) and distilled-water (H_2O) are used as the precursors of Ti and O, respectively. The reactor is maintained at a temperature of 300 °C and the N_2 carrying gas is kept at 100 sccm during the deposition process. The detailed recipe for TiO_2 growth is revealed in Figure 4-1. The growth rate of TiO_2 is about 0.6 nm per cycle and the cycle numbers are defined by the purpose.

4.1.1.2 Atomic layer deposition of Al_2O_3, ZnO and Al doped ZnO

Trimethylaluminum (TMAl, Sigma-Aldrich), Diethylzinc [DEZn, $Zn(C_2H_5)_2$], and distilled-water (H_2O) are used as the precursors of Al, Zn and O, respectively. The reactor is maintained at a temperature of 200 °C and the N_2 carrying gas is kept at 100 sccm during the deposition process. The recipe of Al_2O_3, ZnO and AZO growth is as similar as that described in TiO_2. The growth rate of Al_2O_3 and ZnO is about 1.0 nm per cycle. The pulsing time of TMAl, DEZn, and H_2O is 0.1 s, and the purging time is 5 s. One typical Al_2O_3 growth cycle consists of: TMAl – N_2 purge – H_2O – N_2 purge. One typical AZO growth cycle consists of: DEZn – N_2 purge – H_2O – N_2 purge (20 cycle ZnO)-TMAl-N_2 purge-H_2O-N_2 purge.

4.1.1.3 Atomic layer deposition of SnO_2

Tin (IV) chloride ($SnCl_4$, Sigma-Aldrich) and distilled-water (H_2O) are used as the precursors of Sn and O, respectively. The reactor is maintained at a temperature of 250 °C and the N_2 carrying gas is kept at 100 sccm during the deposition process. The recipe of SnO_2 growth is as similar as that described in TiO_2. The growth rate of SnO_2 is about 0.3 nm per cycle. The pulsing time of $SnCl_4$ and H_2O are 0.5 s and 0.1 s, respectively. The N_2 purging time is 5 s.

4.1.1.4 Atomic layer deposition of Pt

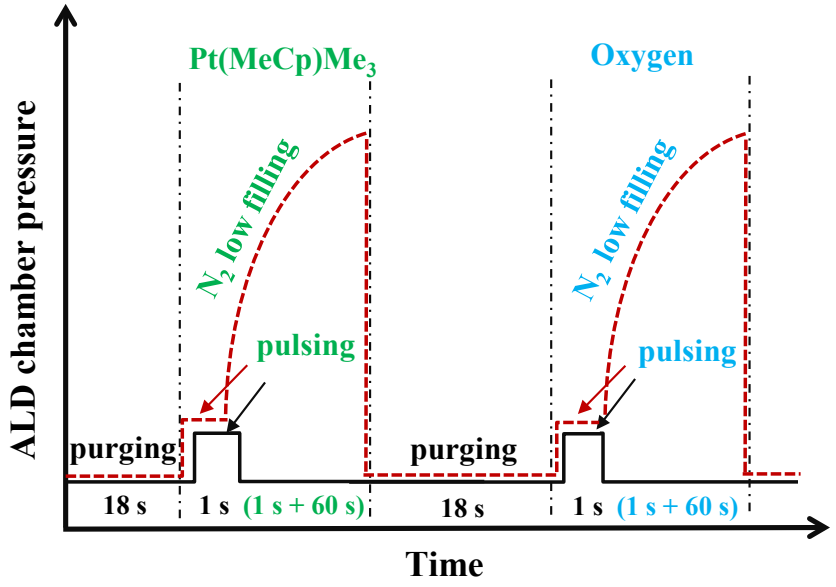

Figure 4-2. Conventional (solid line) and innovative (dot line) recipes of Pt growth (1 cycle).

Trimethyl(methylcyclopentadienyl)platinum(IV)($Pt(MeCp)Me_3$, 98%, Sigma-Aldrich) and Oxygen gas (O_2) are used as the precursor of Pt. The reactor is maintained at a temperature of 300 °C and chamber pressure varies from 8 hPa to 30 hPa under different deposition steps. The temperature of $Pt(MeCp)Me_3$ canister was held at 80 °C. The N_2 carrying gas is kept at 100 sccm, during the deposition process, the pressure values for $Pt(MeCp)Me_3$ line and O_2 line are ~ 10 hPa. The innovative recipe for Pt growth is revealed in Figure 4-2. First, the N_2 carrying gas is kept at 100 sccm. Next, during the low N_2 filling period, the N_2 carrying gas is decrease to 60 sccm, the pressures for $Pt(MeCp)Me_3$ line and O_2 line in low N_2 filling period

are ~ 28 hPa. One typical innovative ALD growth cycle consists of $Pt(MeCp)Me_3$ pulsing (1.0 s) – low N_2 filling (60 s) – N_2 purging (18 s) – O_2 pulsing (1.0 s) – low N_2 filling (60 s) – N_2 purging (18 s).[163]

4.1.2 Electrochemical deposition

Electrochemical deposition is generally used for the growth of metals, conducting metal oxides, and conducting polymers because of the following advantages: (i) the thickness and morphology of the nanostructure can be precisely controlled by adjusting the electrochemical parameters, (ii) relative uniform and compact deposits can be synthesized in template-based structures, (iii) higher deposition rates are obtained, and (iv) the equipment is inexpensive due to the non-requirements of either a high vacuum or a high reaction temperature.[164] A simple modification in the electroplating process is the pulse electroplating. This process involves the swift alternating of the potential or current between two different values resulting in a series of pulses of equal amplitude, duration and polarity, separated by zero current. By changing the pulse amplitude and width, it is possible to change the composition and thickness of the deposited film. All the electrochemical depositions in this dissertation are conducted using electrochemical workstation (BioLogic, Inc.).

4.1.2.1 Deposition of Ni film and Ni nanowire

Nikel (Ni) film deposition is carried out in a Ni plating solution comprising 8.41×10^{-2} M Nickel(II) chloride ($NiCl_2$, Sigma-Aldrich), 1.59 M Nickel sulfamate (II) tetrahydrate ($(H_2NSO_3)_2.4H_2O$, Sigma-Aldrich), and 0.33 M Boric Acid (H_3BO_3, Sigma-Aldrich). The typical current density for the Ni electrodeposition is 10 mA cm^{-2}. Ni nanowires are deposited with a current density of 1.0 mA cm^{-2} in the same Ni plating solution.

4.1.2.2 Deposition of Ag nanowire

Silver (Ag) nanowire deposition is conducted in an Ag plating solution (alfa aesar) with a cathodic current density of 1.0 mA cm^{-2}.

4.1.2.3 Deposition of CdS nanowire

Cadmium sulfide (CdS) nanowires are deposited under a constant anodic current (1.5 mA cm^{-2}) in DMSO solution consisted of 0.055 M Cadmium Chloride ($CdCl_2$, Sigma-Aldrich) and 0.19 M element sulfur (S, Sigma-Aldrich) at 120 °C.

4.1.2.4 Deposition of Cu_2O nanowire

Cuprous oxide (Cu_2O) nanowires are deposited with a cathodic current of 0.08 mA cm^{-2} in a 0.4 M copper sulphate ($CuSO_4$, Sigma-Aldrich) bath containing 3.0 M lactic acid ($CH3CH(OH)CO_2H$, Sigma-Aldrich). The pH value of the bath is carefully adjusted to 12.0 by the addition of 3.0 M sodium hydroxide (NaOH, Sigma-Aldrich). The temperature of the bath is controlled at 45 °C using a heating plate.

4.1.2.5 Deposition of MnO_2 nanotube

Manganese oxide (MnO_2) is deposited at a constant potential of 0.7 V from an aqueous solution of 0.1 M manganese acetate ($MnAC_2$. $4H_2O$, Sigma-Aldrich) and 0.1 M sodium sulfate (Na_2SO_4, Sigma-Aldrich). The potential is measured versus an Ag/AgCl reference electrode and a Pt foil is used for the counter electrode.

4.1.3 Electron beam physical vapor deposition

Electron beam physical vapour deposition is a form of physical vapour deposition, in which a target anode is bombarded with an electron beam given off by a charged tungsten filament under high vacuum.[165] The electron beam causes atoms from the target to transform into the gaseous phase. These atoms then precipitate into solid form, coating everything in the

vacuum chamber (within line of sight) with a thin layer of the anode material. In this dissertation, Ti and Au depositions are carried out using Kurt J. Lesker.

4.1.4 Electron beam lithography

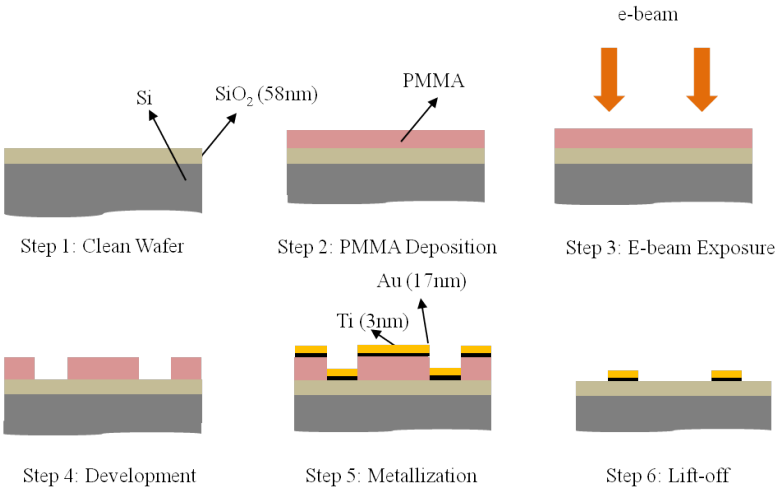

Figure 4-3. A standard EBL process for fabrication of electrode lines

Electron-beam lithography (EBL) is the practice of scanning a focused beam of electrons to draw custom shapes on a surface covered with an electron-sensitive film called a resist ('exposing'). The electron beam changes the solubility of the resist, enabling selective removal of either the exposed or non-exposed regions of the resist by immersing it in a solvent ('developing').[166] The purpose, as with photolithography, is to create very small structures in the resist that can subsequently be transferred to the substrate material, often by etching. The primary advantage of EBL is that it can draw custom patterns (direct-write) with sub-10 nm resolution. This form of maskless lithography has high resolution and low throughput, limiting its usage to photomask fabrication, low-volume production of semiconductor devices, and research & development.[167] In this dissertation, RAITH150 is used for the fabrication of electrode lines. A typical EBL process in this dissertation is shown in Figure 4-3.

4.1.5 Ion milling

In simple terms ion milling can be viewed as an atomic sand blaster. In place of actual grains of sand, submicron ion particles are accelerated and bombard the surface of the target work while it is mounted on a rotating table inside a vacuum chamber.[168] The target work is typically a wafer, substrate, or element that requires material removal by atomic sandblasting or dry ion etching. During the milling, Argon ions contained within plasma formed by an electrical discharge are accelerated by a pair of optically aligned grids. The highly collimated beam is focused on a tilted work plate that rotates during the milling operation. A neutralization filament prevents the build-up of positive charge on the work plate.

In this dissertation, the purpose of the ion milling is used to remove the barrier layer of AAO template, the TiO_2, ZnO and AZO layers on the surface of AAO template, as well as the overgrowth nanowires outside of AAO template. The common condition of the ion milling: angle of 60°C, energy power of 5 kV and rotation of 5 Hz. The ion milling rate for Al_2O_3, TiO_2, ZnO and AZO is about 5.0 nm min^{-1}. All the ion millings in this dissertation are carried out using Gatan PECS^{TM} (model 682).

4.2 Analysis instruments

4.2.1 Field emission scanning electron microscopy

Field emission is the emission of electrons from the surface of a conductor caused by a strong electric field. An extremely thin and sharp tungsten needle (tip diameter 10–100 nm) works as a cathode.[170] The FE source reasonably combines with scanning electron microscopes (SEMs) whose development has been supported by advances in secondary electron detector technology. The acceleration voltage between cathode and anode is commonly in the order of magnitude of 0.5 to 30 kV, and the apparatus requires an extreme vacuum (~10^{-6} Pa) in the column of the microscope. Because the electron beam produced by the FE source is about

1000 times smaller than that in a standard microscope with a thermal electron gun, the image quality will be markedly improved; for example, resolution is on the order of ~2 nm at 1 keV and ~1 nm at 15 keV. Therefore, the FE scanning electron microscope (FE-SEM) is a very useful tool for high resolution surface imaging in the fields of nanomaterials science. Meanwhile, energy-dispersive detector X-rays (EDX) emitted from the sample as a result of the high-energy electron beam penetrating into the sample. X-ray spectra can be collected and analyzed, yielding quantitative elemental information about the sample. A "standardless" routine is utilized, which yields an accuracy of 1-2% and sensitivities for some elements down to 0.1 weight percent. Line scanning and x-ray mapping can also be generated. The SEM, TEM lamella preparation, and part of EDX measurements in this dissertation are conducted using Auriga Zeiss FIB system equipped with Oxford detector.

4.2.2 Transmission electron microscopy

Transmission electron microscopy (TEM) is a microscopy technique, in which a beam of electrons is transmitted through an ultra-thin specimen, interacting with the specimen as it passes through.[171] An image is formed from the interaction of the electrons transmitted through the specimen; the image is magnified and focused onto an imaging device, such as a fluorescent screen, on a layer of photographic film, or to be detected by a sensor such as a CCD camera.

TEMs are capable of imaging at a significantly higher resolution than light microscopes, owing to the small de Broglie wavelength of electrons. This enables the instrument's user to examine fine detail-even as small as a single column of atoms, which is thousands of times smaller than the smallest resolvable object in a light microscope. TEM forms a major analysis method in a range of scientific fields, in both physical and biological sciences. TEMs find application in cancer research, virology, materials science as well as pollution, nanotechnology, and semiconductor research.

At smaller magnifications TEM image contrast is due to absorption of electrons in the material, due to the thickness and composition of the material. At higher magnifications complex wave interactions modulate the intensity of the image, requiring expert analysis of observed images. Alternate modes of use allow for the TEM to observe modulations in chemical identity, crystal orientation, electronic structure and sample induced electron phase shift as well as the regular absorption based imaging. The TEM measurements in this dissertation are carried out using Philips Tecnai transmission electron microscope.

4.2.3 Electrochemical workstation

Electrochemical workstation is fundamental to modern electrochemical studies using three electrode systems for investigations of reaction mechanisms related to redox chemistry and other chemical phenomena.[172] The dimensions of the resulting data depend on the experiment. In voltammetry, electric current in amps is plotted against electric potential in voltage. In a bulk electrolysis total coulombs passed (total electric charge) is plotted against time in seconds even though the experiment measures electric current (amperes) over time. This is done to show that the experiment is approaching an expected number of coulombs.

All the electrodeposition experiments, the performance characterization of supercapacitors and photoelectrochemical electrodes in this dissertation are conducted using the electrochemical workstation (BioLogic, Inc.)

4.2.4 Solar simulator and Quantum efficiency measurement system

A solar simulator (also artificial sun) is a device that provides illumination approximating natural sunlight. The purpose of the solar simulator is to provide a controllable indoor test facility under laboratory conditions, used for the testing of solar cells, sun screen, plastics, and other materials and devices.

In this dissertation, the light source used is Oriel solar simulator (300 W Xe lamp, AM 1.5 global filter). It is calibrated to 1 sun (100 mW cm^{-2}) by a Si photodiode (Model 818, Newport). Optical filter (420 nm and 550 nm cut off) are used in front of the AM 1.5G for different wavelength range requirement. The Incident photon to charge carrier efficiency (IPCE) of the devices is measured without applying bias using QEPVSI-b Quantum Efficiency Measurement System (Newport). Measurements are recorded with chopped illumination (20 Hz) and no external bias was applied during the measurements to get a pure photocurrent signal. The output current signal was connected to a Merlin digital lock-in radiometry system and the output signal from the lock-in amplifier was fed into a computer controlled by TRACQ BASIC software.

4.2.5 UV-Vis absorbance spectroscopy

Ultraviolet–visible spectroscopy (UV-Vis) refers to absorption spectroscopy or reflectance spectroscopy in the ultraviolet-visible spectral region.[173] This means it uses light in the visible and adjacent (near-UV and near-infrared [NIR]) ranges. The absorption or reflectance in the visible range directly affects the perceived color of the chemicals involved. In this region of the electromagnetic spectrum, molecules undergo electronic transitions. This technique is complementary to fluorescence spectroscopy, in that fluorescence deals with transitions from the excited state to the ground state, while absorption measures transitions from the ground state to the excited state. In this dissertation, the UV-Vis measurements are carried out on Varian Cary 5000 UV-Vis-NIR spectrophotometer.

4.2.6 Transient absorbance spectroscopy

Transient-absorption spectroscopy, also known as flash spectroscopy, is an extension of absorption spectroscopy.[174] Ultrafast transient absorption spectroscopy, an example of non-linear spectroscopy, measures changes in the absorbance/transmittance in the sample. Here,

the absorbance at a particular wavelength or range of wavelengths of a sample is measured as a function of time after excitation by a flash of light. In a typical experiment, both the light for excitation ('pump') and the light for measuring the absorbance ('probe') are generated by a pulsed laser. If the process under study is slow, then the time resolution can be obtained with a continuous (i.e., not pulsed) probe beam and repeated conventional spectrophotometric techniques.

Time resolved absorption spectroscopy relies on our ability to resolve two physical actions in real time. The shorter the detection time, better would be the resolution. That's why femto-second laser based spectroscopy offers better resolution than nano-second laser based spectroscopy. In a typical experimental set up, a pump pulse excites the sample and later, a delayed probe pulse strikes the sample. In order to maintain the maximum spectral distribution, two pulses are derived from the same source. The impact of the probe pulse on the sample is recorded and analyzed with wavelength/time to study the dynamics of the excited state.

Absorbance (after probe) - Absorbance (after pump) = Δ Absorbance

Δ Absorbance records any change in the absorption spectrum as a function of time and wavelength. As a matter of fact, it reflects ground state bleaching (-ΔA), further excitation of the excited electrons to higher excited states (+ΔA), stimulated emission (-ΔA) or product absorption (+ΔA). Bleaching of ground state refers to depletion of the ground state carriers to excited states. Stimulated emission follows the fluorescence spectrum of the molecule and is Stokes shifted relative to bleach signal. Product absorption refers to any absorption changes caused due to formation of intermediate reaction products. TA measurements can also be used to predict non emissive states and dark states unlike time resolved photoluminescence.

Transient absorption can be measured as a function of wavelength or time. The TA curve along wavelength provides information regarding evolution/decay of various intermediate

species involved in chemical reaction at different wavelengths. The transient absorption decay curve against time contains information regarding the number of decay processes involved at a given wavelength, how fast or slow the decay processes are. It can provide evidences with respect to inter-system crossing, intermediate unstable electronic states, trap states, surface states etc. In this dissertation, the TA measurements are carried out using the spectroscopy in Prof. Jure Demsar group.

4.2.7 Simulation software

4.2.7.1 COMSOL Multiphysics

Using COMSOL Multiphysics provides you with a significant amount of physics modeling functionality, including multiphysics ability. By adding application-specific modules, the modeling power is increased with dedicated tools for electrical, mechanical, fluid flow, and chemical applications. COMSOL Multiphysics includes a set of core physics interfaces for common physics application areas such as structural analysis, laminar flow, pressure acoustics, and transport of diluted species, electrostatics, electric currents, heat transfer, and Joule heating.

In this dissertation, in order to understand the mechanism of unique binary-pore template formation, COMSOL is used to simulate the electric filed distribution during different stages of anodization. We assumed that the cell boundaries are approximate circulars for all COMSOL simulation models, where geometric domain is based on SEM images of the square and hexagonal templates. The potential drops in electrolyte by concentration polarization, mass transport, and/or interfacial double layer are negligible because of high conductivity of the electrolyte and high resistance of the alumina barrier layer. A much stronger electric field (E-field) is built up at the residual metal/oxide interfaces, indicating the enhancement in the chemical reactions related to the formation and dissolution of the

template. In order to reveal the possibility of relatively weak E-field at the unprinted fourfold and triple junction sites of A-pores, the scale bars of the E-fields are decreased correspondingly.

4.2.7.2 FDTD Solutions

FDTD Solutions is a 3D Maxwell solver, capable of analyzing the interaction of UV, visible, and IR radiation with complicated structures employing wavelength scale features. FDTD Solutions empowers designers to confront the most challenging photonic design problems. Rapid prototyping and highly-accurate simulations reduce reliance upon costly experimental prototypes, leading to a quicker assessment of design concepts and reduced product development costs. FDTD Solutions can facilitate your success in diverse application areas, from fundamental photonics research to current industrial applications in imaging, lighting, biophotonics, photovoltaics, and many more.

In order to better understand the plasmonic effects of Au nanodot arrays prepared in this dissertation, FDTD is conducted to simulate the light absorption of Au nanodot arrays, which could support the experimental results as well as provide guidance for further optimization of the structure and composition.

4.3 Preparation of imprinted templates

(1) Al foil preparation: High-purity (99.99+%) aluminum foil of about 0.22 mm thickness is used as the starting material. The aluminum foil is first degreased with acetone, and then ethanol for 10 min, respectively; finally, it is electropolished in a 1:9 solution of perchloric acid and ethanol.

(2) Ni imprinting mold preparation: First, Silicon master mold with nanohole array (400 nm and 800 nm spacing, square- and hexagon-arranged, AMO GmbH) is cleaned in Piranha solution (H_2SO_4/H_2O_2; 3:1) for 30 min with ultrasonication. Surface modification is then

conducted by treating the Si master mold with 3-aminopropyltriethoxysilane (3-APTES; 1.0 vol% in CH_3CH_2OH) at 65 °C for 1h. After that, a 15 nm thick Au layer is evaporated on the surface of Si master mold by EBPVD. The Au layer is used as a conductive layer for subsequent Ni film electrodepostion. The Ni film electrodeposition is carried out in a Ni plating solution. The typical current density for the Ni electrodeposition is 10 $mAcm^{-2}$. After the electrodeposition, Ni imprinting mold with ordered nanorod array is obtained by stripping the Ni film from the Si master mold (Figure 4-4d), and the Si master mold can be recycling-used many times without noticable damages.

(3) Imprinted template preparation: The Ni imprinting mold is used for the imprinting process on Al foil. Typically, the imprinted Al foil is attained by applying a pressure of about 10 kN cm^{-2} for 3 min using an oil pressing system (Figure 4-4a and b). About 1 cm^2 nearly defect-free imprinted areas have been successfully obtained (Figure 4-4e), in which the formed concave pattern thereby as the initial sites to guide the template growth in the subsequent anodization. For the 400 nm spacing imprinted Al, the anodization is conducted under a constant voltage of 160 V in a H_3PO_4 solution (0.4 M) at 15°C, where the anodization voltage is chose to satisfy the linear relationship between the interpore distance and the anodization voltage (2.5 nmV^{-1}). The temperatures of Al foil and electolyte are controlled by a homemade cooling system (Figure 4-4c). After the anodization, square and hexagonal pore arrays with 400 nm spacing are obtained over the whole imprinted area (Figure 4-4f). For the 800 nm spacing imprinted Al, the anodizatin is carried out under a constant voltage of 320 V in a mixture solution (2.5 mL of 1.0 wt% H_3PO_4, 1:1 v/v% of 4.0 wt% citric acid and ethylene glycol) at 15 °C.

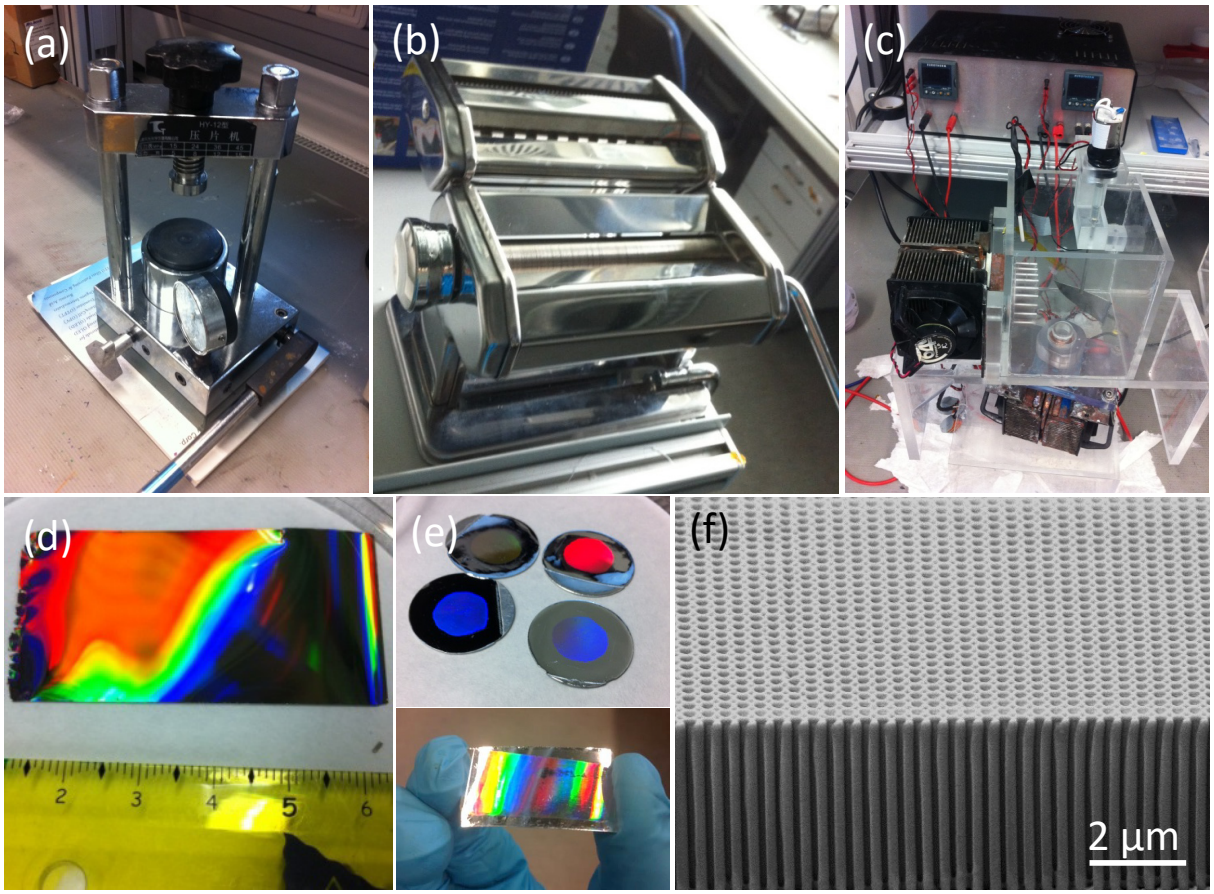

Figure 4-4. (a) Stamp imprinting system. (b) roller to roller imprinting system. (c) home-made cooling system. (d) Stripped Ni imprinting mold with ordered Ni nanorod array. (e) Imprinted Al foils with ordered concave patterns from the stamp (top) and roller to roller (down) imprinting systems. (f) Tilted SEM image of a square template with 400 nm interpore distance.

5 Results and discussions

In the following chapters, the concepts, strategies, features and devices of binary nano-structuring are systematically presented. The Section 5.1 presents the strategy to realize the distinctive binary-pore template. The profile of both nanopores, like the size and the shape, can be individually adjusted to a broad range. After that, the mechanism of binary-pore template formation is investigated and discussed in Section 5.2. The Section 5.3 reports the enormous binary nanostructure arrays that are synthesized by a combination of the binary-pore template and the well-established fabrication techniques. The Section 5.4 shows the template evolution from a binary-pore array to a quadruple-pore array under the same mechanism. The Section 5.5 demonstrates the device applications based on the binary nanostructure arrays. The multi- or superior-functionalized macroscopic ('Z-scheme' artificial photosynthesis system) and nanoscopic (addressable multi-gates nanowire transistor) devices are successfully explored. Optimization of the single 'array' is critical for improving the overall performance based on binary nanostructure arrays in the future. Therefore, the Section 5.6 presents the construction of Pt/MnO_2 core/shell nanotube array for enhancing the performance of supercapacitor. The Section 5.7 shows the building of nano-Au/PZT hybrids for manipulation of plasmonic from Au nanodot array and then improving the performance of PEC.

5.1 Binary-pore template

5.1.1 Synthesize of binary-pore template

Binary-pore template is originated from the squarely imprinted template. After obtained the squarely imprinted template with anodization, an innovative selective etching is utilized to generate binary-pore template and the standard procedure is displayed in Figure 5-1. First, the

prepared Ni imprinting mold is used for the imprinting process on Al foil. About 1 cm^2 nearly defect-free imprinted areas have been successfully obtained, in which the formed concave

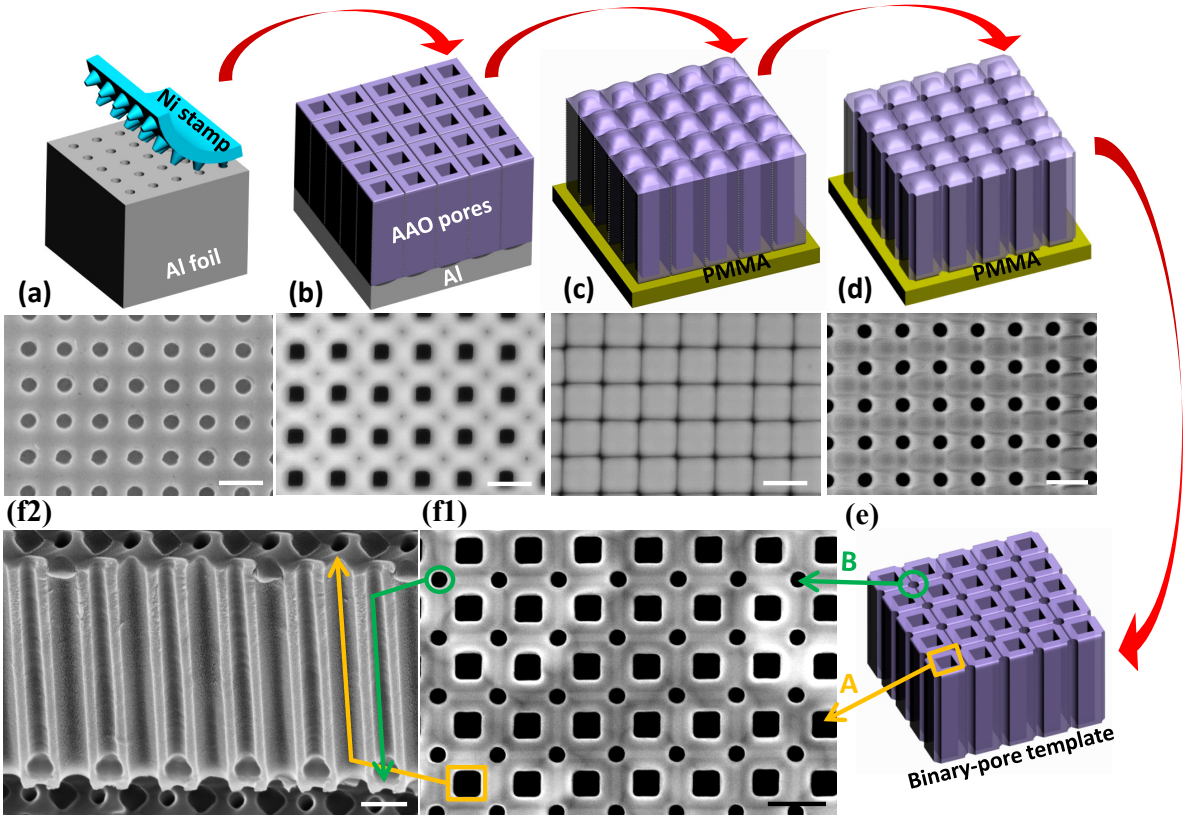

Figure 5-1. Schematic illustration of binary-pore template fabrication process and the relevant SEM images: (a) imprinting on Al foil to form concave array; (b) anodization on imprinted Al foil to obtain square-shaped A-pores; (c) coating PMMA on template, reversing it and removing backside unoxidized Al to expose barrier layer of A-pores; (d) selective etching on barrier layer of A-pores to attain round-shaped B-pores; (e) removing barrier layer of A-pores with ion milling to realize binary-pore template; (f1) top-view of a typical binary-pore template, with two sets of square-shaped A-pore array and round-shaped B-pore array; (f2) cross-sectional view of binary-pore template, showing that both A-pores and B-pores span over the whole template thickness.

pattern thereby as the initial sites to guide the template growth in the subsequent anodization (Figure 5-1a). Second, the anodization is conducted under a constanta voltage of 160 V in a H_3PO_4 solution. After a 15 min anodization, a squarely imprinted template with identically

square-shaped nanopores is obtained over the imprinted area and they are denoted as 'A-pores' (Figure 5-1b). Third, PMMA solution is poured on the surface of the resultant template and a PMMA layer is formed after 20 min baking under 90 °C, which not only acts a supporting layer to avoid the AAO template from broking during the handling, but also prevents unnecessary chemical etching on the top of template. After that, the barrier layer of A-pores appears after removing the unoxidized Al foil in a mixed solution (3.4 g copper chloride, 100 mL hydrochloric acid and 100 mL deionized water) (Figure 5-1c). Fourth, the AAO template is immersed in 0.1 M NaOH solution for 40 min, and then a uniformly round-shaped nanopore array (denoted as 'B-pores') with the size of 126 nm is appeared at the fourfold junction sites of A-pores (Figure 5-1d). A typical binary-pore template is revealed after removing the A-pore barrier layer with ion milling (Figure 5-1e). The square-shaped A-pores are originated from the anodization (indicated by the yellow arrows in Figure 5-1f1 and f2), while the round-shaped B-pores are generated from the selective etching in 0.1 M NaOH solution at the different step (indicated by the green arrow in Figure 5-1f1 and f2), respectively.

Particularly, the detailed morphology of the binary-pore template has been investigated in Figure 5-1d, and a distinctive barrier layer structure is found (Figure 5-2). So far, for all existing AAO templates (normal anodized, hexagonal, or square imprinted),[55] the pores have the same hemispherical-shaped barrier layers located at the bottom of pores. For the binary-pore template, besides the normal barrier layer of A-pores at one side of template (bottom side), the B-pores have flat-disc shaped barrier layers at the opposite side of template (top side). This means that the A-pore and the B-pore are blocked at one end of the pore by its own barrier layer at the different side of template, while the other end of pore is opened at the opposite side. This unique construction could provide huge flexibility for realizing the diverse binary-pore template and the subsequent binary nanostructure arrays.

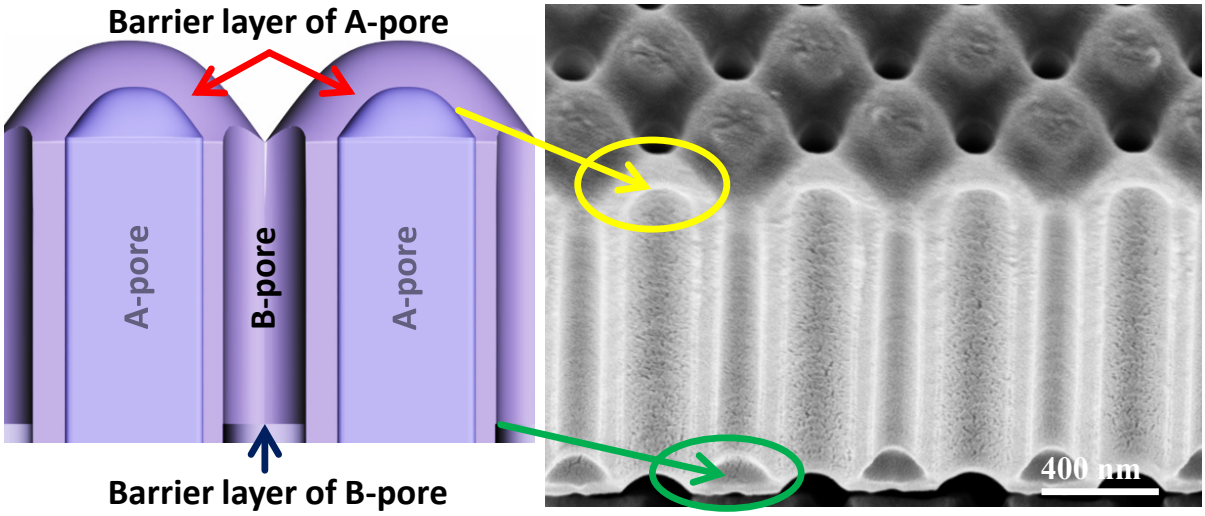

Figure 5-2. Cross-sectional morphology of a squarely imprinted template after the etching in 0.1 M NaOH: A-pore has a hemispherical-shaped barrier layer, similar to the barrier layer of conventional AAO template; B-pore has its own barrier layer with a distinct flat-disc shape. Two barrier layers are located at the opposite sides of template.

5.1.2 Modulation of binary-pore template

5.1.2.1 Tuning size of A-pores and B-pores

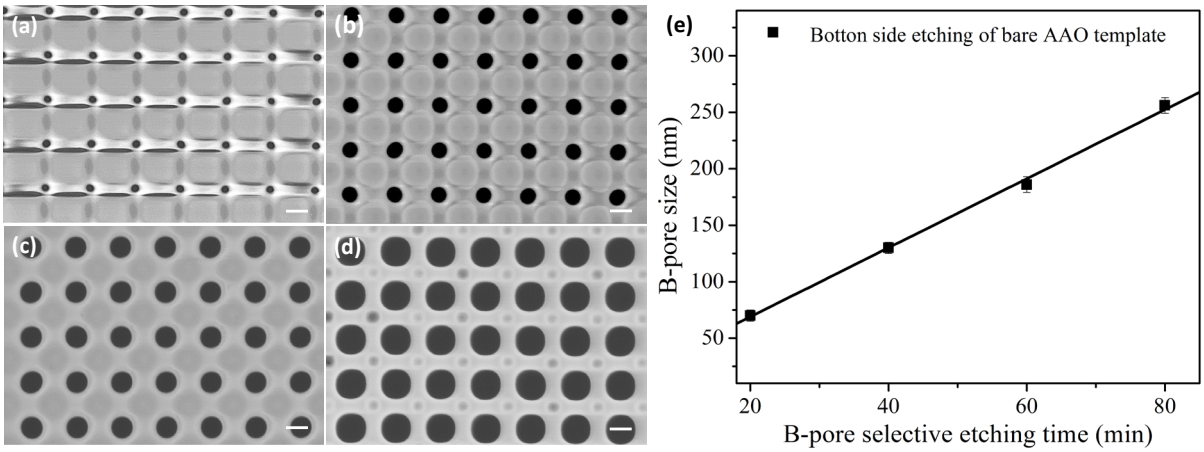

Figure 5-3. SEM images of the bare template after different selective etching times in 0.1 M NaOH solution: (a) 20 min, (b) 40 min, (c) 60 min, and (d) 80 min. (e) Dependence of the B-pore size on the selective etching time. Scale bar: 200 nm.

The size of both binary-pores can be adjusted individually and precisely, which is feasible based on the opposite barrier layer structures (*i.e.*, adjusting B-pore size while fixing the A-pore size by preventing the etching solution from going into A-pores at the opposite side, and vice versa). The B-pores, on one hand, can be tuned largely in 0.1 M NaOH solution with different etching times. When the selective etching is conducted at the bottom side of bare template, the size of B-pores is enlarged linearly from 71 nm to 265 nm with the increasing of etching time from 20 min to 80 min (Figure 5-3). The etch rate of the bare template is about 3.2 nm/min (Figure 5-3e). Moreover, the B-pore size can be tuned even larger until the A-pore barrier layer keeps intact during the selective etching process.

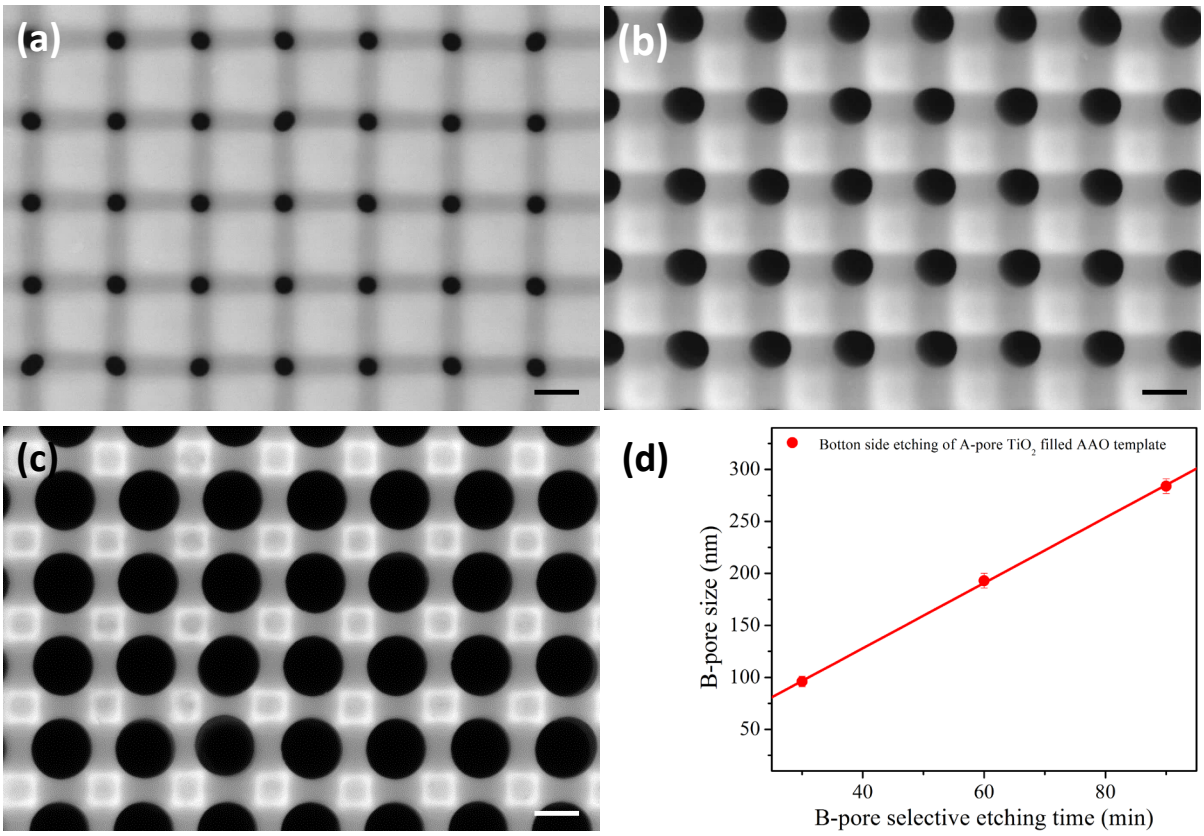

Figure 5-4. SEM images of the bottom side of A-pore TiO_2 filled template after different etching times in 0.1 M NaOH solution: (a) 30 min, (b) 60 min and (c) 90 min. (d) Dependence of the B-pore size on the selective etching time. Scale bar: 200 nm.

The selective etching is also carried out at the bottom side of A-pore TiO_2 filled template (Figure 5-4). The size of B-pores is enlarged linearly from 95 nm to 282 nm with the increasing of etching time from 30 min to 90 nm. The etch rate of the A-pore TiO_2 filled template is about 3.1 nm/min, which is almost the same as that for the bare template. Those results indicated that the operations or modifications for A-pores have no effect on the B-pores because of the protection from A-pore barrier layer.

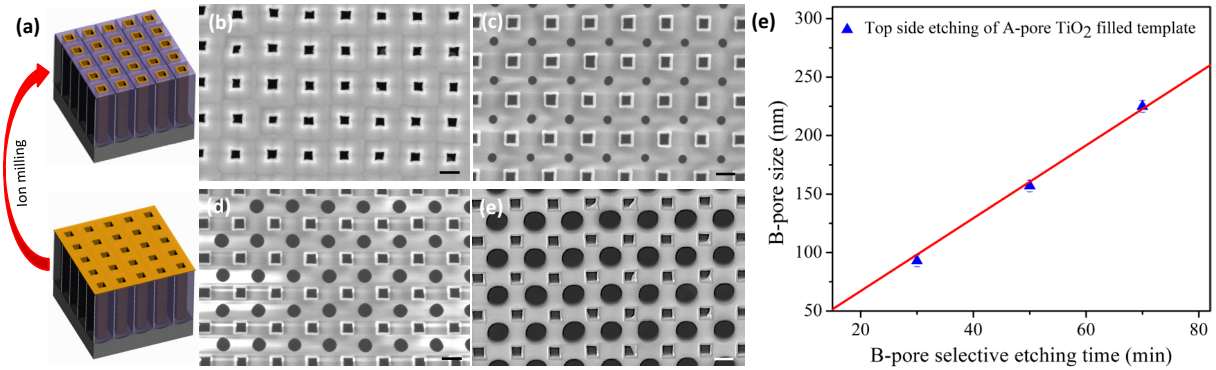

Figure 5-5. (a) Illustration of ion milling on A-pore TiO_2 filled template. Based on the ion milling rate of Al_2O_3 (5 nm min^{-1}) and TiO_2 (5 nm min^{-1}), about 45 min is required to completely remove the TiO_2 film and the barrier layer of B-pores on top surface of template. SEM images of the binary-pore template after different etching times in 0.1 M NaOH solution: (b) 0 min, (c) 30 min, (d) 50 min, and (e) 70 min. (f) Dependence of the B-pore size on the selective etching time. Scale bar: 200 nm.

In order to prove the controllability of the selective etching, the etching is further conducted on the top side of A-pore TiO_2 filled template, where an ion milling is used first to remove the thin TiO_2 layer and B-pore barrier layer on template surface. The TiO_2 nanotubes in A-pores can protect the A-pores away from the etching solution. From the SEM images and curve in Figure 5-5, the size of B-pores is increased linearly from about 92 nm to 225 nm with the etching time from 30 to 70 min, and the etch rate on the top side of template is almost the same that at the bottom side of template.

On the other hand, the A-pores can be precisely controlled as well. With a pore widening in a 5 wt% H_3PO_4 solution, the A-pores are enlarged from 125 nm to 260 nm with the time increasing from 20 to 80 min, while the variation of the B-pores is limited to 7 nm when all the samples are etched in the 0.1 M NaOH solution for 40 min at the relevant step (Figure 5-6). The widening rate of A-pore is about 1.7 nm/min, and the A-pore size can be enlarged to even larger without affect the B-pores because of the protection from the B-pore barrier layer.

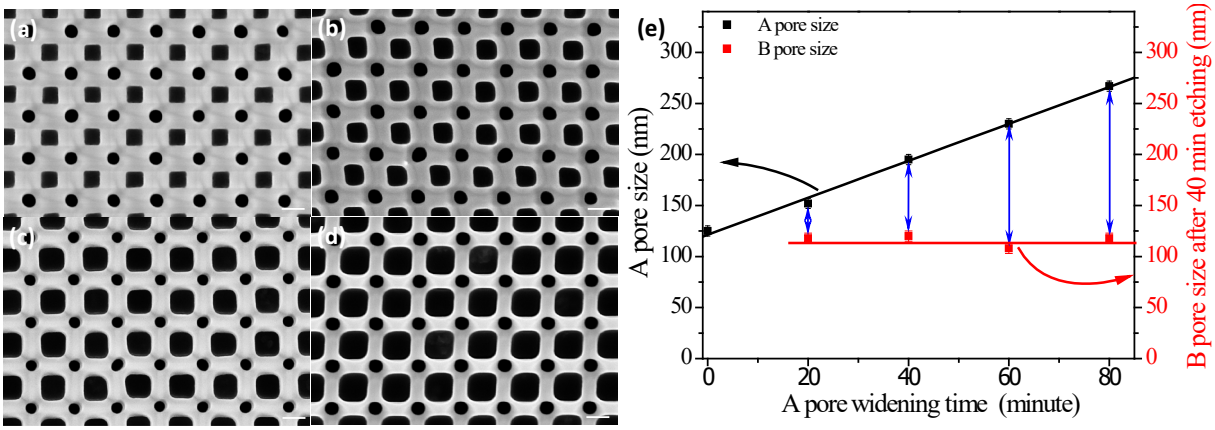

Figure 5-6. SEM images of binary-pore templates after sequential steps: first, immersing the top side of template in 5 wt% H_3PO_4 for widening A-pores with different times: (a) 20 min, (b) 40 min, (c) 60 min, and (d) 80 min; then selective etching the bottom side of templates in 0.1 M NaOH solution for 40 min to obtain the B-pores; finally, ion millings are used to remove the barrier layers of A-pores for the SEM observation. Scale bar: 200 nm.

5.1.2.2 Transforming morphology of B-pores

In an attempt to access more morphology controllability of binary-pore templates, a sequential-step process is innovated for modifying the B-pores, which includes a 30 min selective etching in 0.1 M NaOH and a pore widening in 5 wt% H_3PO_4 solution. Consequently, the B-pores are transformed from round shape to crosshair shape with a pore widening, and the branches of the crosshair can be enlarged and sharped with the increasing of widening time (Figure 5-7).

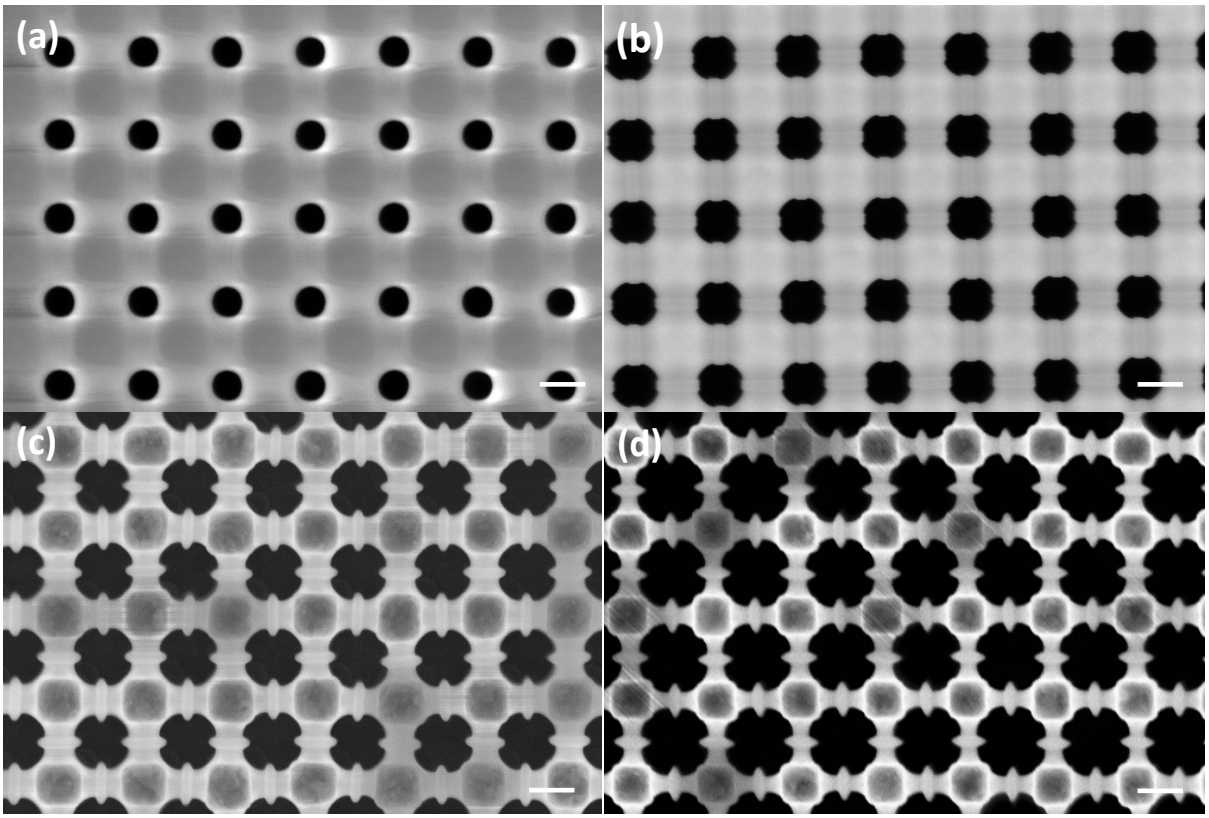

Figure 5-7. Transformation of B-pore shape after a 30 min selective etching in 0.1 M NaOH solution and then different widening times in 5 wt% H_3PO_4 solution: (a) 0 min, (b) 30 min, (c) 90 min, (d) 120 min. Scale bar: 200 nm.

It is well established that anionic impurity, such as SO_4^{2-}, $C_2O_4^{2-}$, PO_4^{3-}, will incorporate inside the pore wall during anodization, and thus the outside impurity layer of the pore wall will dissolve much quickly than the inner pure layer in 5 wt% H_3PO_4 solution.[35, 175] Thus, the unique morphologic transformation of B-pores is ascribed to the double layer characteristic of the pore wall that results in different etch rates in the H_3PO_4 solution. From the TEM images, EDX linear scanning and mapping of the pore wall in Figure 5-8, they reveal the existence of double layers inside the pore wall that the inner layer is a pure Al_2O_3 layer and the outside is a P ion incorporated Al_2O_3 layer. The ratio of the pure Al_2O_3 layer versus the P ion incorporated Al_2O_3 layer is about 1:4, which is close to the value from the

conventional anodization in H_3PO_4 solution.[176] This could well support the morphologic transformation of B-pores.

Concerning the above results, the binary-pore template with highly structural controllability of both A- and B-pore individually can be successfully obtained by using a selective etching, a pore widening or a combination of both processes at the relevant steps.

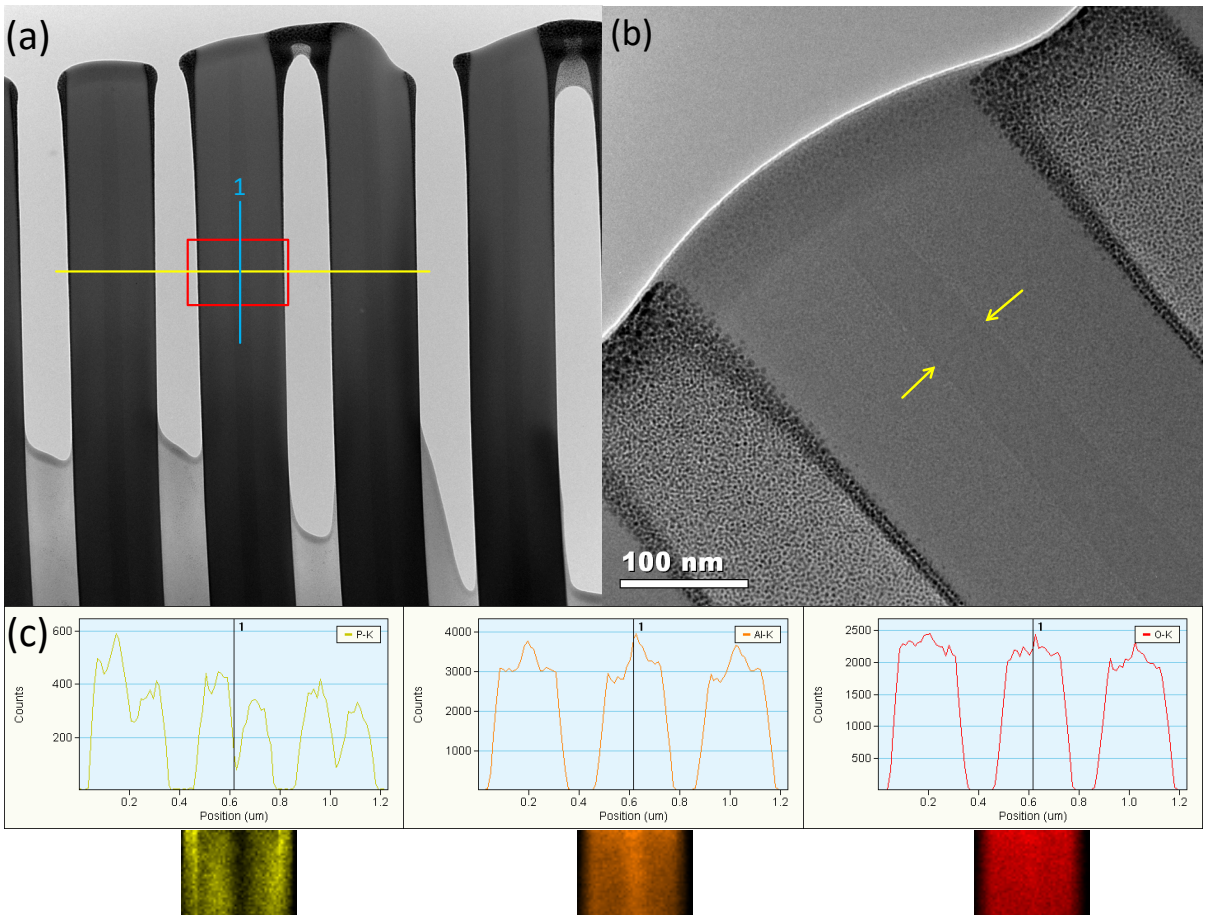

Figure 5-8. (a) and (b): Cross-sectional TEM images of a squarely imprinted template, showing that the pore wall is consisted by double layers. (c) EDX linear scanning and mapping of the pore wall, which demonstrates the distributions of P, O and Al elements, respectively.

5.2 Mechanism of binary-pore formation

In order to gain insight into the formation mechanism of the binary-pore template, a detailed

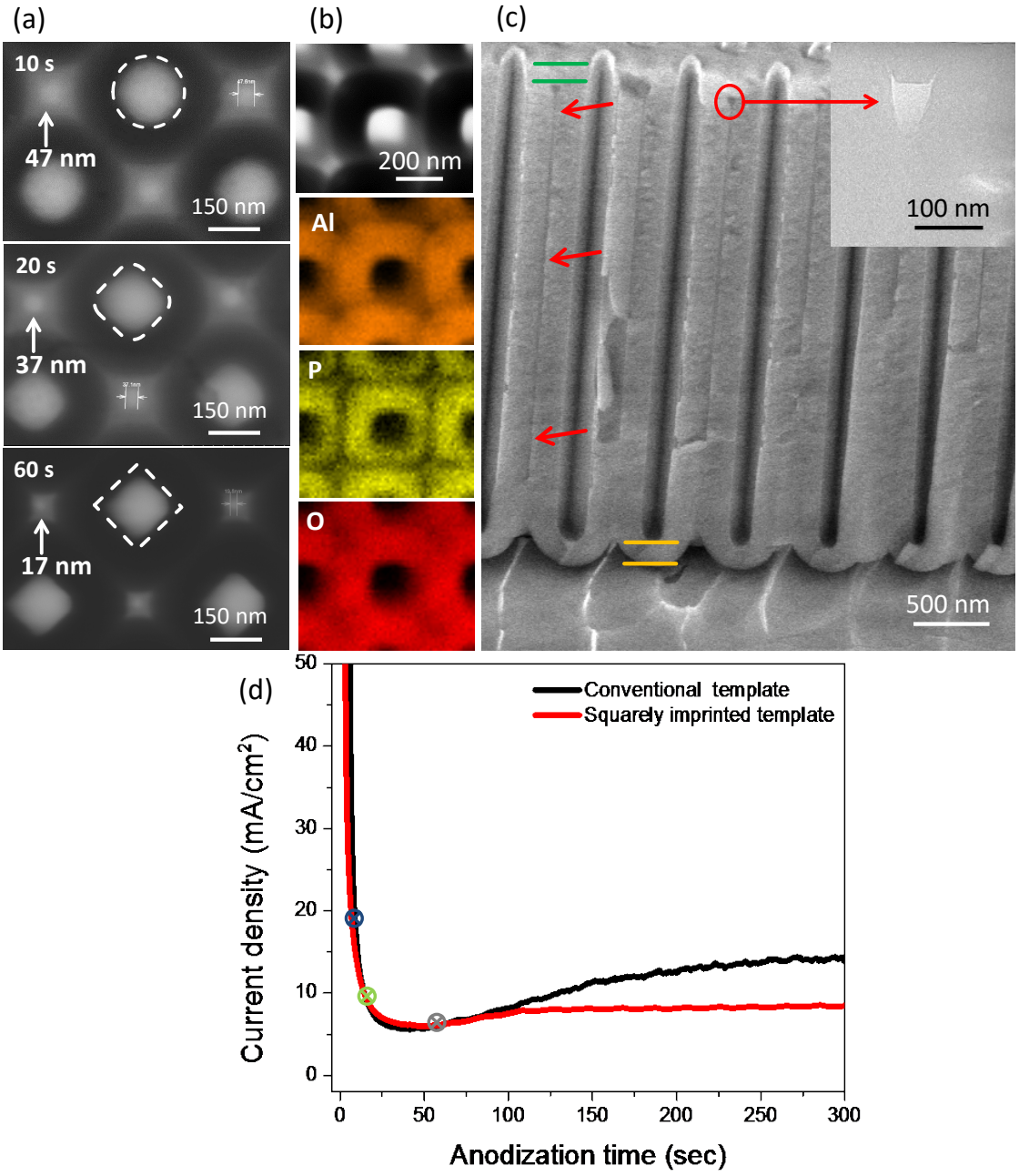

Figure 5-9. (a) STEM images of stripped template at different anodization stages: 10 s, 20 s and 60 s. (b) EDX mappings of the template (60 s), where the distribution of Al, P and O elements are labelled as orange, yellow and red color, respectively. (c) Cross-sectional SEM image of a 20 min anodizated template, in which the narrow B-pore is indicated by the red arrows, and the barrier layer of the B-pore and A-pore are labelled as green and yellow lines, respectively. Inset TEM image shows the enlarged view of the inverted pyramid void. (d) Transient current density of anodization at a constant voltage of 160 V as a comparing for squarely imprinted Al and conventional electropolished Al, respectively.

investigation of the anodization process and the relevant microstructures are carried out. Figure 5-9a shows STEM images of stripped template at different stages. At the very initial stage of anodization (10 s), the arrangement of round-shaped A-pores corresponds to that of the imprintedsites on Al foil. Noteworthily, brightly round-shape spots with size of approximately 47 nm are also observed at the fourfold junction site of A-pores, which implies the existence of small voids. When the anodization time reaches to 20 s, the A-pores expand around the imprinted sites and the pore morphology changes from round to quasi-square. Meanwhile, the small voids shrink to around 37 nm. When the transient current closely reaches the final steady state after a 60 s anodization (Figure 5-9d), the A-pores turn out to be square shape. While the small voids continuously shrink to 17 nm, and it will retain during the whole anodization process (Figure 5-1b). Existence of small voids is also supported by the EDX mapping of the 60 s anodized template in Figure 5-9b, where the intensity of Al, P and O elements at the center site of pore wall is relatively lower than that of the surrounding pore wall. However, these small voids are just shallow pores on template surface, which is revealed by a cross-sectional SEM image in Figure 5-9c. It shows that a barrier layer exists under the shallow pores (indicated by the green lines and defined as the B-pore barrier layer), and the actual B-pore is composed by an inverted pyramid void and a narrow pore beneath the B-pore barrier layer (indicated by red cycle and arrows). The thickness of B-pore barrier layer is maintained around 170 nm, close to the value of A-pore barrier layer at the bottom (indicated by the yellow lines).

An in-situ FIB cutting is carried out on an A-pore TiO_2 filled template and the typical SEM images are shown in Figure 5-10a to f. The inverted pyramid voids and barrier layer of B-pores can be observed at fourfold junction sites of A-pores. However, due to the small diameter of narrow B-pores and also the contamination from re-deposited or etched particles

and ions, the narrow B-pores below the pyramid void are too challenging to be revealed. Moreover, with the assistance of 3D reconstruction from the whole cut out area, the distributions of A-pores and the inverted pyramid voids are further confirmed (5-10g).

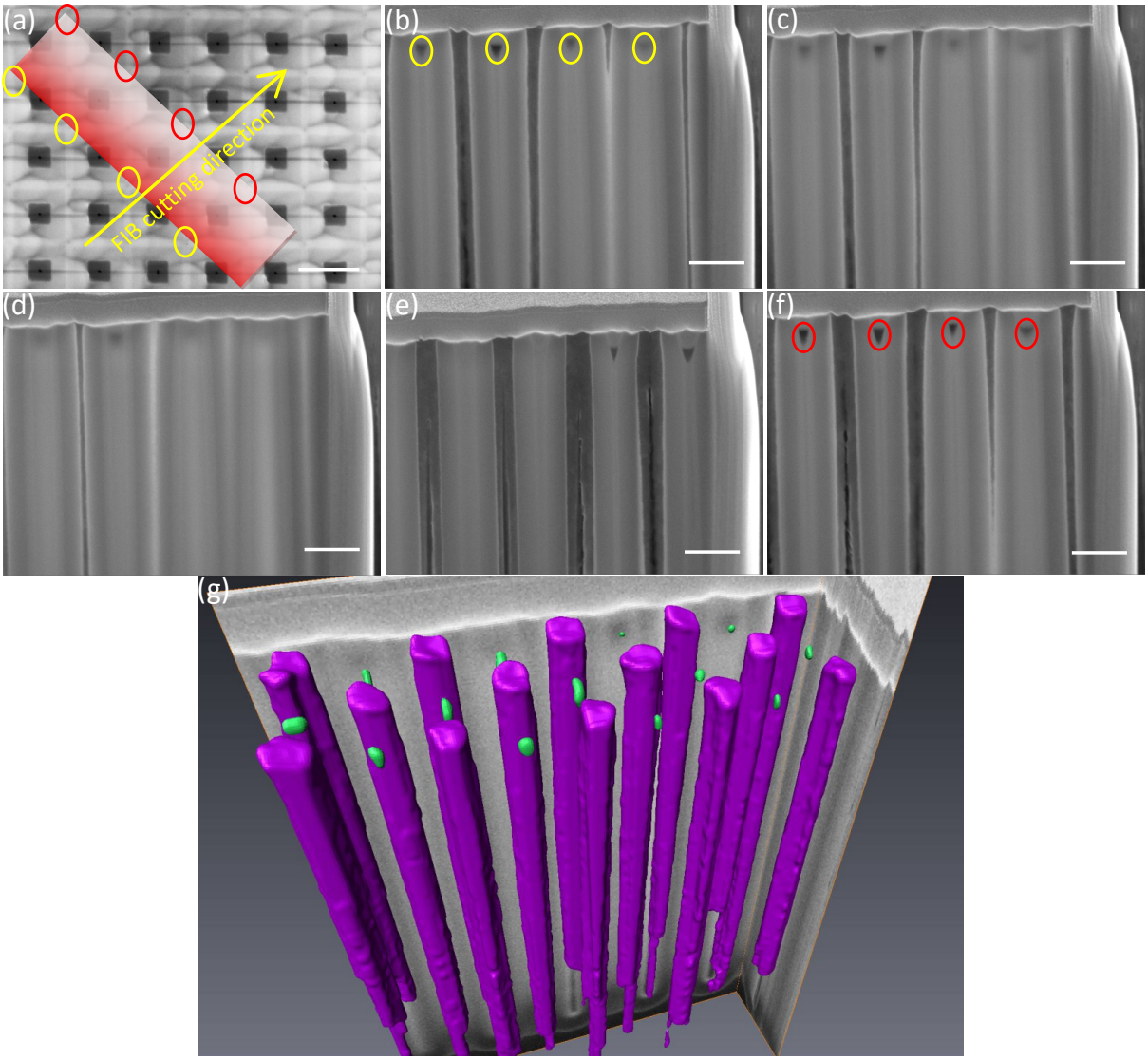

Figure 5-10. (a) FIB cutting direction on an A-pore TiO_2 filled template. (b-f) In-situ SEM image observation during the cutting process. (g) 3D reconstruction from the cut area. The distributions of A-pores and the inverted pyramid voids are indicated by purple and green colors, respectively. Scale bar: 400 nm.

A few models have been proposed with respect to the formation of pore structures, such as, joule's heat-induced chemical dissolution, field-assisted oxide dissolution, average field model, direct cation ejection model, and oxide plastic flow.[35] For more than sixty years, it is commonly accepted that field-assisted dissolution of oxide leads to pore formation, including the pre-patterned pore structures with different arrangements (e.g., triangle, square, diamond, and hexagon).[70, 76, 81, 82, 177-184] However, owning to the existence of B-pore barrier layer, the inverted pyramid void and narrow pore cannot accessed by the electrolyte, thereby the classical field-assisted dissolution mechanism is excluded for the formation of binary-pore structure. Recently, based on the dual-scale AAO template, Oh and Thompson proposed that the field-induced and strain-induced instabilities in the oxide film accounts for the formation of pore structure.[185] Therefore, the binary-pore structure in our case might ascribe to the combined effects of electric-field (E-field) and mechanical stress field around the imprinted concave sites during different period of anodization. The E-field induced instability plays dominate role at the very initial period to form the A-pores and the shallow pores at the fourfold junction sites of A-pores, which is supported by the simulations based on COMSOL Multiphysics. It is found that the imprinted Al shows a non-uniform electric field distribution, and the highest E-field strength (8×10^8 V/m) locates at the imprinted concave bases to form A-pores (Figure 5-11a1 and a2). Meanwhile, relatively strong E-field strength (3×10^8 V/m) is also observed at the fourfold junction site of A-pores, indicating the possibility of shallow pore formation. However, the morphology transformation of A-pores from round shape to square shape is finished in 60 s (Figure 5-9d), which results in a strong mechanical instability associated with the plastic deformation and flow of the oxide during this period. This is well agreed by the formation of inverted pyramid void beneath the B-pore barrier layer. After that, the mechanical constraints between the neighboring A-pores become dominate, and then the formation of A-pores as well as narrow B-pores is related to the rate of oxide plastic flow.

Meanwhile, the E-field assisted dissolution is ignorable during the steady-state growth. The reason is that though the E-field is as high as 1.7×10^{9} V/m at the fourfold junction sites of A-pores (Figure 5-11b1 and b2), the thickness of B-pore barrier layer keeps close to that of the A-pores even after 20 min anodization (Figure 5-9c).

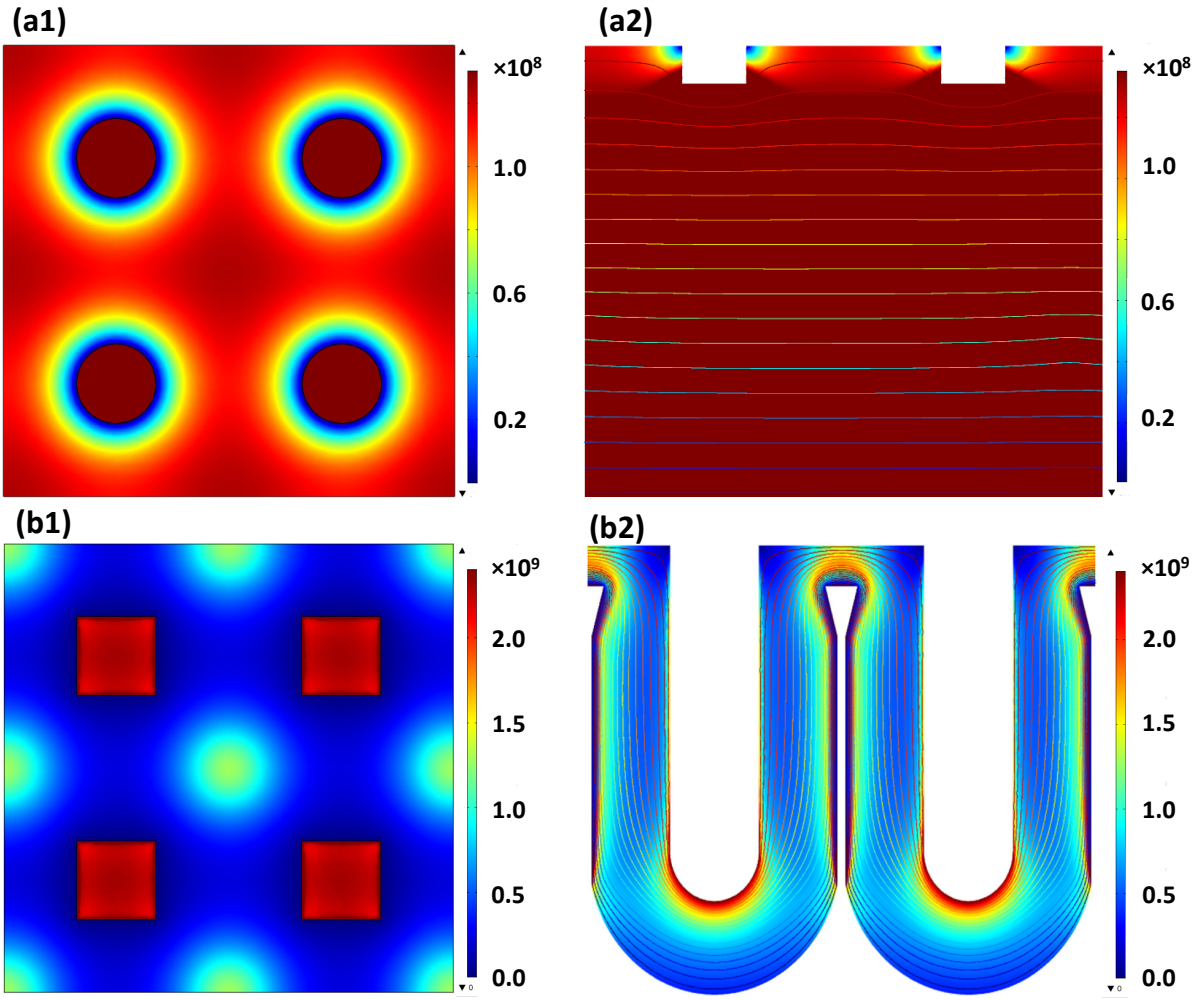

Figure 5-11. COMSOL simulated E-field distributions on a squarely imprinted Al foil: top-down (a1) and cross-sectional (a2) views at very initial stage of anodization, and top-down (b1) and cross-sectional (b2) views at steady state stage of anodization.

On the other hand, the E-field strength on imprinted hexagonal Al foil only focus on the bases of the concaves, while no strong E-field distribution is found at the triple cell junction sites (Figure 5-12a1 and a2). Consequently, no binary-pore template is attained from the hexagonal template with the identical anodization and selective etching processes, where only

A-pores can be obtained with a selective etching in a 0.1 M NaOH solution as well as with a pore widening in a 5 wt% H_3PO_4 solution (Figure 5-12 b1 and b2). This is also supported by immersing an A-pore TiO_2 filled hexagonal template in a 0.1 M NaOH solution that instead of generating new pores, only the TiO_2 nanotubes are exposed with the increasing of immersing times (Figure 5-12 c1 to c3).

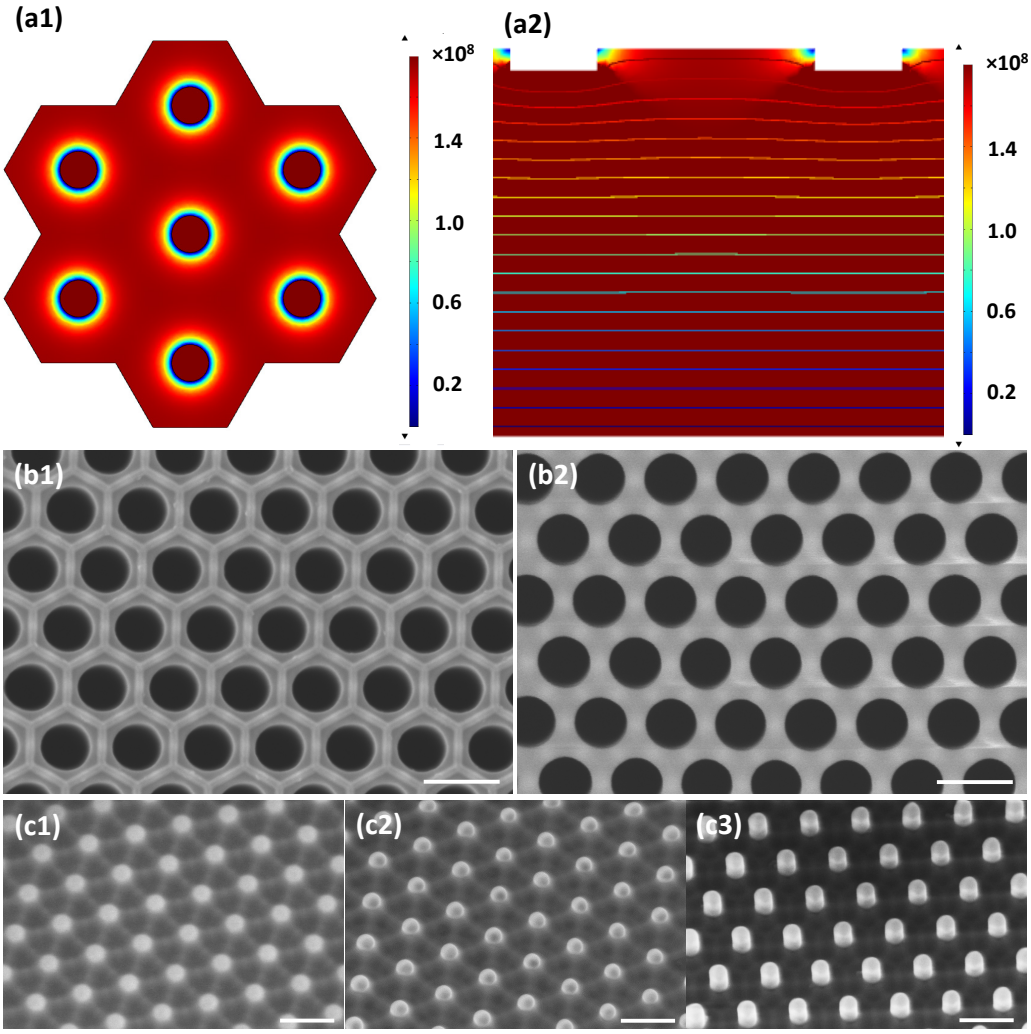

Figure 5-12. COMSOL simulated E-field distribution on a hexagonally imprinted Al foil at a very initial stage: top-down (a1) and cross-sectional (a2) views. SEM images of the bottom side of hexagonal templates: (b1) bare template after 90 min in 5 wt% H_3PO_4; (b2) bare template after 60 min in 0.1 M NaOH solution; (c1-c3) A-pore TiO_2 filled template after different immersing times (20 min, 40 min, and 60 min, respectively) in 0.1 M NaOH solution. Scale bar: 400 nm.

A further chemical etching process is also carried out in H_3PO_4 solution for thorough support this point. The bottom side of template is immersed in H_3PO_4 solution (5 wt%, 30°C) for different times, and we find out that the narrow B-pores barely enlarged even after 90 min immersing, largely different from the pore widening for the A-pores (Figure 5-13a and 5-13b). When the time increases to 2h, a few narrow B-pores become large, while others still keep intact, indicating that the widening rate of narrow B-pores in H_3PO_4 solution is extremely slow (Figure 5-13c). It is convinced that the alumina wall around the narrow B-pores is a pure layer and should not originate from the E-field enhanced oxide dissolution at the unprinted sites. Meanwhile, concerning the random size and morphology distributions of A-pores, the good controllability of H_3PO_4 solution for removing the bottom side barrier layer of square template will no longer exist as that happened to the hexagonal template.

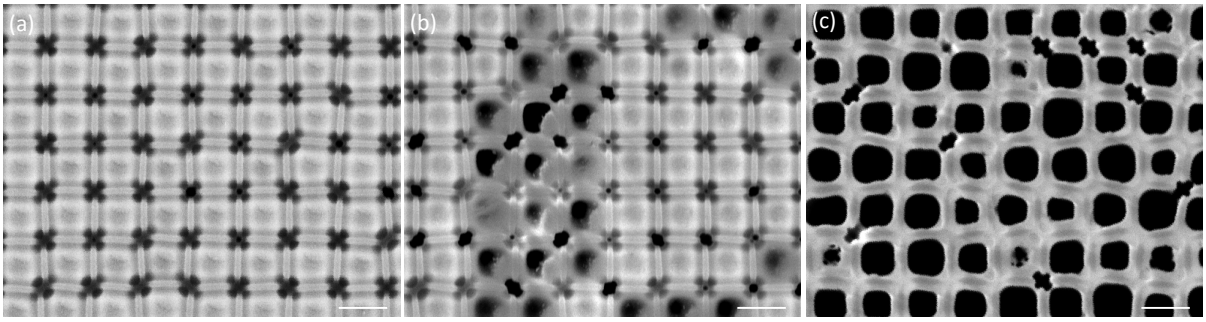

Figure 5-13. (a) SEM images of the bottom side of template after different widening times in 5 wt% H_3PO_4 solution at 30°C: (a) 60 min, (b) 90 min, and (c) 2 h, respectively. Scale bar: 400 nm.

5.3 Binary nanostructure arrays

Utilizing this binary-pore template, large-scale regular arrays of diverse binary nanostructures with morphologic versatility and high structural controllability are appreciable based on different well-established synthesizing approaches. By using only two of these approaches – electrodeposition and ALD processes, arrays of binary nanostructures including

nanowire/nanowire, nanowire/nanotube and nanotube/nanotube have been successfully obtained with different size, morphology and composition.

5.3.1 Fabrication of binary nanowire/nanowire arrays

The preparation details of binary Ni/Ag nanowire/nanowire arrays:

(1). An imprinted template is obtained with 15 min anodization and then an ion milling is used to remove the B-pore barrier layer on top surface of template (Figure 5-14a).

(2). A thin Ti/Au (10/30 nm) layer is evaporated on template surface as a conductive layer for electrodepositing of a thick Ni supporting layer in the Ni plating solution (Figure 5-14b).

(3). The backside unoxidized Al is removed in a mixed solution (3.4 g copper chloride, 100 mL hydrochloric acid and 100 mL deionized water). Then, the template is immersed in 0.1 M NaOH for 40 min to grow B-pores (Figure 5-14c).

(4). Ni nanowires are grown into the B-pores with a current density of 1 mA cm^{-2} for 10 min in the same Ni plating solution. After that, in order to protect the Ni nanowires from the next-step electrodeposition, the top ends of Ni nanowires and the barrier layer of A-pores are fully covered with a 30 nm Al_2O_3 layer by ALD (300 cycles, 100°C). A key is that the length of the Ni nanowires should be slightly shorter than the pore depth of B-pores (*i.e.*, the top of nanowires is slightly lower than the pore-end), so that the Al_2O_3 layer on the top of Ni nanowires will not be etched away by ion milling (Figure 5-14d).

(5). After the Al_2O_3 layer and A-pore barrier layer are removed by ion milling, A-pores are exposed to Ag plating solution for growth of Ag nanowires (with a current density of 1 mA cm^{-2} for 12 min), while the tops of round Ni nanowires are still covered by the Al_2O_3 layer (Figure 5-14e).

(6). Binary Ni/Ag nanowire/nanowire arrays are obtained after dissolving the template and the Al_2O_3 layer in 1.0 M NaOH solution (Figure 5-14f).

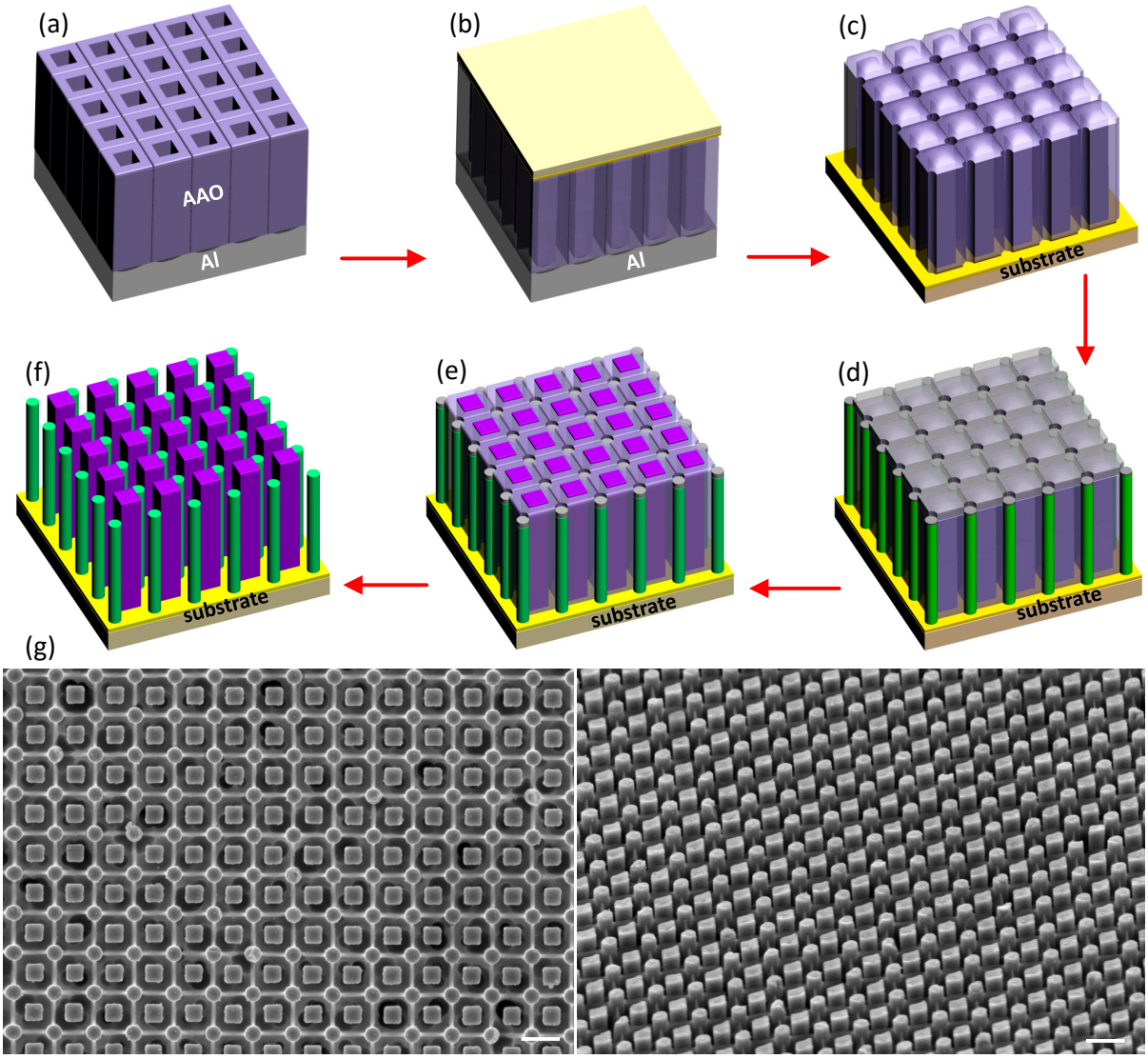

Figure 5-14. Schematic of fabricating binary nanowire/nanowire arrays: (a) template synthesizing and B-pores barrier layer removing; (b) deposition of supporting layer; (c) template reversing, unoxidized Al removing, and selective etching of B-pores; (d) electrodepositing round nanowires into B-pores and coating a top insulated layer; (e) removing insulated layer and A-pore barrier layer, electrodepositing square nanowires in A-pores; (f) dissolving template and insulated layer; (g) representative SEM images of the binary nanowire/nanowire arrays. Scale bar: 400 nm.

Moreover, the distribution profile of the Ni and Ag elements are revealed by EDX linear scanning, spectrum and mapping in Figure 5-15. From an EDX linear scanning along the green line inside the SEM image of Figure 5-15a, it is clearly that the periodical distributions of Ni (blue) and Ag (yellow) curves match with the round-shaped and square-shaped nanowires, respectively. Further information is confirmed by EDX mappings from the inset SEM image in Figure 5-15b, in which the spatial compositions of Ni (green) and Ag (red) dot array perfectly match with the binary nanowire/nanowire arrays.

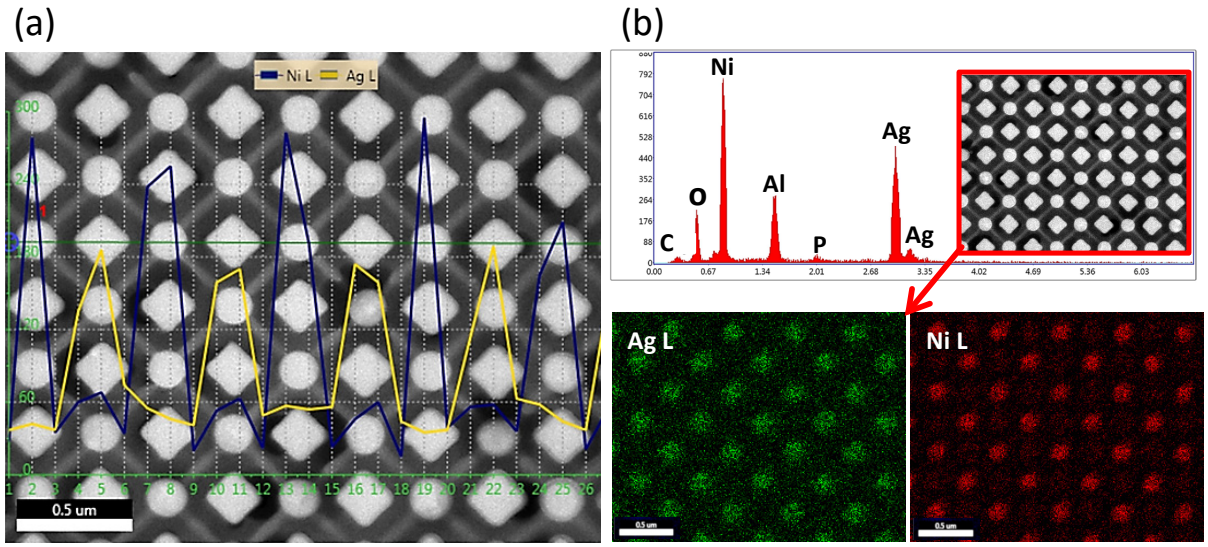

Figure 5-15. (a) SEM image of binary Ni/Ag nanowire/nanowire arrays and the periodical distribution profiles of Ni and Ag elements are revealed by EDX linear scanning along the green line inside the SEM image. (b) EDX spectrum from the inset SEM image. EDX mappings of spatial compositions of binary Ag (green)/Ni (red) dot arrays from the same inset SEM image are presented at the bottom, respectively.

5.3.2 Fabrication of binary nanowire/nanotube arrays

The preparation details of binary TiO_2/Cu_2O nanotube/nanowire arrays:

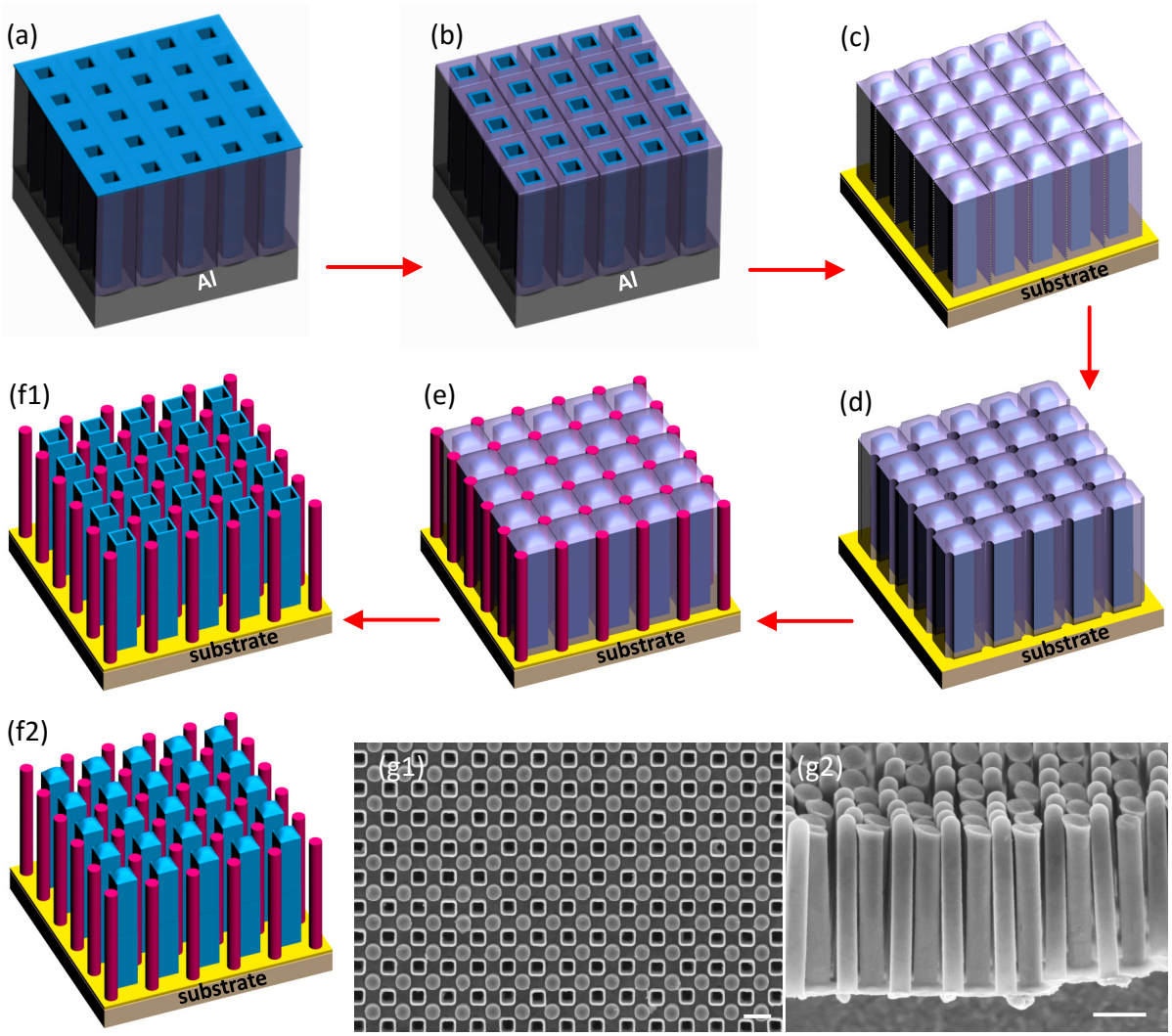

Figure 5-16. Schematic of fabricating binary nanotube/nanowire arrays: (a) ALD growth of square shape nanotubes in A-pores; (b) top surface ALD layer and B-pore barrier layer removing; (c) deposition of supporting layer, template reversing, unoxidized Al removing; (d) selective etching B-pores; (e) electrodepositing nanowires in B-pores; (f1) removing A-pore barrier layer, opening the tubes, and dissolving binary-pore template for opened-tubes; (f2) dissolving binary-pore template for close-end tubes; (g1) top-view SEM image of binary nanotube/nanowire arrays with open-end tubes; (g2) cross-sectional SEM image of binary nanotube/nanowire arrays with close-end tubes.

(1). Template is prepared as described above. TiO_2 nanotubes (with about 30 nm tube wall thickness) are grown in A-pores by ALD (600 cycles, 300°C) (Figure 5-16a).

(2). Remove B-pore barrier layer with ion milling (Figure 5-16b).

(3). Same as the Figure 5-14b, a Ni supporting layer is prepared, followed by Al removing (Figure 5-16c).

(4). Bottom side of the template is immersed in 0.1 M NaOH to generate B-pores (Figure 5-16d).

(5). Cu_2O nanowires are grown inside the B-pores with a cathodic current of 0.08 mA cm^{-2} for 1h (Figure 5-16e).

(6). Ion milling is used to remove the A-pore barrier layer and open the TiO_2 tubes. After dissolving the template, binary TiO_2/Cu_2O nanotube/nanowire arrays (with open-end tubes of TiO_2) are attained (Figure 5-16f1). By dissolving the template without ion milling, close-end TiO_2 tubes are achievable (Figure 5-16f2).

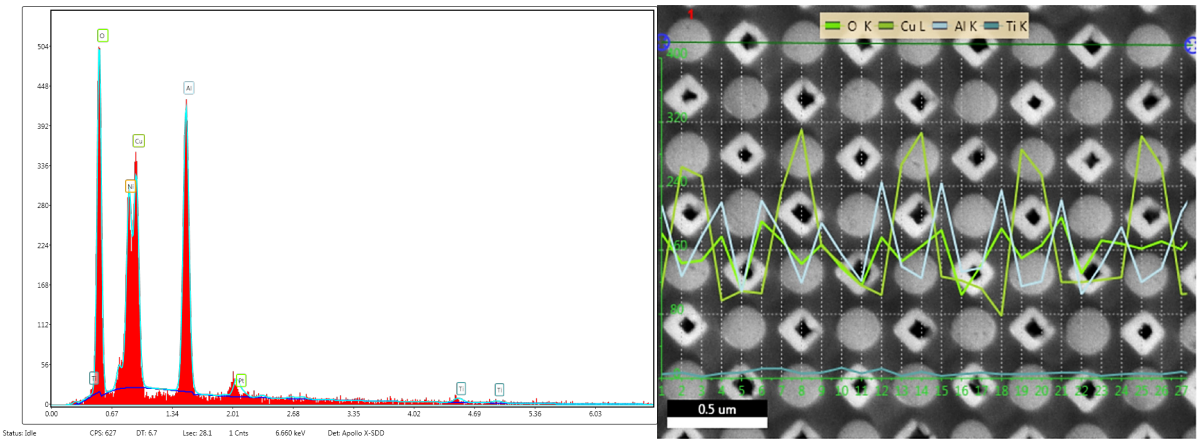

Figure 5-17. (a) EDX spectrum of the binary Cu_2O/TiO_2 nanowire/nanotube arrays. (b) EDX linear scanning across the dark green line inside the SEM image. The element profiles of Cu, O and Al are well match with the periodical distributions of TiO_2 and Cu_2O in the SEM image.

Moreover, the distribution profiles of the O, Cu, Al and Ti elements are revealed by EDX spectrum and linear scanning in Figure 5-17. From an EDX linear scanning along the green

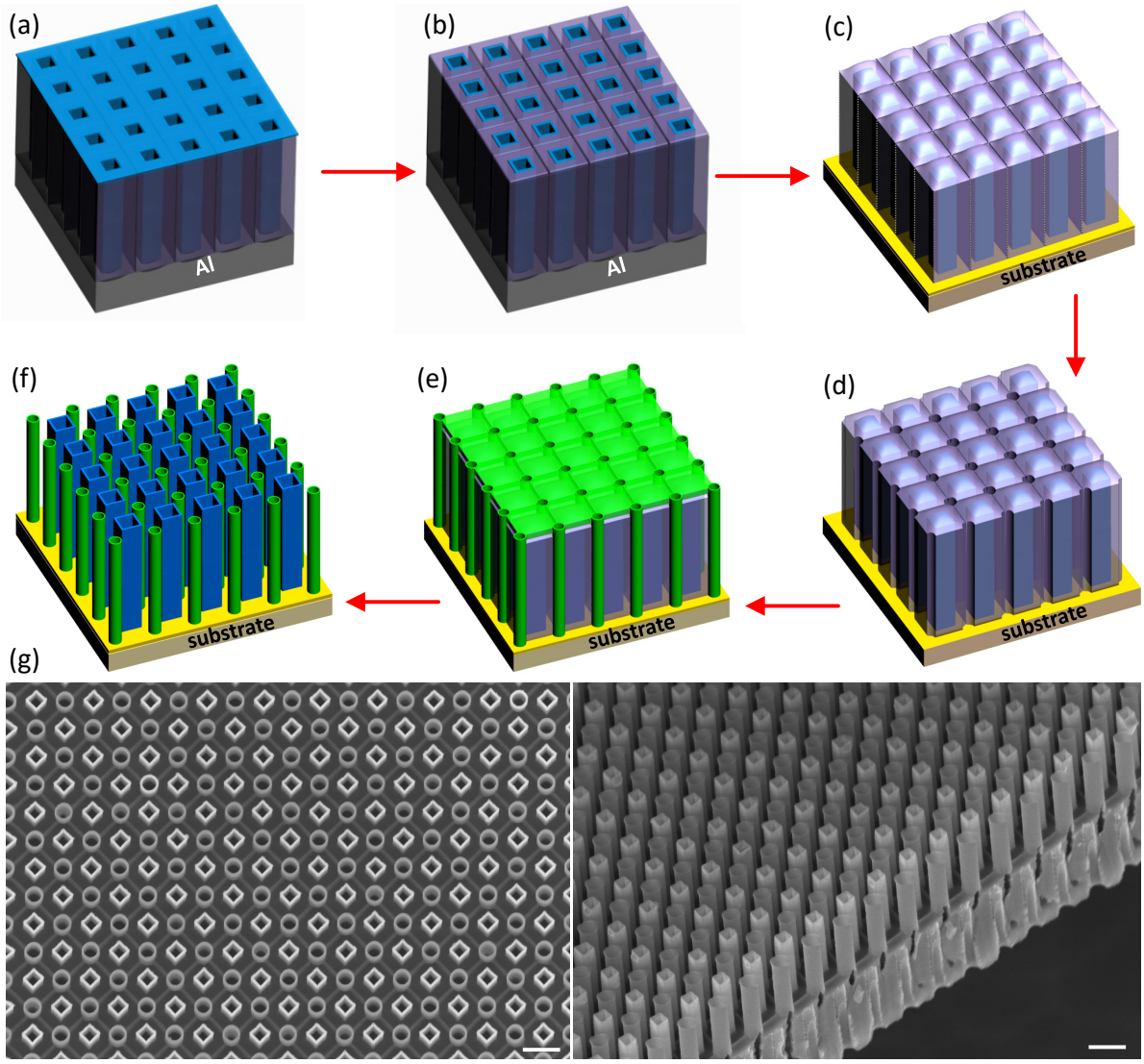

Figure 5-18. Schematic of fabricating binary nanotube/nanotube arrays: (a) ALD growth of nanotubes in A-pores; (b) top surface ALD layer and B-pore barrier layer removing; (c) deposition of supporting layer, template reversing, unoxidized Al removing; (d) selective etching of B-pores; (e) growth of nanotubes in B-pores; (f) etching away top ALD layer and A-pore barrier layer, dissolving binary-pore template; (g) representative SEM images of the binary nanotube/nanotube arrays. Scale bar: 400 nm.

line inside the SEM image of Figure 5-17b, it is clearly that the periodical distributions of O (light green), Cu (dark green), Al (light blue) and Ti (dark blue) curves match with the round-shaped Cu_2O nanowires and square-shaped TiO_2 nanotubes, respectively.

5.3.3 Fabrication of binary nanotube/nanotube arrays

The preparation details of binary TiO_2/SnO_2 nanotube/nanotube arrays:

(1) - (4). Growth of TiO_2 nanotubes is the same as that described in Figure 5-16a-d.

(5). A 30 nm SnO_2 layer is grown in the template with ALD (1000 cycles, 300 °C) (Figure 5-18e).

(6). Binary TiO_2/SnO_2 nanotube/nanotube arrays are obtained after removing the top surface SnO_2 layer and A-pore barrier layer with ion milling, and dissolving the template in 1.0 M NaOH solution (Figure 5-18f).

5.3.4 Fabrication of complex binary nanowire/core-shell nanowire arrays

Besides, a complex binary CdS/Ni-TiO_2 nanowire/core-shell nanowire arrays is also successfully obtained with the assistance of electrodeposition and ALD (Figure 5-19). The general process is the same as that described in Figure 5-16. Only two different steps are carried out in Figure 5-19c and 5-19e, respectively. Filling Ni nanowires into TiO_2 nanotubes is carried out with a 20 min pulsing deposition (80 mA for 50 ms – 1 mA for 450 ms) before the growth of thick Ni film (Figure 5-19c). Then, CdS nanowires are deposited in B-pores under a constant current (1.5 mA cm^{-2}) in DMSO solution consisted of 0.055 M $CdCl_2$ and 0.19 M element sulfur at 120°C (Figure 5-19e). A-pore barrier layer and TiO_2 nanotubes are opened with ion milling and the representative SEM images of the binary nanowire/core-shell nanowire arrays are shown in Figure 5-19g.

Moreover, the distribution of the CdS nanowires and Ni-TiO_2 core-shell nanowires are confirmed by the EDX linear scanning and mapping in Figure 5-20. From an EDX linear scanning along the green line inside the SEM image of Figure 5-20a, it is clearly that the periodical distributions of Ni (yellow) and Ti (blue) curves match with the square-shaped nanowires, and S (purple) and Cd (grey) curves match with the round-shaped nanowires, respectively. Furthermore, from the EDX mappings in Figure 5-20b, the spatial compositions

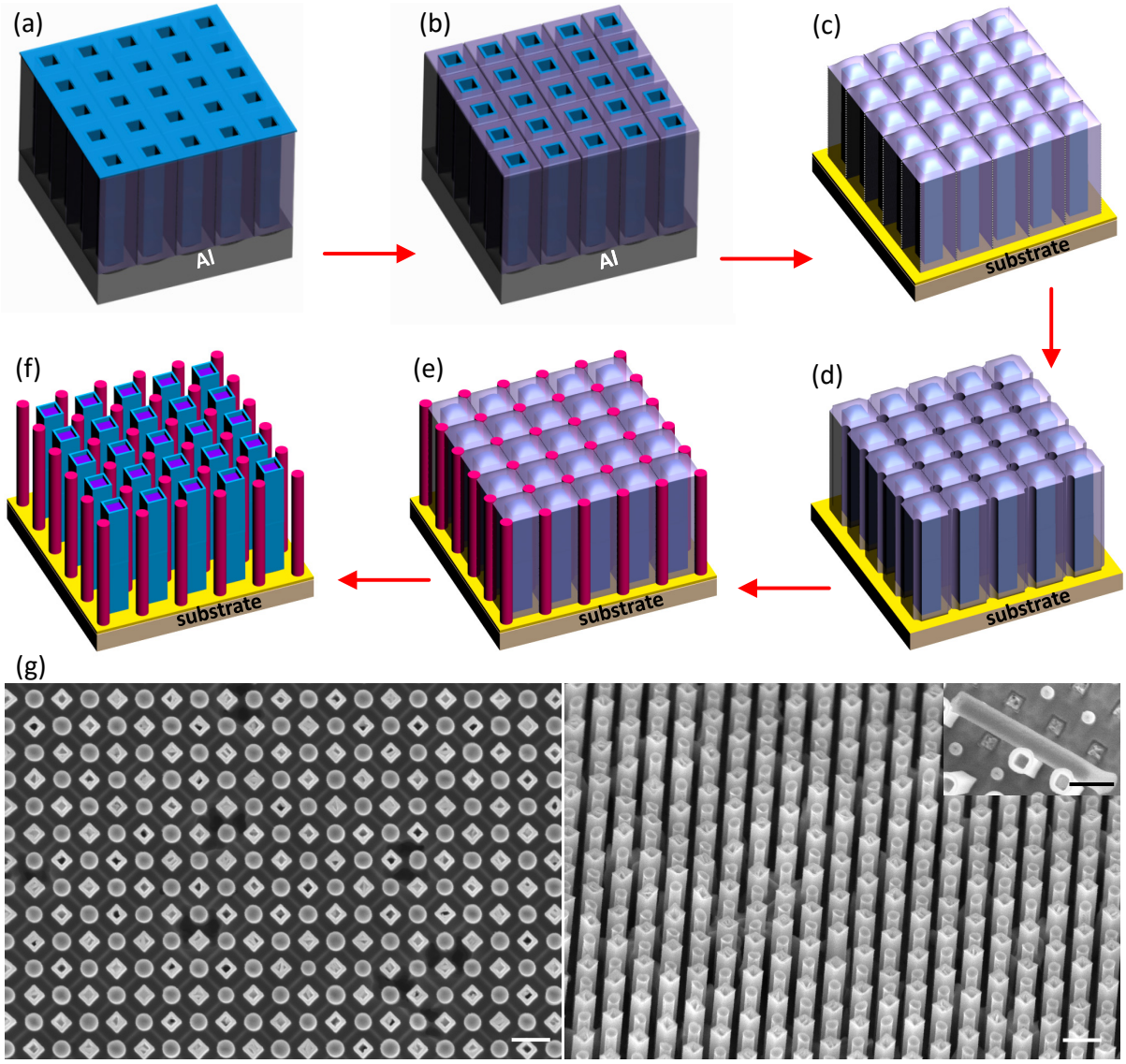

Figure 5-19. (a-f) Schematic of fabricating complex binary CdS/Ni-TiO_2 nanowire/core-shell nanowire arrays. (g) Representative SEM images of the binary CdS/Ni-TiO_2 nanowire/core-shell nanowire arrays. The inset SEM shows the Ni filled TiO_2 nanotube. Scale bar: 400 nm.

of Cd and S elements overlap each other to match with the round-shaped CdS nanowires, and the Ni and Ti elements overlap each other to match with the square-shaped Ni-TiO_2 core-shell nanowires, respectively.

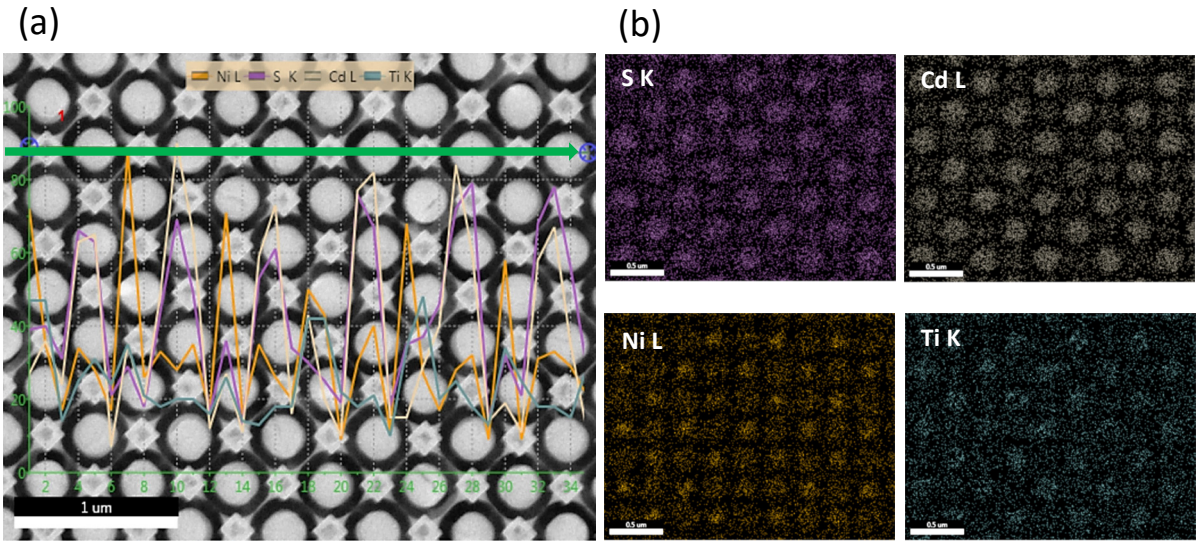

Figure 5-20. (a) EDX linear scanning across the green line inside the SEM image. The distribution profiles of S, Cd, Ni and Ti elements match with the round-shaped CdS nanowires and square-shaped Ni-TiO_2 core-shell nanowires, respectively. (b) EDX mappings from the same SEM image, in which the overlap of purple and yellow dot arrays present the spatial distribution of round-shaped CdS nanowires, and the overlap of orange and cyan dot arrays present the spatial distributions of square-shaped Ni-TiO_2 core-shell nanowires, respectively.

5.3.5 Fabrication of binary nanodot/nanodot arrays

Meanwhile, taking the advantages of ultra-thin alumina mask (UTAM) technique, binary Au/Ag nanodot/nanodot array is also been synthesized with two-step PVD (Figure 5-21).

The preparation details of binary Au/Ag nanodot/nanodot arrays:

(1). An ultra-thin template is prepared with a short time anodization (typically 6 min). After removing the B-pore barrier layer with ion milling, a PMMA layer is coated on the top side of the ultra-thin template as a protection layer for dissolving the backside Al and selective etching of B-pores in 0.1 M NaOH solution (40 min). PMMA is then removed in acetone before mounting the template on substrate (Figure 5-21a).

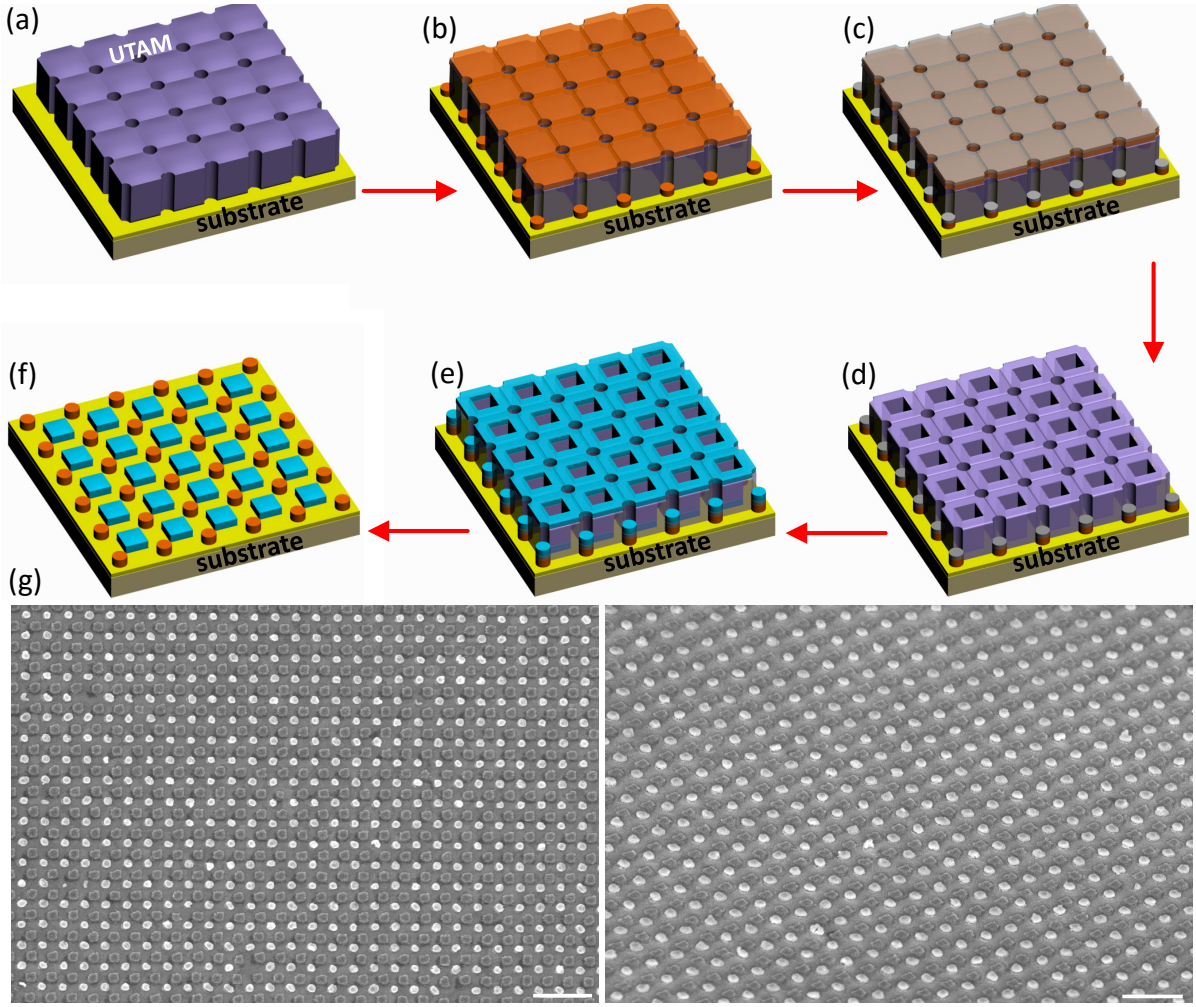

Figure 5-21. Schematic of fabricating binary nanodot/nanodot arrays: (a) removing B-pore barrier layer, selective etching B-pores and mounting ultra-thin template on substrate; (b) evaporating first nanodot array; (c) evaporating sacrificial layer; (d) ion milling for etching away sacrificial layer and A-pore barrier layer on template; (e) evaporating the second nanodot array; (f) removing the ultra-thin template and etching sacrificial layer. (g) Representative SEM images of the binary CdS/Ni-TiO_2 nanowire/core-shell nanowire arrays. Scale bar: 1 µm.

(2). After the first-step of PVD evaporation through B-pores, round-shaped Au nanodot array is attained on substrate and also forms an Au evaporated layer on the surface of template (Figure 5-20b).

(3). Later a sacrificial layer (Zn) is evaporated on top of round-shaped Au nanodot array and on the template surface as well (Figure 5-21c).

(4). The sacrificial Zn layer and the underneath Au evaporated layer, as well as the A-pore barrier layer are removed by ion milling (Figure 5-21d).

(5). A second step of PVD process is carried out through A-pores, resulting in a square-shaped Ag nanodot array (Figure 5-21e).

(6). After removing template with scotch tape and etching away the Zn sacrificial layer with 0.1 M NaOH solution, a binary Au/Ag nanodot/nanodot array could be realized (Figure 5-21f).

5.4 Evolution of binary-pore template

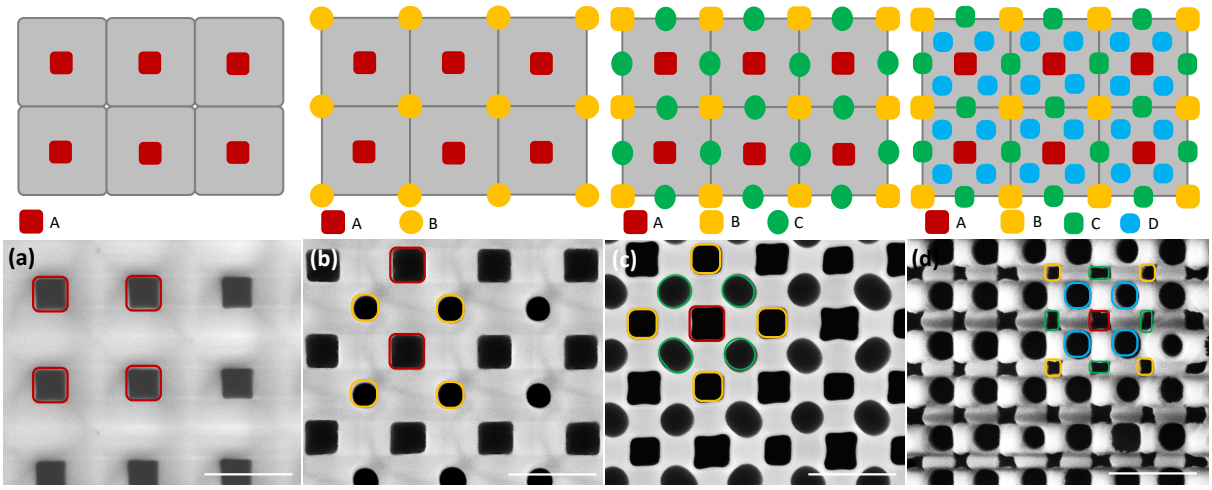

Figure 5-22. Schematics and representative SEM images of the template evolution: (a) single-pore array; (b) binary-pore array; (c) ternary-pore array; (d) quadruple-pore array. Scale bar: 400 nm.

Inspired by the binary-pore template, the evolution of the template from a single-pore array to a quadruple-pore array could be realized, in which not only the nearest interpore distance can be greatly reduced from 400 nm to 140 nm, but also the obtained four sub-pore arrays present even more morphologic options and higher pore densities. The schematics and the

representative SEM images are summarized in Figure 5-22, in which the red, yellow, green, and blue rings indicate the A-, B-, C-, and D-pores, respectively.

The key steps for realizing such structure are shown in follows. The ultra-thin binary-pore template on silicon substrate is prepared with the same procedure as that described in Figure 5-23 (1). Then, a reactive ion etching (RIE) is used to obtain 150 nm depth binary-shallow arrays on silicon substrate, in which the ultra-thin binary-pore template acts as a shade mask (Figure 5-23a). The silicon substrate with binary-shallow array is used as a master mold for obtaining Ni imprinting mold and the subsequent Al foil with binary-concave array (Figure 5-23b). The synthesizing process is as the same as that described in imprinted template preparation part. Since the nearest interpore distance is decreased to about 283 nm, so the Al foil anodization is carried out under 113 V in 0.4 M H_3PO_4 for 10 min, where the anodization voltage is chosen to satisfy the linear relationship between the interpore distance and the anodization potential (2.5 nm V^{-1}). The imprinted square- and round-shaped concave arrays then turn out to be two different sizes of square-shaped pores, and both of the pores are grown vertically to the Al foil (Figure 5-23c). The unoxidized Al is removed in the mixed solution of $CuCl_2$ and HCl, which results in two different sizes of barrier layers (Figure 5-23d). The second selective etching is conducted in 0.1 M NaOH solution for 40 min and a new elliptical-shaped pore array (denoted as 'C-pores',) is generated at the junction sites of A- and B-pores (Figure 5-23e). Ternary-pore array is then obtained after using ion milling to completely remove the barrier of A- and B-pores (Figure 5-23f). The ternary-shallow array is transferred to silicon substrate with the assistance of RIE etching, and the process is as the same as that of (a), which decreases the nearest interpore distance to about 195 nm (Figure 5-23g). After transferring the ternary-concave array to Al foil, the ternary-pore template is attained from the anodization at 78 V in 0.4 M H_3PO_4 for 10 min. The two square-shaped and one elliptical-shaped pore arrays in (g) then turn out to be two square-shaped and one

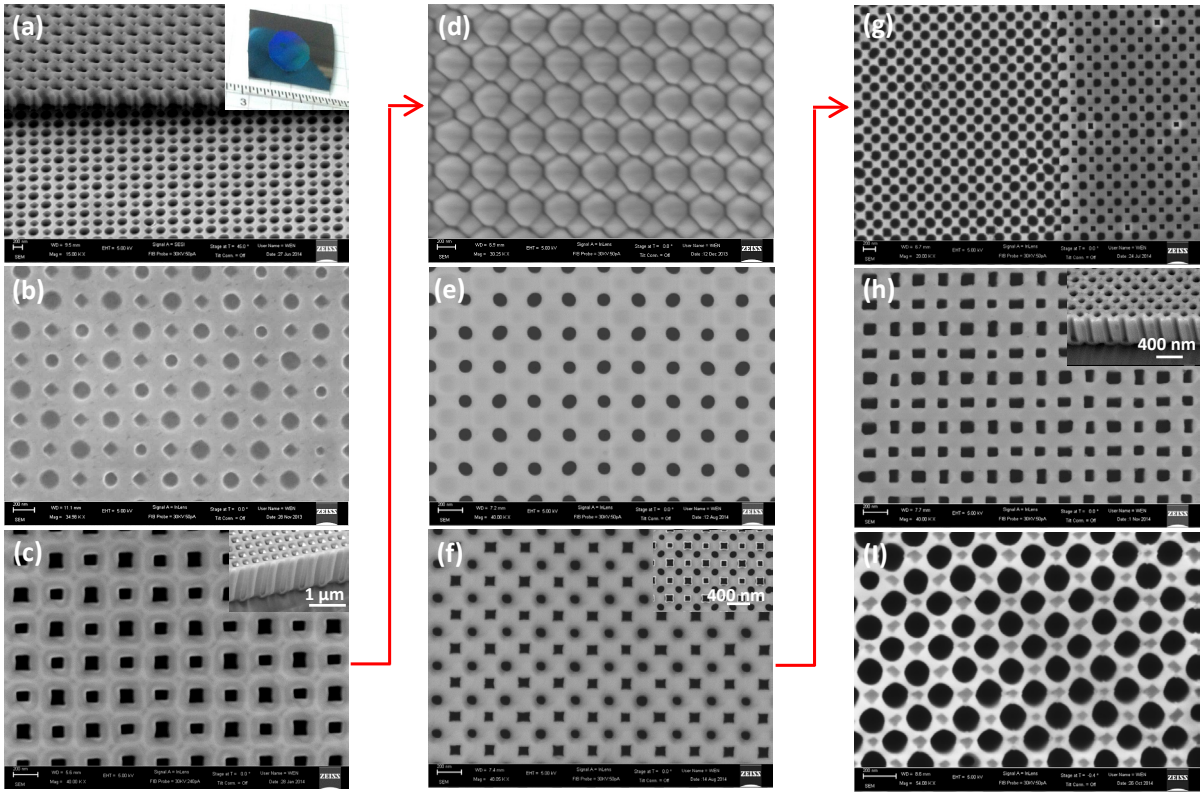

Figure 5-23. SEM images of key steps for realizing a quadruple-pore array: (a) preparation of a binary-shallow array on silicon substrate with RIE; (b) formation of a binary concave array on Al foil with imprinting process; (c) Obtaining a binary-pore array with anodization; (d) removal of unoxidized Al foil; (e) generating C-pores with the 2nd selective etching; (f) attaining a ternary-pore array with ion milling; (g) preparation of a ternary-shallow array on silicon substrate with RIE; (h) anodizing for realizing a ternary-pore array; (i) achieving D-pores with the 3rd selective etching.

rectangle-shaped pore arrays and all of them are grown vertically to the Al foil (Figure 5-23h). Third selective etching is conducted in 0.1 M NaOH solution for 40 min and a round-shaped pore array (denoted as 'D-pores') is generated at each junction sites of A-, B- and C-pores (Figure 5-23i).

Considering the above results, we prove that multi-pore array in one matrix can be successfully attained with our innovative selective etching in NaOH solution. The profile of the template can be precisely tailored, including the pore size, shape and density, which

provides significant superiors and flexibilities for realizing novel architectures based on template that might be very difficult, if not impossible to make with other top-down and bottom-up techniques.

5.5 Performance of binary devices

5.5.1 'Z-scheme photosynthesis cell' based on binary nanostructure arrays

When both sub-arrays are used as the functional-functional units, an artificial nano-photosynthesis for solar energy conversion is proposed here. In natural photosynthesis, photochemical reactions are separated in chloroplast. The electrons used to produce NADPH are excited *via* the absorbed light with 'Z-scheme' in photosystems I and II. The same concept can be applied in artificial photosynthesis with an integrated system consist of inorganic materials.[186-188] So far, most studies of 'Z-scheme' for solar energy conversion employed either electrode-based macroscopic devices or a mixture of two semiconductor powders. Yet, there are no commercial products based on artificial photosynthesis so far, due to the extremely high cost of the existing photoelectrochemical reaction systems.

Our goal here is to find an efficient and inexpensive way to manufacture stable nanostructures for constructing wireless photoelectrochemical units on large scale for solar energy conversion. For this purpose, binary (n-type TiO_2/p-type Cu_2O) nanostructure arrays are synthesized as a nanoscale 'Z-scheme' unit (Figure 5-24a). The unit takes advantages of large surface area, short carrier travel distance, high density, and short ion diffusion distance between each sub-unit sustaining a stable neutral environment. Upon illumination, photoexcited electron-hole pairs are generated in Cu_2O and TiO_2. Due to the band-bending at the semiconductor-electrolyte interfaces, the photogenerated holes in the TiO_2 nanowire and the electrons in the Cu_2O nanowire will migrate to the surfaces for oxidizing water to O_2 and

reducing protons to H_2, respectively. The electrons from TiO_2 nanotube and the holes from Cu_2O nanowire will recombine at the common metal substrate. This process completes the

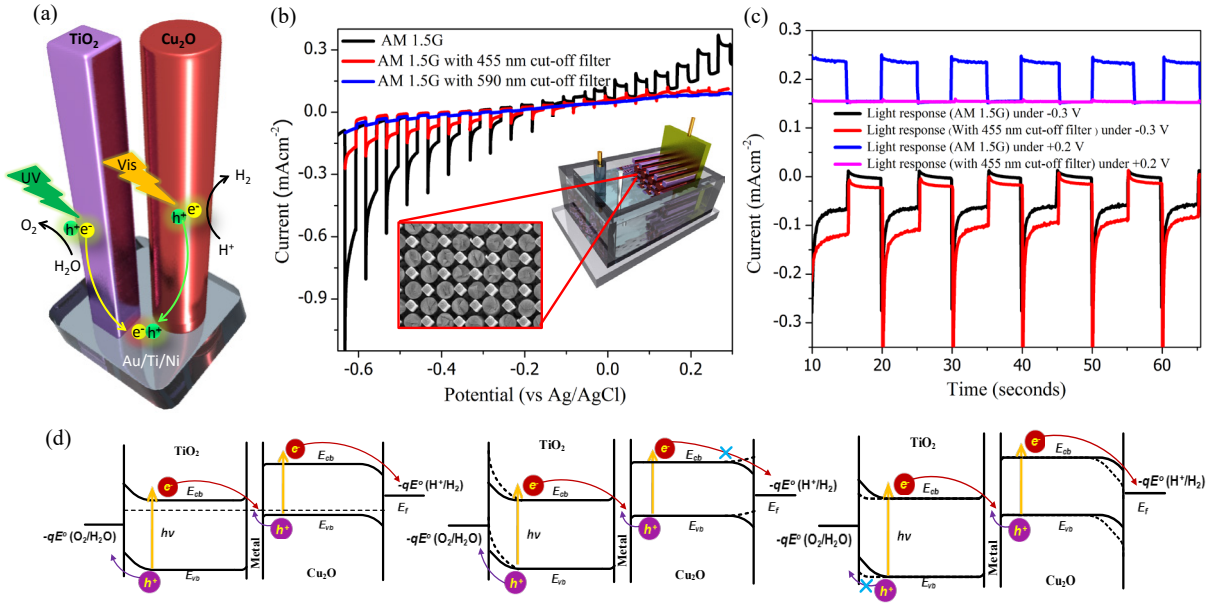

Figure 5-24. (a) Illustration of a 'Z-scheme' unit based on binary TiO_2 (n-type)/Cu_2O (p-type) nanostructure arrays (binary-electrode). (b) Current vs potential curves of the binary-electrode under AM 1.5G, AM 1.5G with 455 nm cut-off filter and AM 1.5G with 590 nm cut-off filter, respectively. Sweep rate is 5 mV s^{-1} and sweep direction is from -0.7 V to 0.3 V. (c) Selective light response of the binary-electrode under -0.3 V (negative bias) without/with 455 nm cut-off filter and under 0.2 V (positive bias) without/with 455 nm cut-off filter, respectively. (d) Energy band diagrams of the binary-electrode under non bias, positive, and negative bias conditions.

relay of the 'Z-scheme', which successfully mimics the function of natural photosynthesis (Figure 5-24a). The chopped I-V photocurrents of the binary-electrode under simulated sunlight are plotted in Figure 5-24b. Illuminating with AM 1.5G and sweeping the bias from -0.7 V to 0.3 V, the binary-electrode shows obvious anodic and cathodic photocurrents simultaneously, in which the anodic part is ascribed to the n-type TiO_2 nanotubes and the cathodic part is originated from the p-type Cu_2O nanowires (dark curve in Figure 5-24b). When a 455 nm cut-off filter is used, the photocurrent from the anodic part becomes

negligible because of the large band band gap of TiO_2 (3.2 eV). While, the photocurrent from the cathodic part still can be observed, though it decreases to about 35% of the original value (red curve in Figure 5-24b). Furthermore, owning to the band gap of Cu_2O (2.1 eV), no photocurrent is observed from the cathodic part when a 590 nm cut-off filter is used (blue curve in Figure 5-24b).

Meanwhile, a multiple photodetector is also proposed based on the binary-electrode in Figure 5-24c, under AM 1.5G illuminating, when a -0.3 V (negative bias) is applied, light response from the Cu_2O nanowires is observed and the response keeps well with a 455 nm cut-off filter. On the other hand, when a 0.2 V (positive bias) is applied, light response from the TiO_2 nanotubes is observed, but the light response completely vanishes with a 455 nm cut-off filter. Therefore, the light response of the photodetector can be tuned by not only the bias (-0.3 V or 0.2 V) but also the light wavelength (with or without 450 nm cut-off filter) as well. Those results can also be confirmed with the energy band diagram in Figure 5-24d, the band bending between the binary-electrode and the electrolyte will upward with a positive bias, which promotes the transfer of holes from the TiO_2 nanotubes to the electrolyte interface, but depresses or even blocks the transfer of electrons from the CuO_2 nanowires to the electrolyte interface. On the other hand, when a negative bias is applied, the condition between the binary-electrode and the electrolyte will be reversed. Moreover, each sub-component array can be future tailored or optimized at the relevant steps for improving the performance accordingly. As a comparison, single round-shaped Cu_2O nanowire array and single square-shaped TiO_2 nanotube array are prepared, in which only cathodic photocurrent is generates from the Cu_2O nanowires and only anodic photocurrent is observed from the TiO_2 nanotubes (Figure 5-25).

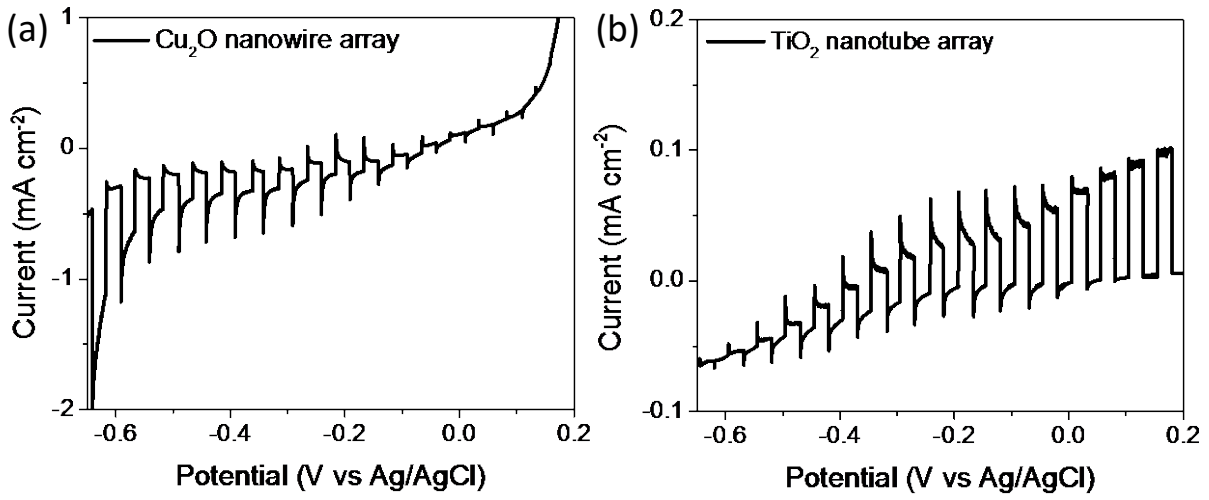

Figure 5-25. Current vs potential curves of single 'array's: (a) round-shaped Cu_2O nanowire array; (b) square-shaped TiO_2 nanotube array.

5.5.2 Addressable multi-gate nanowire transistor based on binary nanostructure arrays

So far IC technology in the microelectronic industry almost reaches the lithographic limit. Extreme ultraviolet, e-beam, nanoimprint and other lithographic technologies have been developed to replace conventional optical lithography. Due to the physical limits of semiconductors, the effort to scaling-down devices faced other challenges, such as high off-state leakage current and short-channel effect. Alternatively, scientists are exploring the third dimension for 3D integration of chips. Semiconductor nanowires are the ideal candidate for integration.[3, 189-192] However, current integration of nanowires on large-scale only depends on complicated multi-step patterning, deposition, etching and polishing. Furthermore, realization of nanowire devices is still a hard task because current technologies are very difficult to control the stacking of channel, dielectric and gate layer in vertical. Therefore, an addressable multi-gates nanowire transistor is proposed based on binary nanostructure arrays, which is expected to solve the above problems.

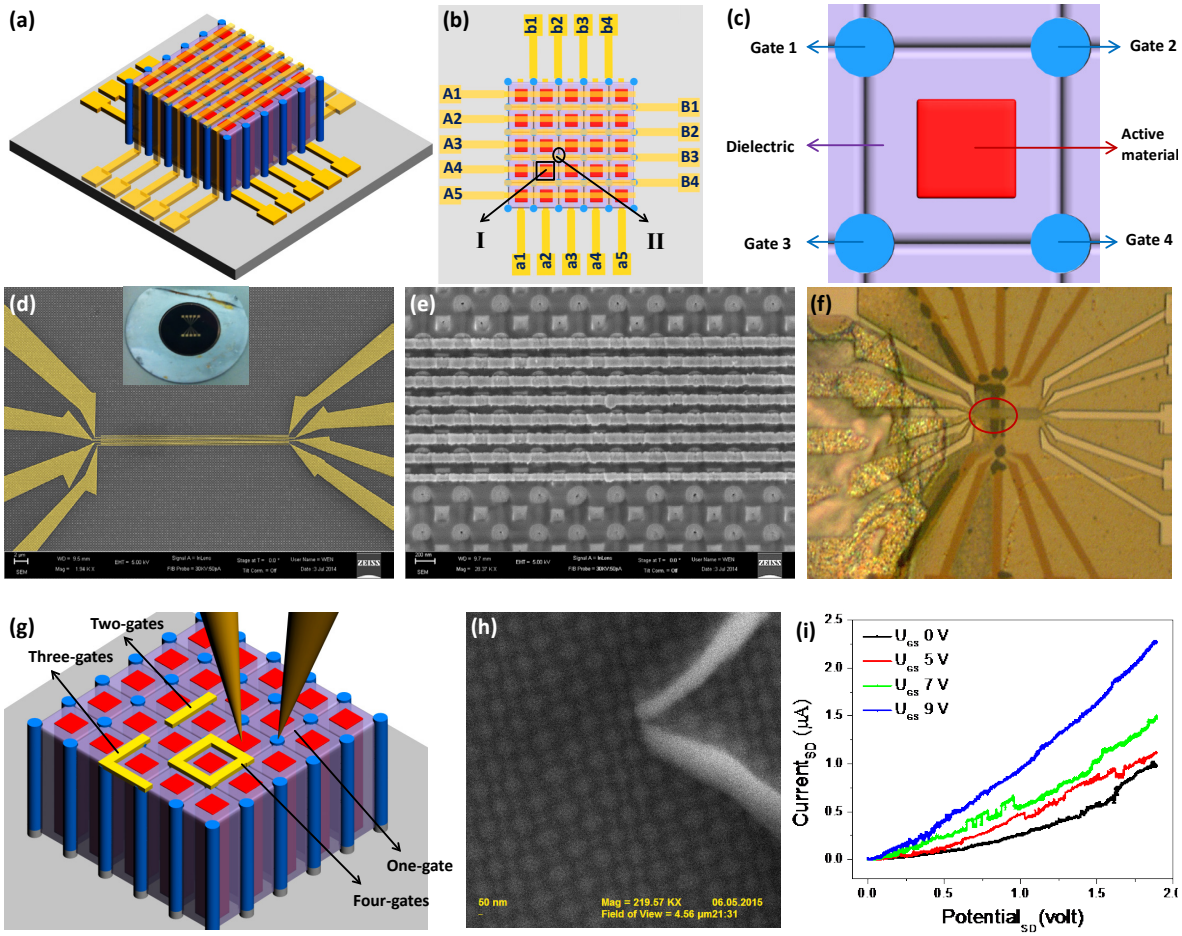

Figure 5-26. (a-c) Schematic of an addressable multi-gates nanowire transistor based on binary AZO/ZnO nanostructure arrays. (d-f) Fabrication of crossbar electrode lines to match with the top ends of the ZnO and AZO nanowires on both sides of the template, respectively. (g-h) MTSTM set up for a single ZnO nanowire investigation. (i) Transfer characteristics of a single ZnO nanowire when applying the gate bias on an adjacent AZO nanowire.

As shown in Figure 5-26a and b of this transistor, the square-shaped nanowires are controlled through Ax (x=1-5) with ax (x=1-5) electrodes, while the round-shaped nanowires are addressed by Bx (x=1-5) with bx (x=1-5) electrodes. For instance, the square-shaped nanowire (I) could be controlled by A4−a2 electrodes, and the round-shaped nanowire (II) is guided by B3−b2 electrodes (Figure 5-26b). The core concept of the multi-gates transistor is that the semiconductor in the square-shaped pores could conduct as a functional unit, the

conductive material in the surrounded four round-shaped pores could run as controlling gates, and the insulate AAO template could act as a native dielectric layer (Figure 5-26c). During the transistor operation, the four gates can work as either a single-gate or multi-gate (two-, three- or four-) with a designable purpose. Such as, when ZnO nanowire (I) in Figure 5-26b is defined as the functional unit and being manipulated by A4−a2 electrodes, the surrounded AZO four-gates of this wire (I) are controlled by B3−b1, B3−b2, B4−b1, and B4−b2 electrodes individually or simultaneously. Overall, addressable multi-gates nanowire transistor is highly feasible and each parameter of the functional and controlling unit (such as the size and morphology of semiconductor channel and gate, as well as the thickness of the dielectric layer) can be precisely adjusted depending on requirement.

After that, a standard EBL process is conducted to fabricate electrode lines on one side of the template to match with the top end of the ZnO and AZO wires, respectively (Figure 5-26d and e). Then, a same EBL process is carried out again to fabricate electrode lines on the other side of template, which results in crossbar electrode lines at the both top end of ZnO and AZO wires (Figure 5-26f).

Meanwhile, in order to evaluate the transistor performance easily, multi-tip scanning tunneling microscopy (MTSTM, from Prof. Thomas Hannappel group), a powerful tool for electrical transport measurements at nano-scale, is used to investigate a single ZnO nanowire performance before the device assembling (Figure 5-26g and h). The typical transfer characteristics of a single ZnO nanowire are plotted in Figure 5-26i. From the results, we can see that the ZnO current$_{SD}$ is largely increased by applying a bias on an adjacent AZO gate from 0 V to 9 V gradually. Therefore, it confirms the possibility of realizing multi-gates nanowire transistor based on binary nanostructure arrays. The performance of the transistor could be optimized by adjusting the thickness of dielectric layer, the growth conditions of ZnO and AZO, or replacing with other more suitable materials (e.g, Si, InP) in the further.

5.6 Construction of Pt/MnO_2 core/shell nanotube array for supercapacitor

5.6.1 Background

Among pseudocapacitors, ruthenium oxide (RuO_2)-based devices have shown the highest specific capacitance of 1580 Fg^{-1} (at 1 mV s^{-1}).[193-196] However, its toxicity and high cost make RuO_2 less attractive for practical applications. Among other low-cost alternatives, MnO_2 has stood out as the most promising material due to many remarkable features such as environmental friendliness, low cost, and high theoretical specific capacitance.[197-204] However, it is highly challenging to reach this value due to the low electrical conductivity of MnO_2 ($\sim 10^{-5} - 10^{-6}$ S cm^{-1}). To improve the electrical conductivity and boost the performance of pseudocapacitors, Simon and Gogotsi proposed the development of binder-free electrodes in which pseudo-capacitive materials would be conformally deposited onto highly conductive and well-ordered nanostructured electrodes.[205]

5.6.2 Preparation of Pt/MnO_2 core/shell nanotube arrays

Herein, Pt/MnO_2 core/shell electrode is exploited to address this issue, and the fabrication process is shown in Figure 5-27. In this process, a Pt nanotube array (NTs) is grown on an imprinted template firstly (Figure 5-27a to d). After that, a mixed polydimethylsiloxane (PDMS) solution is poured on the surface of the template, followed by dissolving the backside template (Figures 5-27e and f). Finally, a thin MnO_2 layer is deposited on the Pt NTs, resulting in a supercapacitor electrode based on core/shell Pt/MnO_2 NT array (Figure 5-27g). For this core/shell structure, the core Pt NT with high electrical conductivity is used as a current collector to provide paths for charge storage and delivery. Meanwhile, the construction of the NTs can also offer a large surface area to increase the active material (*i.e.*, MnO_2) mass loading.

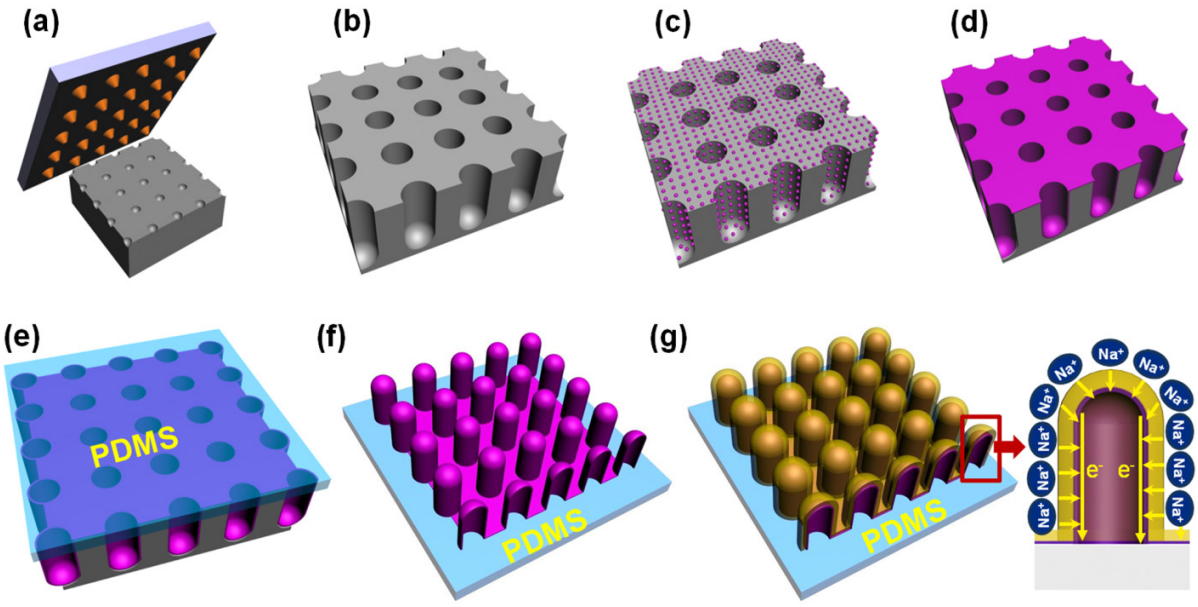

Figure 5-27. Schematic illustration of the fabrication process for Pt/MnO_2 core/shell electrode: (a) surface imprinting on an aluminium foil to form concave array; (b) anodization for preparing template followed by a chemical etching process; (c) dispersed Pt nanoparticles formed on template after a few ALD growth cycles; (d) continuous Pt NT array obtained after more ALD growth cycles; (e) a mixed PDMS solution poured on template; (f) removing template and resulting in a Pt NT array on PDMS substrate; (g) electrodepositing MnO_2 to form Pt/MnO_2 NT array for supercapacitor electrode.

Pt NTs with about 180 nm tube diameter and 2 µm length (Figure 5-28a) are used for growing core/shell Pt/MnO_2 NTs for supercapacitor applications. MnO_2 shells are electrodeposited on Pt cores. The overall core-shell NT diameter (and hence the thickness of MnO_2 shell) can be adjusted by controlling the MnO_2 deposition time: the tube diameter and the shell thickness is about 240 and 30 nm when the deposition time is 30s (Figure 5-28b), while the diameter and thickness reach up to about 340 and 80 nm respectively for 90s deposition time (Figure 5-28c). These pre-defined core-shell Pt/MnO_2 NT arrays are used to construct supercapacitor electrodes (photography of a typical electrode is shown in Figure 5-28d). The mass of the

MnO_2 is determined from the charge passed during electrochemical deposition and assumes 100% efficiency. The calculated mass of MnO_2 is ~ 0.094 mg/cm^2 and ~ 0.216 mg/cm^2 for 30 s and 90 s MnO_2 deposition electrodes, respectively.

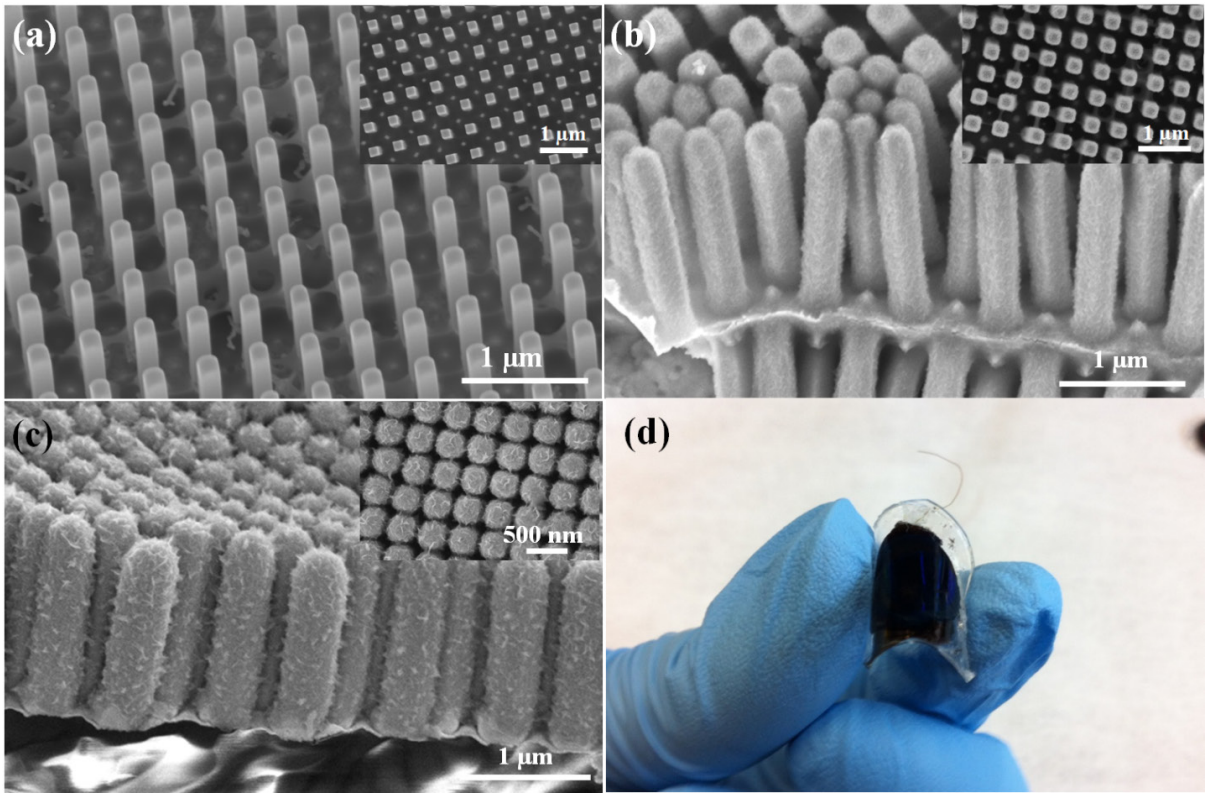

Figure 5-28. Tilted and top SEM images of (a) Pt NT array, (b) MnO_2 shell on Pt NTs after 30s deposition, (c) MnO_2 shell on Pt NTs after 90s deposition. (d) Photograph of a supercapacitor electrode on PDMS substrate using core/shell Pt/MnO_2 NT array.

5.6.3 Optimization of Pt/MnO_2 core/shell electrodes for supercapacitor

In order to study the performance of the core/shell Pt/MnO_2 NT arrays for electrochemical energy storage, cyclic voltammetry (CV) and galvanostatic charge-discharge are measured in a voltage window of 0-0.9 V. The CV tests are performed on four samples at a scan rate of 20 mV/s in 1.0 M Na_2SO_4: bare Pt NT array, 30s deposition Pt/MnO_2 NT array (denoted as 30s-NT electrode), 90 s deposition Pt/MnO_2 NTs array (denoted as 90s-NT electrode), MnO_2 on a Pt planar film (denoted as PF electrode) with same mass loading of the 30s-NT sample

(Figure 5-29a). The enclosed areas of the CV curves become much larger after MnO_2 loading, which reveals that the Pt electrode contribution to the capacitance can be ignored. The CV curves of the 30s-NT and 90s-NT electrodes have a clear quasi-rectangular shape, indicating their ideal electrical double-layer capacitance behaviours. On the contrary, the CV curve of the PF electrode is much worse compared to the NT electrodes. Meanwhile, the rate-dependent CVs of the typical 30s-NT electrode are investigated from 5 to 100 mVs^{-1} (Figure 5-29b). All the curves maintain a nearly ideal capacitive CV shape with only small distortions, showing remarkable rate capabilities of the electrode.

After that, the gravimetric specific capacitance (C_{sp}) vs the scan rate is summarized in Figure 5-29c. The C_{sp} of Pt/MnO_2 NTs electrode is calculated from cyclic voltammograms (CV) in 1.0 M Na_2SO_4 using equation (5-1):

$$C_{sp} = \frac{Q}{\Delta V * m} \tag{5-1}$$

Where C_{sp} is specific capacitance, Q is the total charge integrated from the CVs, ΔV is the width of potential window 0.9 V, and m is the mass of deposited MnO_2.

The specific capacitance, energy density (d_e), and power density (d_p) are also calculated from the chronopotentiometric curves according to equations (5-2 to 5-4):

$$C_{sp} = \frac{I\Delta t}{m\Delta V} \tag{5-2}$$

$$d_e = \frac{1}{2} C_{sp} (\Delta \mathrm{V})^2 \tag{5-3}$$

$$d_p = \frac{d_e}{\Delta t} \tag{5-4}$$

Where the I is the charge/discharge current, Δt is the time for a full charge or discharge, m is the mass of the active MnO_2 electrodes, and ΔV is the voltage change after a full charge or discharge.

And the areal specific capacitance (Casp) can be calculated as eq 5-5:

$$C_{asp} = \frac{Q}{\Delta V * a} or \frac{I\Delta t}{a\Delta V} \tag{5-5}$$

Where the *a* is the area of the MnO_2 active electrodes (about 0.50 cm^2) and the other values are the same as before described.

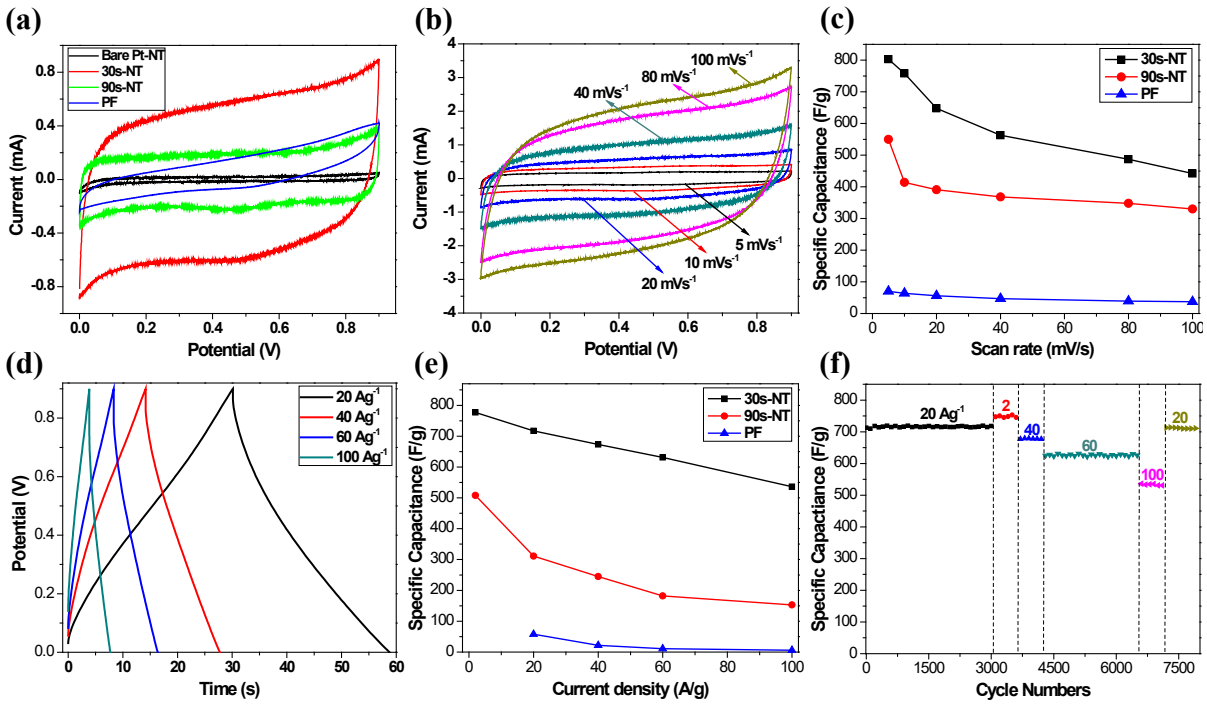

Figure 5-29. (a) The CVs of bare Pt-NT, 30s-NT, 90s-NT and PF electrode at a scan rate of 20 mVs^{-1}. (b) Typical CVs of the 30s-NT electrode at different scan rates from 5 to 100 mVs^{-1}. (c) Specific capacitance curves of the 30s-NT, 90s-NT and PF electrodes at the different scan rates. (d) Representative linear voltage-time profiles for the charging and discharging of the 30s-NT electrode at high current densities from 20 to 100 Ag^{-1}. (e) The summary plot of Csp versus current density of the 30s-NT, 90s-NT and PF electrodes. (f) Cycling stability of the 30s-NT electrode at random current densities up to 8000 cycles.

The calculations demonstrate that the capacitance of the 30s-NT electrode reaches to 810 Fg^{-1} at the scan rate of 5 mVs^{-1} (Eq 5-1). Meanwhile, the areal specific capacitance (Casp) also reaches up to 75 $mFcm^{-2}$ (Eq 5-5). Even when the deposition time increases to 90s, the electrode C_{sp} still keeps at 550 Fg^{-1} (119 $mFcm^{-2}$). The C_{sp} of the 30s- and 90s-NT electrodes yield much better performance at all scan rates compared with the PF electrode. For the 30s-NT electrode, the typical one-cycle charging-discharging behaviour from the current density of 20 to 100 Ag^{-1} show high symmetric natures in all current densities (Figure 5-29d). The

summary plot of C_{sp} versus current density demonstrates that the 30s-NT electrode reaches up to 793 Fg^{-1} (73 $mFcm^{-2}$) at 2 Ag^{-1} and this value is still at 530 Fg^{-1} (114 $mFcm^{-2}$) when the deposition time is increased to 90s (Figure 5-29e). And both the NT-electrodes have a much better performance than that of the PF electrode in all current densities. Most importantly, when the current density of the 30s-NT electrode increases to 100 Ag^{-1}, the C_{sp} still keeps at 542 Fg^{-1} (50 $mFcm^{-2}$), which retains at about 68 % capacitance of the C_{sp} at 2 Ag^{-1}. For most of the previously reported core/shell and hybrid nanostructures (*e.g.*, Au/MnO_2 nanopores,[206] Au/MnO_2 nanowires[207] and AuPd/MnO_2 nanorods[208]), the C_{sp} are very high at low current densities while it decreases dramatically at high current densities. The good rate capability of the Pt/MnO_2 NT arrays electrodes can be attributed to the superior Pt NT collector, which provides not only a highly accessible surface area but also appropriate gaps among the adjacent NTs for fast and reversible Faradic reactions and short ion diffusion paths. The long-term cycle stability of the 30s-NT electrode is also evaluated. The C_{sp} as a function of cycle number is presented in Figure 5-29f, where a negligible C_{sp} loss at 20 Ag^{-1} is observed over the first 3000 cycles. After that, random charging and discharging with current densities from 2 to 100 Ag^{-1} is carried out up to 8000 cycles and the electrode still presents a high cycle stability and a negligible capacitance loss after such a sudden variation.

Moreover, the morphology and the elements of the electrode after the cycling test are investigated by EDX mapping over a 20 μm × 20 μm area and by EDX line-scanning across a single Pt/MnO_2 NT (Figure 5-30a to c), where the electrode keeps good core/shell structural feature even after 8000 cycles of random cycling. The Ragone plot (power density vs energy density) of the electrode at various current densities is shown in Figure 5-30d, which delivers a high power density of about 56 $kWkg^{-1}$ at the energy density of about 61 $kWhkg^{-1}$. The energy and power density in this study reveals that the Pt/MnO_2 NT-based

electrodes fulfil the power requirement (15 $kWkg^{-1}$) for PNGV (Partnership for a New Generation of Vehicles).

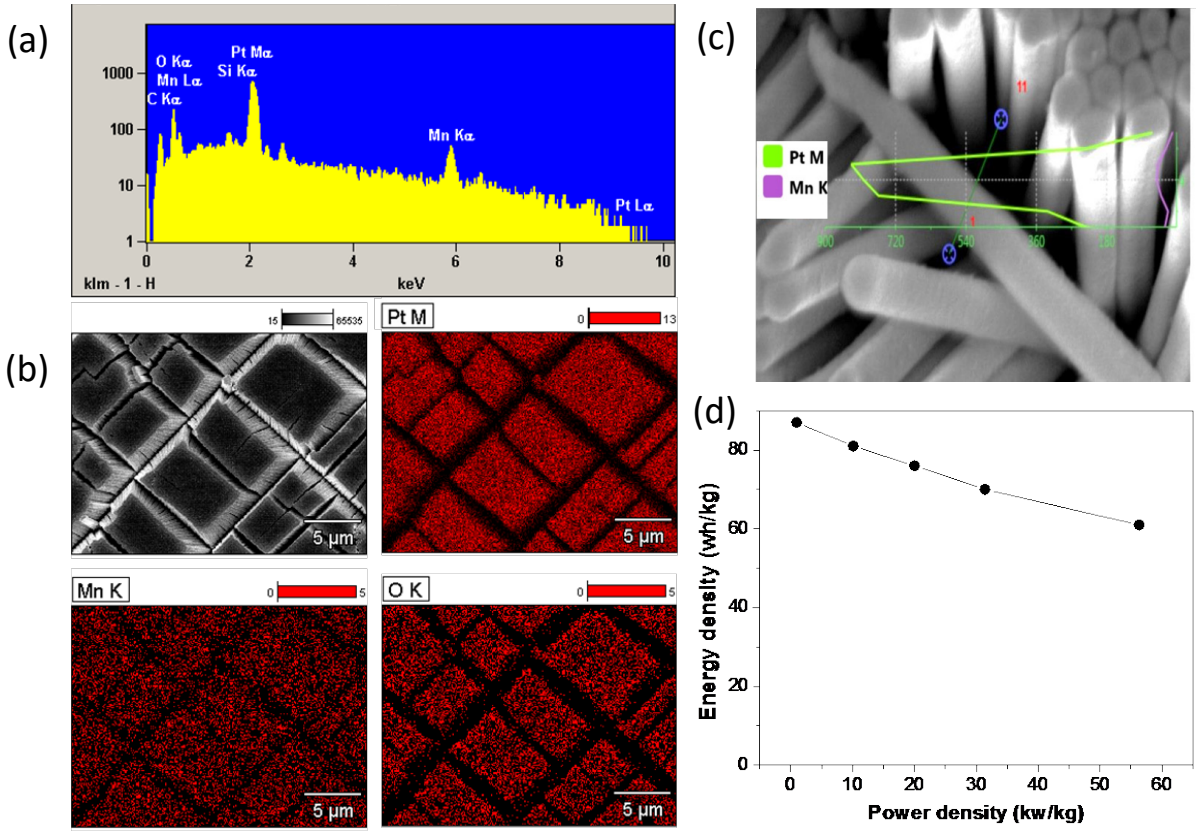

Figure 5-29. The 30s-NT electrode after 8000 cycles of random charging-discharging test: (a) the EDX spectrum; (b) EDX mapping of the platinum, oxygen and manganese elements on a 20 µm×20 µm area; (c) EDX line scan of a single Pt/MnO_2 NT. (d) Ragone plots (energy density vs power density) of 30s-NT electrode at various current densities.

5.7 Manipulation of charge transfer and transport in nano-Au/PZT hybrids for photoelectrochemical applications

5.7.1 Background

For photoelectrochemical (PEC) systems based on plasmonics, in addition to scattering effect in metallic nanostructures,[143, 144] three factors play decisive roles: the Schottky junction at the interface between the metallic nanoparticle and the semiconductor, enabling the capture of hot

electrons generated in photon-stimulated nano-metals to semicondcutors;[175, 184] the interface between the semiconductor and electrolyte, governing the transfer of the hot carriers from the semiconductor to the electrolyte; and the transport of hot carriers between the two interfaces. Considering that the properties of the Schottky junction are fixed for a given combination of a metal and a semiconductor, the other two factors are crucial for adjusting the PEC performance. Particularly the semiconductor/electrolyte interface is important, since the band-bending is either upward (from semiconductor to electrolyte) for an easy hole transfer or downward to facilitate electron transfer to the electrolyte.[169, 209, 210] As a conventional PEC semiconductor, TiO_2 has been widely used in water splitting for collecting hot electrons from plasmonic nanostructures.[210-219] However, Pt nanoparticles or other catalysts have to be adopted to adjust the upward band-bending at the TiO_2/electrolyte interface that inhibits the transfer of electrons in the conduction band of TiO_2 to the electrolyte.[8, 132] Though different approaches have been followed to tune the plasmonic properties of metallic nanostructures in order to enhance the PEC performance,[220-222] insightful mechanism and technique proposed for tailoring both the band-bending at the semiconductor/electrolyte interface and the transport of hot carriers in the PEC film, preferably at the same time, have so far been lacking. Here, we present an approach where conventional semiconductor has been replaced by ferroelectric $Pb(Zr,Ti)O_3$ (PZT) which possesses a large, stable and manipulable remnant polarization.[223-226] The associated depolarization electric field (E_{DP}), extending over the entire thin film volume, enables tuning the band-bending at the ferroelectric/electrolyte interface by poling pretreatments and thus adding extra functionality for scavenging and conducting the excited charges. Manipulation of the charge transfer and transport in nano-Au/PZT hybrids by placing nano-Au array in different positions within ITO/PZT and by poling the PZT films with different potentials are conducted in this chapter. Among the PEC electrodes (as-grown), the structure of ITO/nano-Au/PZT provides the best performance

among the three structures. On the other hand, using the ITO/PZT/nano-Au/PZT electrodes, tuning of the short circuit photocurrent by nearly an order of magnitude is obtained, when the pre-poling bias is switched from +10 V to –10 V. The transport studies are accompanied by femtosecond transient absorbance study to track the dynamics of the hot charge transfer from Au nanoparticles to PZT. Such simultaneous manipulation of the charge-transfer and interface-related PEC phenomena within a given nano-metal/PEC film/electrolyte system presents a novel route to optimally and flexibly manipulate the photo-excited charges for PEC energy conversion (*e.g.* solar water splitting).

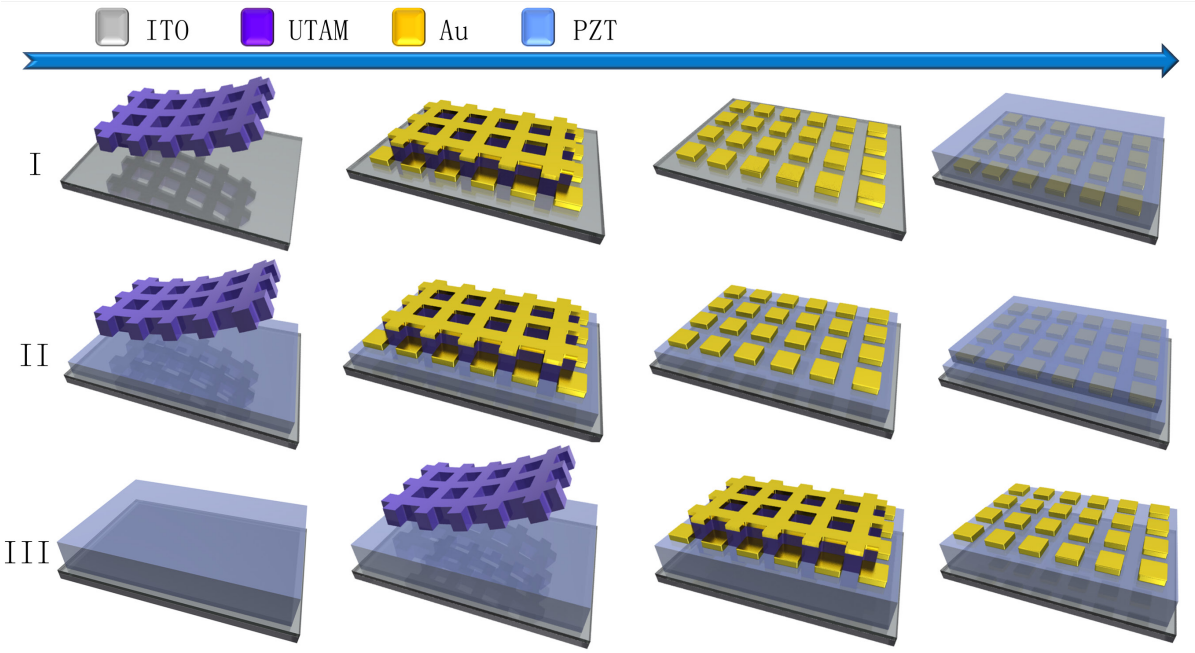

Figure 5-30. Schematic of fabrication processes for preparing the nano-Au/PZT hybrids as photoelectrodes. Process I, the procedure for fabricating the nano-Au array at the interface of ITO/PZT (structure: ITO/nano-Au/PZT). Process II, the procedure for embedding the nano-Au array in the PZT films (structure: ITO/PZT/nano-Au/PZT), poling treatment is performed on this structure for investigating the impact of the orientation of ferroelectric polarization on the PEC performance. Process III, the procedure for making nano-Au array on top of ITO/PZT (structure: ITO/PZT/nano-Au).

5.7.2 Preparation of nano-Au/PZT hybrids

Figure 5-30 summarizes the fabrication processes used for preparing different nano-Au/PZT hybrids as PEC photoelectrodes. Well-ordered Au nanodot array is prepared utilizing a well-established UTAM technique in section 5.3.5. A representative top-view SEM image is

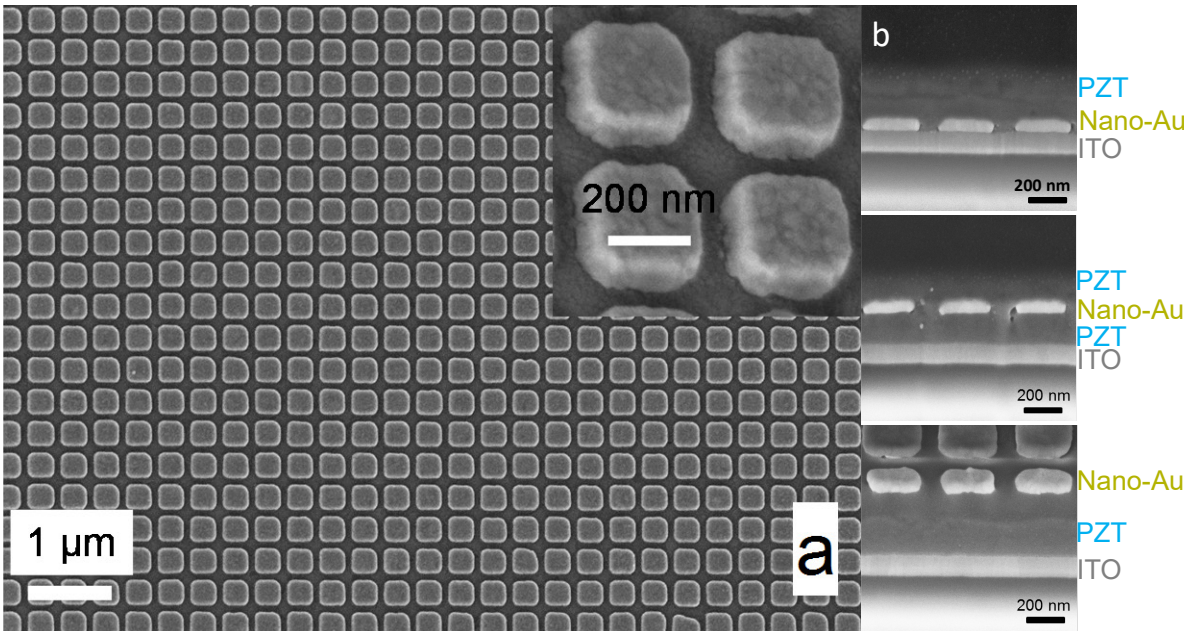

Figure 5-31. (a) A representative top-view SEM image of a squarely shaped nano-Au array. (b) Cross-sectional SEM images of the nano-Au arrays placed at different positions within ITO/PZT.

shown in Figure 5-31, where the spacing between the square-shaped Au nanodots is about 130 nm, the dot dimension is gauged at about 270 x 270 nm^2 and the thickness of dot is 60 nm (the inset in Figure 5-31a). For placing the Au nanodot array at different positions within ITO/PZT, a spin-coating process is applied for obtaining high quality PZT films. The precursor solution for the coating is prepared by dissolving an appropriate amount of lead acetate ($Pb(CH_3COO)_2 \cdot 5H_2O$) in acetic acid at room temperature in air. A stoichiometric amount of titanium isopropoxide ($Ti((CH_3)_2CHO)_4$) and zirconium isopropoxide ($Zr((CH_3)_2CHO)_4$) is slowly added to the precursor solution. Subsequently, 2-methoxyethanol is added to adjust the concentration until a clear yellow sol with a molar concentration of 0.2

mol L^{-1} is obtained. A 10 mol% excess amount of lead acetate is used to compensate the Pb evaporation during annealing. The wet films are dried at 150°C for 5 min in air and annealed at 400°C for 10 min. Finally, the films are crystallized in air atmosphere under 550ºC for two hours. The Au nanodot arrarys are prepared before or after the growth of PZT film (Figure 5-31b).

5.7.3 Optimization of nano-Au/PZT hybrids for photoelectrochemical cell

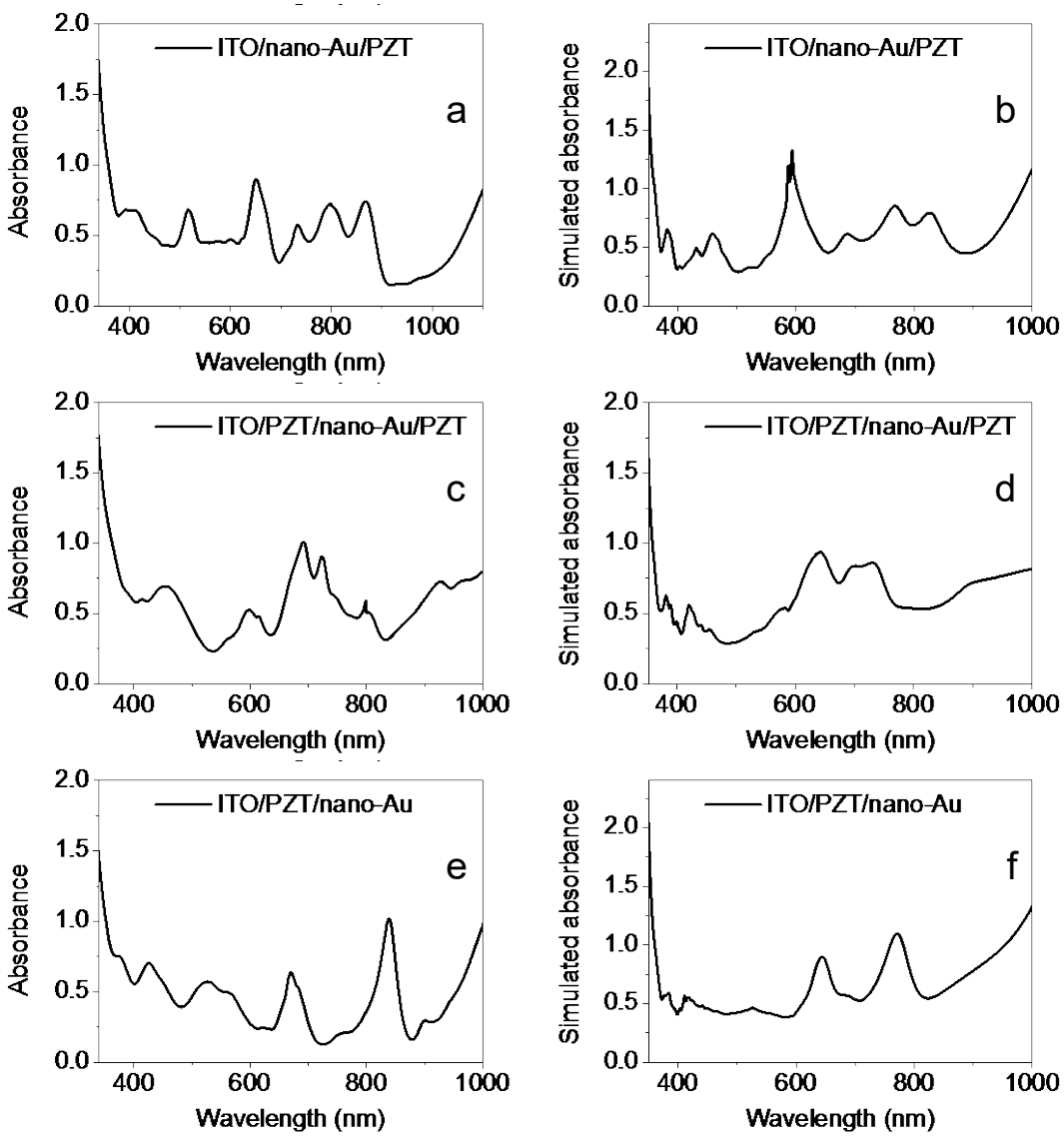

Figure 5-32. Measured absorbance spectra (left panels) compared to the FDTD simulated spectra (right panels) of the ITO/nano-Au/PZT, ITO/PZT/nano-Au/PZT and ITO/PZT/nano-Au.

Figure 5-32 presents the absorbance spectra of hybrid structures with nano-Au placed at different positions within the ITO/PZT multilayer. The spectra differ considerably from the spectra of the pure ITO/nano-Au structure. This is due to the change of the dielectric surroundings of nano-Au and the Fabry-Perot interferences. The simulated spectra of relevant structures are presented in the right panels, demonstrating a qualitative agreement with the measured ones.

Figure 5-33a presents the representative steady-state external quantum efficiency (EQE) spectra of PEC electrodes of ITO/PZT and ITO/nano-Au/PZT (note that the corresponding internal quantum efficiency would be at least an order of magnitude higher). Compared to the bare (intrinsic) PZT photoelectrode on ITO substrate, the nano-Au/PZT photoelectrode exhibits a distinctive EQE for photon energies below the absorption threshold of PZT (Eg=3.6eV). The spectrum of the EQE qualitatively matches the absorbance spectrum of nano-Au/PZT (Figure 5-32a), demonstrating the occurrence of hot electron injection from the excited nano-Au to PZT. Photocurrent–potential profiles are measured by soaking the photoelectrodes into 0.1 M Na_2SO_4 aqueous solutions. Each plot represents typical photo-response obtained by illumination with a standard 300 W Xe lamp (Newport). To get the photocurrent signal from nano-Au array solely, a 455 nm low pass optical filter is used to avoid the excitation of PZT. The light intensity is characterized as 100 mW cm^{-2}. As illustrated in Figure 5-33b, the ITO/nano-Au/PZT electrode possesses a distinct PEC performance with a short circuit current around 10 μA cm^{-2} and an open circuit potential close to 0.6 V vs Ag/AgCl. The photocurrent direction is cathodic, demonstrating that it is the hot electrons that have been transferred from the nano-Au to the PZT/electrolyte and hence initiate the PEC reactions.

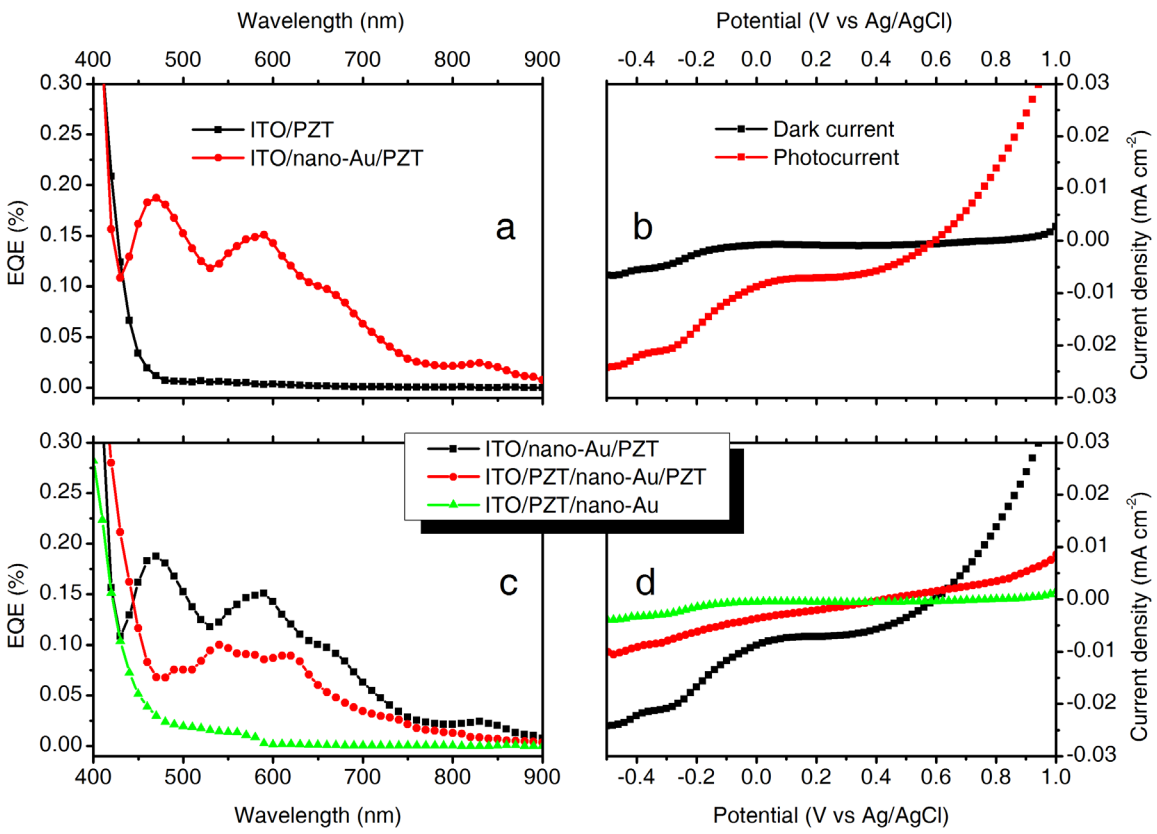

Figure 5-33. Comparison of the PEC responses from photoelectrodes with nano-Au arrays placed to various positions in the structure of ITO/PZT. a, External quantum efficiency spectra of the PEC electrodes of ITO/PZT and ITO/nano-Au/PZT, respectively. b, Current density−potential curves of the ITO/nano-Au/PZT photoelectrodes under white light excitation (filtered, λ>450 nm), compared to dark measurement. c, External quantum efficiency spectra of the electrodes of ITO/nano-Au/PZT(black), ITO/PZT/nano-Au/PZT (red) and ITO/PZT/nano-Au (green). d, Photocurrent–potential measurements of the samples in c under the white light excitation (filtered, λ>450 nm).

Two strategies are adopted to manipulate the hot electron injection efficiency and to optimize the PEC performance: adjusting the positions of nano-Au within the ITO/PZT and tuning the ferroelectric polarization in PZT films with external potential. First, the nano-Au array is placed in varied positions: at the interface of ITO/PZT, in the middle of PZT films and on the

top of PZT films, respectively (as shown in Figure 5-31). PEC results in Figure 5-33c and d show that the electrodes (as-grown) with nano-Au array at the ITO/PZT interface have the best performance among these three structures. The Schottky barrier of ITO/PZT is 1.03 eV.[226, 227] When the nano-Au array is placed in the depletion region of such Schottky contact, with continuously varying band-bending, the collection and conduction of hot electrons injected into PZT should be more efficient. Importantly, the work function of Au is larger than that of ITO,[228] which supports the transfer of photo-generated holes in nano-Au into ITO. Considering the fact that the valence band position of PZT is almost 1.5 eV below the work function of Au,[226] it is on the other hand for the remaining holes in the Au to overcome the barrier at the Au/PZT interface and be collected by the external circuit when the nano-Au array is sandwiched within the PZT films. This can be relaxed if the ferroelectric domain structure is optimized by poling treatment.[229] As to the electrodes with the nano-Au array located on the top of the PZT, even though hot electrons can be injected into the PZT, the 1.03 eV Schottky barrier at the ITO/PZT interface prevents the electrons from being transferred to the external circuit.

The tunability of the E_{DP} in PZT films offers another opportunity to manipulate hot electron injection and transfer. Experiments are conducted by poling the electrodes with different potentials in a propylene carbonate solution. As shown in Figure 5-34a, +10 V poling pretreatment results in the highest EQE compared to the same electrodes undergone –10 V poling and no poling treatments, respectively. This EQE value is even higher than that of the ITO/nano-Au/PZT electrodes, indicating that the poling condition in PZT is crucial for optimizing the PEC performance. The –10 V poling treatment strongly suppresses the EQE while the as-grown sample shows an intermediate EQE, suggesting that the ferroelectric domains in the as-grown polycrystalline PZT films are randomly distributed. Correspondingly, the photocurrent–potential plots, displayed in Figure 5-34b, demonstrate the

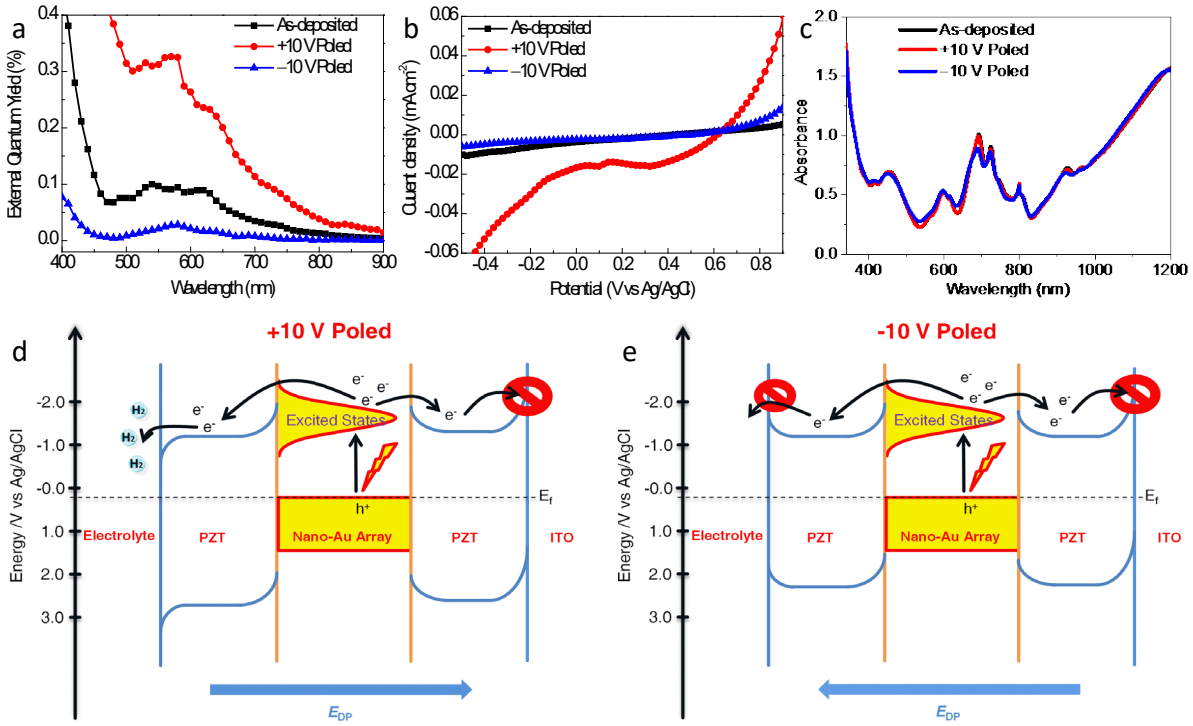

Figure 5-34. Polarization switching behavior and the schematic representations of the electronic band structure in the ITO/PZT/nano-Au/PZT photoelectrode. a and b, External quantum efficiency spectra and photocurrent–potential measurements (under the filtered white light excitation) of the as-grown(black), +10 V (red) and –10 V (blue) poled samples. c, Absorbance spectra of photoelectrode after different poling condition, 0 V (black), +10 V (red) and –10 V (blue). d and e, Schematic electronic structure and the mechanisms for the injected hot electron transfer from PZT films to the electrolyte for the two poling configurations.

same tendency. The short circuit current can thus be tuned from 2.4 μA cm^{-2} to 16.7 μA cm^{-2} (for white light excitation density of 100 W/cm^2) just by switching the poling conditions from –10 V to +10 V. The effect of the poling conditions on the absorbance of this structure is shown in Figure 5-34c, where no pronounced changes in the absorbance could be observed. The randomly oriented ferroelectric domains in the as-grown PZT films can be poled using electric fields larger than the coercive field.[230] In this way, the direction of E_{DP} can be correspondingly switched.[231, 232] The +10 V poling potential induces an E_{DP} with the

direction pointing towards the ITO substrate and a downward band-bending at the PZT/electrolyte interface (Figure 5-34d). This configuration is favorable for the injected hot electrons being transferred to the interface and driving the PEC reactions. The optimized E_{DP} across the entire PZT films could also be helpful for transferring the excited holes to ITO electrode.[229] The –10 V poling potential, however, switches the direction of the E_{DP}, which points towards the PZT/electrolyte interface and renders an upward band-bending at the PZT/electrolyte interface (Figure 5-34d). In this case, the hot electrons injected into the PZT cannot be transferred to the PZT/electrolyte interface and get trapped in the bulk of the PZT film.

Figure 5-35a presents the time evolution of the relative transmission changes (ΔT/T) recorded on the nano-Au array on ITO/glass. Here two distinct, spectrally well separated components can be identified (Figure 5-35d), the enhanced transmission peaked at about 1.65 eV (~750 nm) and the reduced transmission peaked at about 2.5 eV. The former can be linked to the photo-induced changes in absorbance due to the photo-induced changes in the LSPR centered at about 1.5 eV (Figure 5-32b). Photoexcitation, the resulting electron-electron and electron-phonon thermalization result in broadening of the LSPR due to the enhanced scattering.[233, 234] The strongest photo-induced changes in transmission, caused by the broadening of the LSPR, may be expected near the LSPR for photon energies where the linear transmission strongly varies with the photon energy. Apart from the broadening of the LSPR, the photo-induced shift of the central frequency may be expected due to the photo-induced expansion, particularly for longer time delays.[233]

Even more pronounced is the photo-induced decrease of transmission, peaked at about 2.5 eV. We attribute this peak to a bulk-like response of Au, governed by the photo-induced changes in the joint density of states for the optical transition between the d-band and Fermi level (E_f).

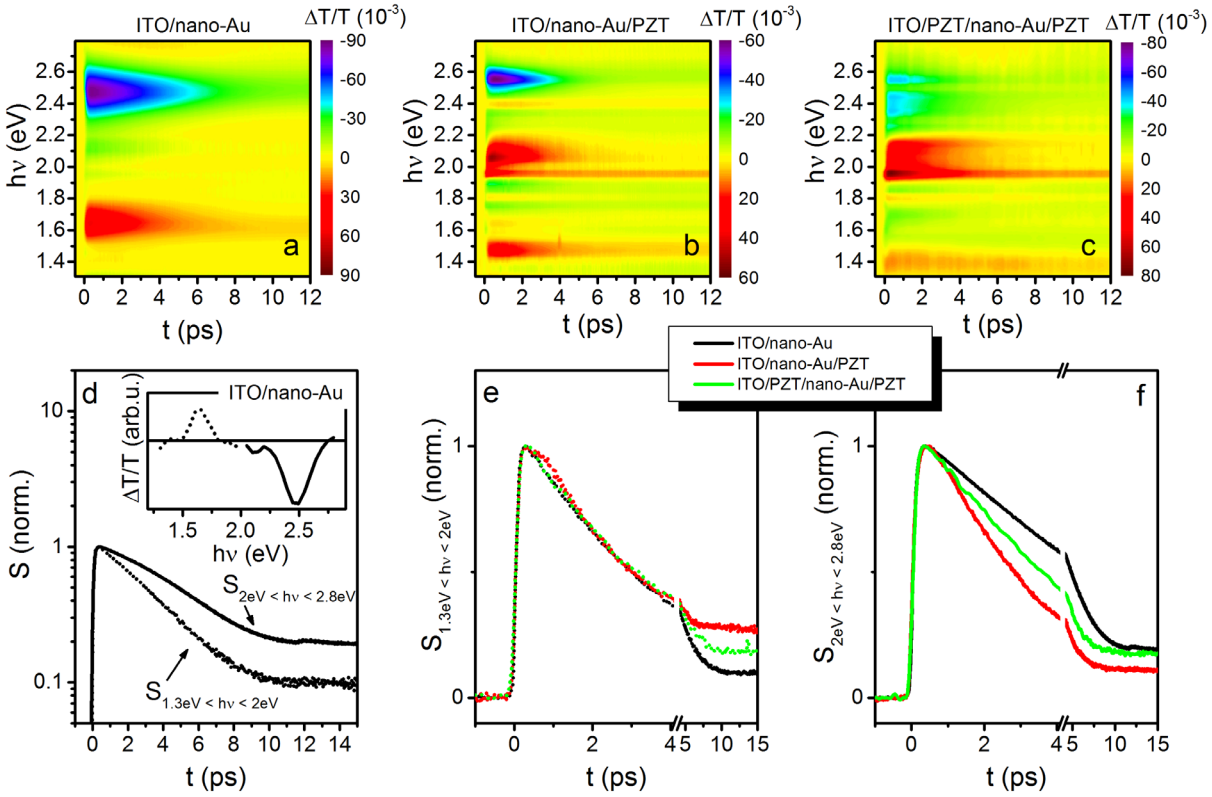

Figure 5-35. Transient absorbance spectroscopy on the nano-Au hybrids. a Photo-induced transmission (ΔT/T) spectra recorded on an ITO/nano-Au, b ITO/nano-Au/PZT and c ITO/PZT/nano-Au/PZT, following photoexcitation with 70 fs UV pulses at 400 nm. d The time evolution of the spectra in ITO/nano-Au. The dotted line presents the time evolution of the low frequency range (1.3 eV < hν < 2 eV), while the solid line corresponds to the high frequency (2 eV < hν < 2.8 eV). Comparison of the low frequency (e) and high frequency (f) dynamics between the three nano-Au hybrids. The high frequency response demonstrates the speeding up of relaxation in nano-Au/PZT hybrids, consistent with the existence of an additional relaxation channel (Au-PZT charge transfer).

Indeed, the spectral shape of the induced change in transmission (inset of Figure 5-35d) matches well the results obtained on extended thin films.[235] Unlike in gold nanoparticles with lateral dimensions on the 10 nm scale, where the LSPR spectrally overlaps with the d-

band to E_f transition,[233] the two spectral features are well separated in our case. The photo-induced transmission spectra recorded on ITO/nano-Au/PZT (Figure 5-35b) and ITO/PZT/nano-Au/PZT (Figure 5-35c) are much more complicated. This can be linked to the complicated linear transmission spectra (Figure 5-32) caused by Fabry-Perot interference due to the additional PZT layer(s). Nevertheless, the reduced transmission in the high frequency range and bleaching absorbance in the low frequency part of the spectra are still recognizable.

Let us now address the dynamical aspect of the data. The rise-time (20% − 80%) is resolution limited (~120 fs) for all samples. Plotting $\Delta T/T(t)$ in ITO/nano-Au for photon energies at the two spectral peaks we find, however, that their respective $\Delta T/T$ decays with considerably different time constants. To avoid artifacts that can arise due to the time dependent spectral shifts (particularly critical for data with narrow spectral features as in Figure 5-35 b and c), we analyzed the time evolution of the low frequency ($1.3\ eV < h\nu < 2\ eV$) and high frequency ($2\ eV < h\nu < 2.8\ eV$) responses separately. Applying singular value decomposition on both spectral ranges, we demonstrate that the photo-induced transient spectra in each of the spectral ranges can be well reproduced by single components (their spectral weights are about 90% of the entire signal), with their respective temporal traces given by S(t). Figure 5-35d presents their time evolutions on ITO/nano-Au, the corresponding spectra are shown in inset. It should be noted that, while the two spectral ranges are Kramers-Kronig connected, the fact that the underlying excitations (LSPR and the interband transition) are well spectrally separated justifies this approach.

There are two noteworthy observations as far as the dynamics is concerned. First, the relaxation of the high frequency part is substantially slower. Secondly, while the dynamics of the low frequency part is well described by an exponential decay, the high frequency part clearly displays a non-exponential relaxation, which can be well seen on the semi-log plot. Considering the different natures of the two processes, the observation may not be too

surprising. The relaxation of the LSPR is governed by the time-evolution of the (collective) plasma scattering rate, while the interband transition is governed by the photoexcited quasiparticle density and their distribution. Indeed, for the high frequency part, the slope of S(t) changes with time, suggesting the presence of multiple decay channels.[236] Since this component corresponds to a bulk-like interband transition, the carrier diffusion (ballistic transport) into the 60 nm thick Au nanoparticles, competing with electron-phonon thermalization, could be the origin of the observed functional form of S(t).[236]

Further evidence for the above suggestion comes from the comparison of relaxation dynamics between different samples. While no measurable changes are observed for the low frequency part (Figure 5-35e), the high frequency part (Figure 5-35f) shows a pronounced variation of relaxation rates, recovering substantially faster in nano-Au/PZT hybrids. The relaxation rates show a clear trend: $\tau^{-1}_{\mathrm{ITO/nano-Au/PZT}} > \tau^{-1}_{\mathrm{ITO/PZT/nano-Au/PZT}} > \tau^{-1}_{\mathrm{ITO/nano-Au}}$. Since photoconductivity data demonstrate a substantial charge transfer from nano-Au to PZT, with the highest efficiency in ITO/nano-Au/PZT (Figure 5-33c), we suggest that the nano-Au−PZT charge transfer may be responsible for speeding up the relaxation of the high frequency spectral component in nano-Au/PZT hybrids.

These cumulative evidences point out that the hot electron injection from excited nano-Au to the ferroelectric material mirrors the hot electron transfer in nano-Au/semiconductor structures in terms of hot electron collection. However, the employment of ferroelectric material in plasmonic hybrids introduces another dimension to effectively manipulate the PEC properties. The tunable electric polarization offers a flexible platform to freely utilize the optical energy collected in nano-metals. In this regard, the hot electrons could be either conducted to the ferroelectric/electrolyte interface to drive PEC reduction reactions or be transferred to the bulk of the ferroelectric material leaving the holes to initiate PEC oxidation reactions, just by switching the direction of the depolarization field in the ferroelectric films.

Moreover, adding an additional finger type electrode on top of the device would enable in-situ control of the device performance. This concept could have a great impact on the field of solar fuel generation by water splitting or carbon dioxide reduction. This merit is beyond the capabilities of conventional semiconductors. At semiconductor/electrolyte interface, the PEC reactions are fixed by the specific band bending, which cannot be manipulated without changing the semiconductor or the electrolyte or both. Considering that the optimized depolarization electric field across the entire ferroelectric film is beneficial for capturing and conducting the hot charges in an efficient way, the energy conversion efficiency of our system is superior over the conventional system. Further improvement can be expected by optimizing the plasmonic configuration and the redox couple.

6 Summary and outlook

In summary, an innovatively template-guided technique is demonstrated to fabricate diverse binary nanostructure arrays. The main contributions of this dissertation can be summarized in the following aspects:

(1) A perfectly ordered binary-pore template with highly morphological controllability (e.g., size of A-pores, size of B-pores, and shape of B-pores) is successfully achieved to centimeter-scale by a selective etching in 0.1 M NaOH, a pore widening in 5 w% H_3PO_4 and a combination of both processes. The key feature of the binary-pore template is originated from the distinctive double barrier layers of A-pores and B-pores located at the opposite side of the template.

(2) Combing with the conventional fabrication techniques (e.g., electrodeposition, ALD, and PVD), tremendous binary nanostructure arrays are realized, including the nanowire/nanowire, nanowire/nanotube, nanotube/nanotube, nanowire/core-shell nanowire, and nanodot/nanodot, in which the morphology, length and composition of each sub-array can be independently adjusted to a broad range.

(3) The detailed microstructure investigation and COMSOL simulation are conducted to understand the formation of binary-pore template. The reason might originate from the combined effects of electric-field and mechanical stress field around the imprinted concave sites during different periods of anodization. Under the same mechanism, the binary-pore template is easily upgraded to ternary- or quadruple-pore array with more morphological options and higher pore densities.

(4) The greatly flexible combinations of the different component arrays generate many possibilities for achieving superior ‘functional-functional’ and ‘controlling-functional’ devices, such as ‘TiO_2/Cu_2O’ Z-scheme photosynthesis unit and ‘ZnO/AZO’ addressable multi-gate nanowire transistor.

(5) For improving the supercapacitor performance based on MnO_2, Pt/MnO_2 core/shell NT array is constructed with the assistance of ALD and electrodeposition. This core/shell NT electrode exhibits a high gravimetric and areal specific capacitance (810 Fg^{-1} and 75 $mFcm^{-2}$ at 5 mVs^{-1}) as well as an excellent rate capability (68% capacitance retention from 2 to 100 Ag^{-1}). A negligible capacitance loss is observed after 8000 random charging-discharging cycles from 2 to 100 Ag^{-1}. These good performances can be attributed to the well-defined Pt NT arrays, which provide a high accessible surface area and inter-tube gaps for fast and reversible Faradic reactions and short ion diffusion paths.

(6) In order to capture and utilize hot electrons from light-stimulated nano-metals modulate, nano-Au/PZT hybrid is constructed on ITO substrates. In addition to varying the photocurrent by placing the nano-Au array at different positions in ITO/PZT, the orientation of ferroelectric domains is employed to manipulate the photocurrent. For ITO/PZT/nano-Au/PZT electrodes, the short circuit photocurrent can be changed by nearly an order of magnitude when changing the ferroelectric polarization in the PZT films by pre-poling. Femtosecond transient absorbance studies reveal a faster carrier relaxation dynamics in nano-Au/PZT hybrids, providing insights into the nature of charge transfer between the nano-Au and PZT. This demonstrates a versatile and tunable system for energy harvesting.

From the optimized composition and structure of Pt/MnO_2 supercapacitor and nano-Au/PZT hybrid, superior performances of ‘functional-functional’ and ‘controlling-functional’ devices based on binary nanostructure arrays are highly expectable. Such as, a high efficiency of ‘TiO_2/Cu_2O Z-scheme’ could be realized by enhancing the light utilization of TiO_2 with the introduction of core/shell structures (e.g., AZO/TiO_2) and integration of narrow bandgap semiconductor (e.g., CdS), and increasing the stability of Cu_2O with a surface modification or coating (e.g., Cu_2O/ZnO/TiO_2 core/shell structure). Second, in order to compete with the performance of conventional film transistors, the key parameters of the ZnO/AZO transistor

are still need to be optimized, like the ZnO growth condition, the length of the ZnO nanowire, and the thickness of the dielectric Al_2O_3 layer.

Besides the binary semiconductor/semiconductor arrays, unique optical properties based on the binary metal/metal arrays are also highly expectable, such as the 'functional-functional' devices based on different metals (e.g., Au, Ag, and Al), or the 'controlling-functional' devices based on magnetics (e.g., Fe, Co, and Ni) and metals (e.g., Au, Ag, and Al). Thus, even more fruitful results might be possible by combining the binary metal/metal arrays with semiconductor or ferroelectric materials.

Considering the countless binary nanostructure arrays, the developed technique in this dissertation could raise a new horizon to the 'nanostructure array' in the modern and future devices.

7 Bibliography

[1]. Kelzenberg, M. D.; Boettcher, S. W.; Petykiewicz, J. A.; Turner-Evans, D. B.; Putnam, M. C.; Warren, E. L.; Spurgeon, J. M.; Briggs, R. M.; Lewis, N. S.; Atwater, H. A. *Nat Mater* **2010,** 9, (3), 239.
[2]. Luk'yanchuk, B.; Zheludev, N. I.; Maier, S. A.; Halas, N. J.; Nordlander, P.; Giessen, H.; Chong, C. T. *Nat Mater* **2010,** 9, (9), 707.
[3]. Tomioka, K.; Yoshimura, M.; Fukui, T. *Nature* **2012,** 488, (7410), 189.
[4]. Li, K. H.; Liu, X.; Wang, Q.; Zhao, S.; Mi, Z. *Nat Nanotechnol* **2015,** 10, (2), 140.
[5]. Pan, C. F.; Dong, L.; Zhu, G.; Niu, S. M.; Yu, R. M.; Yang, Q.; Liu, Y.; Wang, Z. L. *Nat Photonics* **2013,** 7, (9), 752.
[6]. Wu, W. Z.; Wen, X. N.; Wang, Z. L. *Science* **2013,** 340, (6135), 952.
[7]. Fan, Z. Y.; Razavi, H.; Do, J. W.; Moriwaki, A.; Ergen, O.; Chueh, Y. L.; Leu, P. W.; Ho, J. C.; Takahashi, T.; Reichertz, L. A.; Neale, S.; Yu, K.; Wu, M.; Ager, J. W.; Javey, A. *Nat Mater* **2009,** 8, (8), 648.
[8]. Mubeen, S.; Lee, J.; Singh, N.; Kramer, S.; Stucky, G. D.; Moskovits, M. *Nat Nanotechnol* **2013,** 8, (4), 247.
[9]. Wallentin, J.; Anttu, N.; Asoli, D.; Huffman, M.; Aberg, I.; Magnusson, M. H.; Siefer, G.; Fuss-Kailuweit, P.; Dimroth, F.; Witzigmann, B.; Xu, H. Q.; Samuelson, L.; Deppert, K.; Borgstrom, M. T. *Science* **2013,** 339, (6123), 1057.
[10]. Banerjee, P.; Perez, I.; Henn-Lecordier, L.; Lee, S. B.; Rubloff, G. W. *Nat. Nanotechnol.* **2009,** 4, (5), 292.
[11]. Taberna, L.; Mitra, S.; Poizot, P.; Simon, P.; Tarascon, J. M. *Nat Mater* **2006,** 5, (7), 567.
[12]. Liu, C. Y.; Gillette, E. I.; Chen, X. Y.; Pearse, A. J.; Kozen, A. C.; Schroeder, M. A.; Gregorczyk, K. E.; Lee, S. B.; Rubloff, G. W. *Nat Nanotechnol* **2014,** 9, (12), 1031.
[13]. Shegai, T.; Chen, S.; Miljkovic, V. D.; Zengin, G.; Johansson, P.; Kall, M. *Nat Commun* **2011,** 2.
[14]. Liu, N.; Tang, M. L.; Hentschel, M.; Giessen, H.; Alivisatos, A. P. *Nat Mater* **2011,** 10, (8), 631.
[15]. Jang, J. W.; Du, C.; Ye, Y. F.; Lin, Y. J.; Yao, X. H.; Thorne, J.; Liu, E.; McMahon, G.; Zhu, J. F.; Javey, A.; Guo, J. H.; Wang, D. W. *Nat Commun* **2015,** 6.
[16]. Reece, S. Y.; Hamel, J. A.; Sung, K.; Jarvi, T. D.; Esswein, A. J.; Pijpers, J. J. H.; Nocera, D. G. *Science* **2011,** 334, (6056), 645.
[17]. Zhang, G.; Wang, D. Y.; Mohwald, H. *Nano Lett.* **2007,** 7, (1), 127.
[18]. Zhang, G.; Wang, D. Y. *J. Am. Chem. Soc.* **2008,** 130, (17), 5616.
[19]. Shegai, T.; Johansson, P.; Langhammer, C.; Kall, M. *Nano Lett.* **2012,** 12, (5), 2464.
[20]. Shin, D. O.; Mun, J. H.; Hwang, G.-T.; Yoon, J. M.; Kim, J. Y.; Yun, J. M.; Yang, Y.-B.; Oh, Y.; Lee, J. Y.; Shin, J.; Lee, K. J.; Park, S.; Kim, J. U.; Kim, S. O. *Acs Nano* **2013**.
[21]. Masuda, H.; Yasui, K.; Nishio, K. *Adv. Mater.* **2000,** 12, (14), 1031.
[22]. Mei, X.; Kim, D.; Ruda, H. E.; Guo, Q. X. *Appl. Phys. Lett.* **2002,** 81, (2), 361.
[23]. Lei, Y.; Chim, W. K. *Chem. Mater.* **2005,** 17, (3), 580.
[24]. Lei, Y.; Chim, W. K. *J. Am. Chem. Soc.* **2005,** 127, (5), 1487.
[25]. Lei, Y.; Chim, W. K.; Sun, H. P.; Wilde, G. *Appl. Phys. Lett.* **2005,** 86, (10), 103106.
[26]. Lei, Y.; Chim, W. K.; Weissmuller, J.; Wilde, G.; Sun, H. P.; Pan, X. Q. *Nanotechnology* **2005,** 16, (9), 1892.
[27]. Lei, Y.; Cai, W. P.; Wilde, G. *Prog. Mater Sci.* **2007,** 52, (4), 465.
[28]. Zhan, Z. B.; Lei, Y. *Acs Nano* **2014,** 8, (4), 3862.

[29]. Lei, Y.; Zhang, L. D.; Meng, G. W.; Li, G. H.; Zhang, X. Y.; Liang, C. H.; Chen, W.; Wang, S. X. *Appl. Phys. Lett.* **2001,** 78, (8), 1125.
[30]. Liu, C. H.; Zapien, J. A.; Yao, Y.; Meng, X. M.; Lee, C. S.; Fan, S. S.; Lifshitz, Y.; Lee, S. T. *Adv. Mater.* **2003,** 15, (10), 838.
[31]. Wen, L. Y.; Shao, Z. Z.; Fang, Y. G.; Wong, K. M.; Lei, Y.; Bian, L. F.; Wilde, G. *Appl. Phys. Lett.* **2010,** 97, (5), 053106.
[32]. Martin, C. R. *Adv. Mater.* **1991,** 3, (9), 457.
[33]. Bao, J. C.; Wang, K. Y.; Xu, Z.; Zhang, H.; Lu, Z. H. *Chem. Commun.* **2003**, (2), 208.
[34]. Gu, D. F.; Baumgart, H.; Abdel-Fattah, T. M.; Namkoong, G. *Acs Nano* **2010,** 4, (2), 753.
[35]. Lee, W.; Park, S. J. *Chem. Rev.* **2014,** 114, (15), 7487.
[36]. Zhao, H. P.; Zhou, M.; Wen, L. Y.; Lei, Y. *Nano Energy* **2015,** 13, 790.
[37]. Lee, W.; Ji, R.; Gosele, U.; Nielsch, K. *Nat Mater* **2006,** 5, (9), 741.
[38]. Lee, W.; Schwirn, K.; Steinhart, M.; Pippel, E.; Scholz, R.; Gosele, U. *Nat Nanotechnol* **2008,** 3, (4), 234.
[39]. Qin, L. D.; Park, S.; Huang, L.; Mirkin, C. A. *Science* **2005,** 309, (5731), 113.
[40]. Qin, L. D.; Zou, S. L.; Xue, C.; Atkinson, A.; Schatz, G. C.; Mirkin, C. A. *P Natl Acad Sci USA* **2006,** 103, (36), 13300.
[41]. Osberg, K. D.; Schmucker, A. L.; Senesi, A. J.; Mirkin, C. A. *Nano Lett.* **2011,** 11, (2), 820.
[42]. Pedano, M. L.; Li, S. Z.; Schatz, G. C.; Mirkin, C. A. *Angew Chem Int Edit* **2010,** 49, (1), 78.
[43]. Qin, L.; Banholzer, M. J.; Millstone, J. E.; Mirkin, C. A. *Nano Lett.* **2007,** 7, (12), 3849.
[44]. Banholzer, M. J.; Osberg, K. D.; Li, S. Z.; Mangelson, B. F.; Schatz, G. C.; Mirkin, C. A. *ACS Nano* **2010,** 4, (9), 5446.
[45]. Wei, W.; Li, S. Z.; Millstone, J. E.; Banholzer, M. J.; Chen, X. D.; Xu, X. Y.; Schatz, G. C.; Mirkin, C. A. *Angew Chem Int Edit* **2009,** 48, (23), 4210.
[46]. Osberg, K. D.; Rycenga, M.; Harris, N.; Schmucker, A. L.; Langille, M. R.; Schatz, G. C.; Mirkin, C. A. *Nano Lett.* **2012,** 12, (7), 3828.
[47]. Bourret, G. R.; Ozel, T.; Blaber, M.; Shade, C. M.; Schatz, G. C.; Mirkin, C. A. *Nano Lett.* **2013,** 13, (5), 2270.
[48]. Mangelson, B. F.; Jones, M. R.; Park, D. J.; Shade, C. M.; Schatz, G. C.; Mirkin, C. A. *Chem. Mater.* **2014,** 26, (12), 3818.
[49]. Mangelson, B. F.; Park, D. J.; Ku, J. C.; Osberg, K. D.; Schatz, G. C.; Mirkin, C. A. *Small* **2013,** 9, (13), 2250.
[50]. Qin, L. D.; Banholzer, M. J.; Xu, X. Y.; Huang, L.; Mirkin, C. A. *J. Am. Chem. Soc.* **2007,** 129, (48), 14870.
[51]. Chen, X. D.; Braunschweig, A. B.; Wiester, M. J.; Yeganeh, S.; Ratner, M. A.; Mirkin, C. A. *Angew Chem Int Edit* **2009,** 48, (28), 5178.
[52]. Chen, X. D.; Yeganeh, S.; Qin, L. D.; Li, S. Z.; Xue, C.; Braunschweig, A. B.; Schatz, G. C.; Ratner, M. A.; Mirkin, C. A. *Nano Lett.* **2009,** 9, (12), 3974.
[53]. Ozel, T.; Bourret, G. R.; Mirkin, C. A. *Nat Nanotechnol* **2015,** 10, (4), 319.
[54]. Wen, L. Y.; Wang, Z. J.; Mi, Y.; Xu, R.; Yu, S. H.; Lei, Y. *Small* **2015,** 11, (28), 3408.
[55]. Lee, W.; Park, S.-J. *Chem. Rev.* **2014**.
[56]. O'Sullivan.; P., J.; Wood, G. C. *Proc. R. Soc. London, Ser. A* **1970,** 317, (1531), 511.
[57]. Thompson, G. E.; Xu, Y.; Skeldon, P.; Shimizu, K.; Han, S. H.; Wood, G. C. *Philos Mag B* **1987,** 55, (6), 651.

[58]. Shimizu, K.; Kobayashi, K.; Thompson, G. E.; Wood, G. C. *Philos Mag A* **1992,** 66, (4), 643.
[59]. Thompson, G. E. *Thin Solid Films* **1997,** 297, (1-2), 192.
[60]. Li, F. Y.; Zhang, L.; Metzger, R. M. *Chem. Mater.* **1998,** 10, (9), 2470.
[61]. Albella, J. M.; Montero, I.; Jimenez, M. C.; Martinezduart, J. M. *Electrochim. Acta* **1991,** 36, (3-4), 739.
[62]. Yahalom, J.; Hoar, T. P. *Electrochim. Acta* **1970,** 15, (6), 877.
[63]. Van Overmeere, Q.; Proost, J. *Electrochim. Acta* **2011,** 56, (28), 10507.
[64]. Hoar, T. P.; Mott, N. F. *J. Phys. Chem. Solids* **1959,** 9, (2), 97.
[65]. Garcia-Vergara, S. J.; Skeldon, P.; Thompson, G. E.; Habazaki, H. *Electrochim. Acta* **2006,** 52, (2), 681.
[66]. Skeldon, P.; Thompson, G. E.; Garcia-Vergara, S. J.; Iglesias-Rubianes, L.; Blanco-Pinzon, C. E. *Electrochem Solid St* **2006,** 9, (11), B47.
[67]. Garcia-Vergara, S. J.; Skeldon, P.; Thompson, G. E.; Habakaki, H. *Appl. Surf. Sci.* **2007,** 254, (5), 1534.
[68]. Garcia-Vergara, S. J.; Le Clere, D.; Hashimoto, T.; Habazaki, H.; Skeldon, R.; Thompson, G. E. *Electrochim. Acta* **2009,** 54, (26), 6403.
[69]. Li, A. P.; Muller, F.; Birner, A.; Nielsch, K.; Gosele, U. *J. Appl. Phys.* **1998,** 84, (11), 6023.
[70]. Masuda, H.; Asoh, H.; Watanabe, M.; Nishio, K.; Nakao, M.; Tamamura, T. *Adv. Mater.* **2001,** 13, (3), 189.
[71]. Smith, J. T.; Hang, Q.; Franklin, A. D.; Janes, D. B.; Sands, T. D. *Appl. Phys. Lett.* **2008,** 93, (4).
[72]. Kustandi, T. S.; Loh, W. W.; Gao, H.; Low, H. Y. *Acs Nano* **2010,** 4, (5), 2561.
[73]. Martín, J.; Martín-González, M.; Francisco Fernández, J.; Caballero-Calero, O. *Nat Commun* **2014,** 5.
[74]. Masuda, H.; Fukuda, K. *Science* **1995,** 268, (5216), 1466.
[75]. Masuda, H.; Yamada, H.; Satoh, M.; Asoh, H.; Nakao, M.; Tamamura, T. *Appl. Phys. Lett.* **1997,** 71, (19), 2770.
[76]. Sun, Z. J.; Kim, H. K. *Appl. Phys. Lett.* **2002,** 81, (18), 3458.
[77]. Choi, J.; Nielsch, K.; Reiche, M.; Wehrspohn, R. B.; Gosele, U. *J Vac Sci Technol B* **2003,** 21, (2), 763.
[78]. Lee, W.; Ji, R.; Ross, C. A.; Gosele, U.; Nielsch, K. *Small* **2006,** 2, (8-9), 978.
[79]. Matsui, Y.; Nishio, K.; Masuda, H. *Small* **2006,** 2, (4), 522.
[80]. Kim, B. Y.; Park, S. J.; McCarthy, T. J.; Russell, T. P. *Small* **2007,** 3, (11), 1869.
[81]. Lipson, A. L.; Comstock, D. J.; Hersam, M. C. *Small* **2009,** 5, (24), 2807.
[82]. Noh, K.; Choi, C.; Kim, J. Y.; Oh, Y.; Brammer, K. S.; Loya, M. C.; Jin, S. H. *J Vac Sci Technol B* **2010,** 28, (6), C6m88.
[83]. Mikulskas, I.; Juodkazis, S.; Tomasiunas, R.; Dumas, J. G. *Adv. Mater.* **2001,** 13, (20), 1574.
[84]. Maury, P.; Escalante, M.; Reinhoudt, D. N.; Huskens, J. *Adv. Mater.* **2005,** 17, (22), 2718.
[85]. Guo, L. J. *Adv. Mater.* **2007,** 19, (4), 495.
[86]. Losic, D.; Lillo, M.; Losic, D. *Small* **2009,** 5, (12), 1392.
[87]. Fu, Q.; Zhan, Z.; Dou, J.; Zheng, X.; Xu, R.; Wu, M.; Lei, Y. *Acs Appl Mater Inter* **2015,** 7, (24), 13322.
[88]. Wu, M. H.; Wen, L. Y.; Lei, Y.; Ostendorp, S.; Chen, K.; Wilde, G. *Small* **2010,** 6, (5), 695.
[89]. Lei, Y.; Chim, W. K.; Sun, H. P.; Wilde, G. *Appl. Phys. Lett.* **2005,** 86, (10), 103106.

[90]. Grote, F.; Kuhnel, R. S.; Balducci, A.; Lei, Y. *Appl. Phys. Lett.* **2014,** 104, (5), 053904.
[91]. Zhang, Z.; Shimizu, T.; Senz, S.; Gosele, U. *Adv. Mater.* **2009,** 21, (27), 2824.
[92]. Zhang, Y.; Li, G. H.; Wu, Y. C.; Zhang, B.; Song, W. H.; Zhang, L. *Adv. Mater.* **2002,** 14, (17), 1227.
[93]. Lee, W.; Kim, J. C. *Nanotechnology* **2010,** 21, (48), 485304.
[94]. Nicewarner-Pena, S. R.; Freeman, R. G.; Reiss, B. D.; He, L.; Pena, D. J.; Walton, I. D.; Cromer, R.; Keating, C. D.; Natan, M. J. *Science* **2001,** 294, (5540), 137.
[95]. Kovtyukhova, N. I.; Mallouk, T. E. *Chem-Eur J* **2002,** 8, (19), 4355.
[96]. Wang, J. G.; Tian, M. L.; Kumar, N.; Mallouk, T. E. *Nano Lett.* **2005,** 5, (7), 1247.
[97]. Winkler, N.; Leuthold, J.; Lei, Y.; Wilde, G. *J. Mater. Chem.* **2012,** 22, (32), 16627.
[98]. Lei, Y.; Yeong, K. S.; Thong, J. T. L.; Chim, W. K. *Chem. Mater.* **2004,** 16, (14), 2757.
[99]. Lee, W.; Scholz, R.; Niesch, K.; Gosele, U. *Angew Chem Int Edit* **2005,** 44, (37), 6050.
[100]. Al-Haddad, A.; Wang, Z. J.; Xu, R.; Qi, H. Y.; Vellacheri, R.; Kaiser, U.; Lei, Y. *J. Phys. Chem. C* **2015,** 119, (28), 16331.
[101]. Grote, F.; Zhao, H. P.; Lei, Y. *J. Mater. Chem. A* **2015,** 3, (7), 3465.
[102]. Tarish, S.; Wang, Z. J.; Al-Haddad, A.; Wang, C. L.; Ispas, A.; Romanus, H.; Schaaf, P.; Lei, Y. *J. Phys. Chem. C* **2015,** 119, (3), 1575.
[103]. Grote, F.; Lei, Y. *Nano Energy* **2014,** 10, 63.
[104]. Grote, F.; Wen, L. Y.; Lei, Y. *J. Power Sources* **2014,** 256, 37.
[105]. Lei, Y.; Chim, W. K.; Zhang, Z. P.; Zhou, T. J.; Zhang, L. D.; Meng, G. W.; Phillipp, F. *Chem. Phys. Lett.* **2003,** 380, (3-4), 313.
[106]. Zhao, H. P.; Wang, C. L.; Vellacheri, R.; Zhou, M.; Xu, Y.; Fu, Q.; Wu, M. H.; Grote, F. B.; Lei, Y. *Adv. Mater.* **2014,** 26, (45), 7654.
[107]. Wen, L.; Wang, Z.; Mi, Y.; Xu, R.; Yu, S.-H.; Lei, Y. *Small* **2015,** 11, (28), 3408.
[108]. Price, M. J.; Maldonado, S. *J Phys Chem C* **2009,** 113, (28), 11988.
[109]. Foley, J. M.; Price, M. J.; Feldblyum, J. I.; Maldonado, S. *Energy Environ. Sci.* **2012,** 5, (1), 5203.
[110]. Foley, J. M.; Price, M. J.; Feldblyum, J. I.; Maldonado, S. *Energy Environ. Sci.* **2012,** 5, (12), 9946.
[111]. Long, J. W.; Dunn, B.; Rolison, D. R.; White, H. S. *Chem. Rev.* **2004,** 104, (10), 4463.
[112]. Hart, R. W.; White, H. S.; Dunn, B.; Rolison, D. R. *Electrochem. Commun.* **2003,** 5, (2), 120.
[113]. Brongersma, M. L.; Cui, Y.; Fan, S. H. *Nat. Mater.* **2014,** 13, (5), 451.
[114]. Kapadia, R.; Fan, Z. Y.; Javey, A. *Appl. Phys. Lett.* **2010,** 96, (10), 103116.
[115]. Liu, P. A.; Singh, V. P.; Jarro, C. A.; Rajaputra, S. *Nanotechnology* **2011,** 22, (14), 145304.
[116]. Dang, H.; Singh, V.; Rajaputra, S.; Guduru, S.; Chen, J.; Nadimpally, B. *Sol. Energy Mater. Sol. Cells* **2014,** 126, (0), 184.
[117]. Lin, Q. F.; Leung, S. F.; Lu, L. F.; Chen, X. Y.; Chen, Z.; Tang, H. N.; Su, W. J.; Li, D. D.; Fan, Z. Y. *Acs Nano* **2014,** 8, (6), 6484.
[118]. Kuo, C. Y.; Tang, W. C.; Gau, C.; Guo, T. F.; Jeng, D. Z. *Appl. Phys. Lett.* **2008,** 93, (3), 033307.
[119]. Lee, J.; Jho, J. Y. *Sol. Energy Mater. Sol. Cells* **2011,** 95, (11), 3152.
[120]. Foong, T. R. B.; Shen, Y. D.; Hu, X.; Sellinger, A. *Adv. Funct. Mater.* **2010,** 20, (9), 1390.
[121]. Kang, Y. M.; Park, N. G.; Kim, D. *Appl. Phys. Lett.* **2005,** 86, (11), 113101.

[122]. Schierhorn, M.; Boettcher, S. W.; Peet, J. H.; Matioli, E.; Bazan, G. C.; Stucky, G. D.; Moskovits, M. *Acs Nano* **2010,** 4, (10), 6132.
[123]. Lee, J.; Mubeen, S.; Hernandez-Sosa, G.; Sun, Y. M.; Toma, F. M.; Stucky, G. D.; Moskovits, M. *Adv. Mater.* **2013,** 25, (2), 256.
[124]. Kim, J. S.; Park, Y.; Lee, D. Y.; Lee, J. H.; Park, J. H.; Kim, J. K.; Cho, K. *Adv. Funct. Mater.* **2010,** 20, (4), 540.
[125]. Chang, C. Y.; Wu, C. E.; Chen, S. Y.; Cui, C. H.; Cheng, Y. J.; Hsu, C. S.; Wang, Y. L.; Li, Y. F. *Angew Chem Int Edit* **2011,** 50, (40), 9386.
[126]. Chen, D.; Zhao, W.; Russell, T. P. *Acs Nano* **2012,** 6, (2), 1479.
[127]. Wang, H. S.; Lin, L. H.; Chen, S. Y.; Wang, Y. L.; Wei, K. H. *Nanotechnology* **2009,** 20, (7), 075201.
[128]. Wang, H. S.; Chen, S. Y.; Su, M. H.; Wang, Y. L.; Wei, K. H. *Nanotechnology* **2010,** 21, (14), 145203.
[129]. Martinson, A. B. F.; Elam, J. W.; Liu, J.; Pellin, M. J.; Marks, T. J.; Hupp, J. T. *Nano Lett.* **2008,** 8, (9), 2862.
[130]. Sahu, G.; Gordon, S. W.; Tarr, M. A. *Rsc Adv* **2012,** 2, (2), 573.
[131]. Maijenburg, A. W.; Veerbeek, J.; de Putter, R.; Veldhuis, S. A.; Zoontjes, M. G. C.; Mul, G.; Montero-Moreno, J. M.; Nielsch, K.; Schafer, H.; Steinhart, M.; ten Elshof, J. E. *J Mater Chem A* **2014,** 2, (8), 2648.
[132]. Lee, J.; Mubeen, S.; Ji, X. L.; Stucky, G. D.; Moskovits, M. *Nano Lett.* **2012,** 12, (9), 5014.
[133]. Qiu, Y. C.; Leung, S. F.; Zhang, Q. P.; Hua, B.; Lin, Q. F.; Wei, Z. H.; Tsui, K. H.; Zhang, Y. G.; Yang, S. H.; Fan, Z. Y. *Nano Lett.* **2014,** 14, (4), 2123.
[134]. Huang, L.; Chen, D.; Ding, Y.; Feng, S.; Wang, Z. L.; Liu, M. *Nano Lett.* **2013,** 13, (7), 3135.
[135]. Guo, Y. B.; Tang, Q. X.; Liu, H. B.; Zhang, Y. J.; Li, Y. L.; Hu, W. P.; Wang, S.; Zhu, D. B. *J. Am. Chem. Soc.* **2008,** 130, (29), 9198.
[136]. Guo, Y. B.; Zhang, Y. J.; Liu, H. B.; Lai, S. W.; Li, Y. L.; Li, Y. J.; Hu, W. P.; Wang, S.; Che, C. M.; Zhu, D. B. *J. Phys. Chem. Lett.* **2010,** 1, (1), 327.
[137]. Yoo, S. H.; Liu, L. C.; Ku, T. W.; Hong, S.; Whang, D.; Park, S. *Appl. Phys. Lett.* **2013,** 103, (14), 143101.
[138]. Kim, K.; Lee, J. W.; Lee, S. H.; Lee, Y. B.; Cho, E. H.; Noh, H. S.; Jo, S. G.; Joo, J. *Org. Electron.* **2011,** 12, (10), 1695.
[139]. Ozel, T.; Bourret, G. R.; Schmucker, A. L.; Brown, K. A.; Mirkin, C. A. *Adv. Mater.* **2013,** 25, (32), 4515.
[140]. Mubeen, S.; Singh, N.; Lee, J.; Stucky, G. D.; Moskovits, M.; McFarland, E. W. *Nano Lett.* **2013,** 13, (5), 2110.
[141]. Wang, X. T.; Liow, C.; Qi, D. P.; Zhu, B. W.; Leow, W. R.; Wang, H.; Xue, C.; Chen, X. D.; Li, S. Z. *Adv. Mater.* **2014,** 26, (21), 3506.
[142]. Wang, G. P.; Zhang, L.; Zhang, J. J. *Chem. Soc. Rev.* **2012,** 41, (2), 797.
[143]. Zheng, J. P.; Jow, T. R. *J. Electrochem. Soc.* **1995,** 142, (1), L6.
[144]. Soudan, P.; Gaudet, J.; Guay, D.; Belanger, D.; Schulz, R. *Chem. Mater.* **2002,** 14, (3), 1210.
[145]. Lin, C.; Ritter, J. A.; Popov, B. N. *J. Electrochem. Soc.* **1998,** 145, (12), 4097.
[146]. Brousse, T.; Toupin, M.; Belanger, D. *J. Electrochem. Soc.* **2004,** 151, (4), A614.
[147]. Takahashi, K.; Wang, Y.; Cao, G. Z. *J. Phys. Chem. B* **2005,** 109, (1), 48.
[148]. Liu, R.; Lee, S. B. *J. Am. Chem. Soc.* **2008,** 130, (10), 2942.
[149]. Liu, R.; Duay, J.; Lee, S. B. *Acs Nano* **2010,** 4, (7), 4299.
[150]. Liu, R.; Duay, J.; Lee, S. B. *ACS Nano* **2011,** 5, (7), 5608.

[151]. Liu, R.; Duay, J.; Lane, T.; Lee, S. B. *PCCP* **2010,** 12, (17), 4309.
[152]. Ponrouch, A.; Garbarino, S.; Bertin, E.; Guay, D. *J. Power Sources* **2013,** 221, 228.
[153]. Reddy, A. L. M.; Shaijumon, M. M.; Gowda, S. R.; Ajayan, P. M. *J Phys Chem C* **2010,** 114, (1), 658.
[154]. Sherrill, S. A.; Duay, J.; Gui, Z.; Banerjee, P.; Rubloff, G. W.; Lee, S. B. *PCCP* **2011,** 13, (33), 15221.
[155]. Kim, J. Y.; Lee, S. H.; Yan, Y. F.; Oh, J.; Zhu, K. *Rsc Adv* **2012,** 2, (22), 8281.
[156]. Zhao, H.; Wang, C.; Vellacheri, R.; Zhou, M.; Xu, Y.; Fu, Q.; Wu, M.; Grote, F.; Lei, Y. *Adv. Mater.* **2014,** 26, (45), 7654.
[157]. Shelimov, K. B.; Davydov, D. N.; Moskovits, M. *Appl. Phys. Lett.* **2000,** 77, (11), 1722.
[158]. Sohn, J. I.; Kim, Y. S.; Nam, C.; Cho, B. K.; Seong, T. Y.; Lee, S. *Appl. Phys. Lett.* **2005,** 87, (12), 123115.
[159]. Haspert, L. C.; Lee, S. B.; Rubloff, G. W. *Acs Nano* **2012,** 6, (4), 3528.
[160]. George, S. M. *Chem. Rev.* **2010,** 110, (1), 111.
[161]. Johnson, R. W.; Hultqvist, A.; Bent, S. F. *Mater. Today* **2014,** 17, (5), 236.
[162]. Miikkulainen, V.; Leskela, M.; Ritala, M.; Puurunen, R. L. *J. Appl. Phys.* **2013,** 113, (2).
[163]. Wen, L. Y.; Mi, Y.; Wang, C. L.; Fang, Y. G.; Grote, F.; Zhao, H. P.; Zhou, M.; Lei, Y. *Small* **2014,** 10, (15), 3162.
[164]. Penner, R. M. *J Phys Chem C* **2014,** 118, (31), 17179.
[165]. https://en.wikipedia.org/wiki/Electron_beam_physical_vapor_deposition
[166]. https://en.wikipedia.org/wiki/Electron-beam_lithography
[167]. Altissimo, M. *Biomicrofluidics* **2010,** 4, (2), 026503.
[168]. http://www.ionbeammilling.com/about_the_ion_milling_process
[169]. https://en.wikipedia.org/wiki/Scanning_electron_microscope.
[170]. https://en.wikipedia.org/wiki/Scanning_electron_microscope
[171]. https://en.wikipedia.org/wiki/Transmission_electron_microscopy
[172]. https://en.wikipedia.org/wiki/Potentiostat
[173]. https://en.wikipedia.org/wiki/Ultraviolet%E2%80%93visible_spectroscopy
[174]. https://en.wikipedia.org/wiki/Time-resolved_spectroscopy
[175]. Han, H.; Park, S. J.; Jang, J. S.; Ryu, H.; Kim, K. J.; Baik, S.; Lee, W. *Acs Appl Mater Inter* **2013,** 5, (8), 3441.
[176]. Thompson, G. E.; Wood, G. C. *Nature* **1981,** 290, (5803), 230.
[177]. Asoh, H.; Ono, S.; Hirose, T.; Nakao, M.; Masuda, H. *Electrochim. Acta* **2003,** 48, (20-22), 3171.
[178]. Choi, J.; Wehrspohn, R. B.; Gosele, U. *Electrochim. Acta* **2005,** 50, (13), 2591.
[179]. Masuda, H.; Abe, A.; Nakao, M.; Yokoo, A.; Tamamura, T.; Nishio, K. *Adv. Mater.* **2003,** 15, (2), 161.
[180]. Asoh, H.; Ono, S.; Hirose, T.; Takatori, I.; Masuda, H. *Japanese Journal of Applied Physics Part 1-Regular Papers Short Notes & Review Papers* **2004,** 43, (9A), 6342.
[181]. Lee, W.; Ji, R.; Ross, C. A.; Gösele, U.; Nielsch, K. *Small* **2006,** 2, (8-9), 978.
[182]. Smith, J. T.; Hang, Q.; Franklin, A. D.; Janes, D. B.; Sands, T. D. *Appl. Phys. Lett.* **2008,** 93, (4).
[183]. Chen, S. H.; Chan, D. S.; Chen, C. K.; Chang, T. H.; Lai, Y. H.; Lee, C. C. *Jpn J Appl Phys* **2010,** 49, (1).
[184]. Yang, J.; Huang, H. T.; Lin, Q. F.; Lu, L. F.; Chen, X. Y.; Yang, L. Y.; Zhu, X. F.; Fan, Z. Y.; Song, Y.; Li, D. D. *Acs Appl Mater Inter* **2014,** 6, (4), 2285.
[185]. Oh, J.; Thompson, C. V. *Electrochim. Acta* **2011,** 56, (11), 4044.

[186]. Nozik, A. J. *Appl. Phys. Lett.* **1976,** 29, (3), 150.
[187]. Tada, H.; Mitsui, T.; Kiyonaga, T.; Akita, T.; Tanaka, K. *Nat. Mater.* **2006,** 5, (10), 782.
[188]. Liu, C.; Tang, J. Y.; Chen, H. M.; Liu, B.; Yang, P. D. *Nano Lett.* **2013,** 13, (6), 2989.
[189]. Franklin, A. D.; Koswatta, S. O.; Farmer, D. B.; Smith, J. T.; Gignac, L.; Breslin, C. M.; Han, S.-J.; Tulevski, G. S.; Miyazoe, H.; Haensch, W.; Tersoff, J. *Nano Lett.* **2013,** 13, (6), 2490.
[190]. Vlad, A.; Dutu, C. A.; Jedrasik, P.; Sodervall, U.; Gohy, J. F.; Melinte, S. *Nanotechnology* **2012,** 23, (2).
[191]. Thelander, C.; Rehnstedt, C.; Froberg, L. E.; Lind, E.; Martensson, T.; Caroff, P.; Lowgren, T.; Ohlsson, B. J.; Samuelson, L.; Wernersson, L. E. *Ieee Transactions on Electron Devices* **2008,** 55, (11), 3030.
[192]. Ng, H. T.; Han, J.; Yamada, T.; Nguyen, P.; Chen, Y. P.; Meyyappan, M. *Nano Lett.* **2004,** 4, (7), 1247.
[193]. Hu, C. C.; Chang, K. H.; Lin, M. C.; Wu, Y. T. *Nano Lett.* **2006,** 6, (12), 2690.
[194]. Wang, H. L.; Liang, Y. Y.; Mirfakhrai, T.; Chen, Z.; Casalongue, H. S.; Dai, H. J. *Nano Res* **2011,** 4, (8), 729.
[195]. Subramanian, V.; Hall, S. C.; Smith, P. H.; Rambabu, B. *Solid State Ionics* **2004,** 175, (1-4), 511.
[196]. Bi, R. R.; Wu, X. L.; Cao, F. F.; Jiang, L. Y.; Guo, Y. G.; Wan, L. J. *J. Phys. Chem. C* **2010,** 114, (6), 2448.
[197]. Kuratani, K.; Tatsumi, K.; Kuriyama, N. *Cryst Growth Des* **2007,** 7, (8), 1375.
[198]. Xu, M.; Kong, L.; Zhou, W.; Li, H. *J. Phys. Chem. C* **2007,** 111, (51), 19141.
[199]. Yu, P.; Zhang, X.; Wang, D. L.; Wang, L.; Ma, Y. W. *Cryst Growth Des* **2009,** 9, (1), 528.
[200]. Jiang, H.; Zhao, T.; Ma, J.; Yan, C. Y.; Li, C. Z. *Chem. Commun.* **2011,** 47, (4), 1264.
[201]. Xiao, W.; Xia, H.; Fuh, J. Y. H.; Lu, L. *J. Power Sources* **2009,** 193, (2), 935.
[202]. Luo, J.; Zhu, H. T.; Fan, H. M.; Liang, J. K.; Shi, H. L.; Rao, G. H.; Li, J. B.; Du, Z. M.; Shen, Z. X. *J. Phys. Chem. C* **2008,** 112, (33), 12594.
[203]. Chen, S.; Zhu, J. W.; Wu, X. D.; Han, Q. F.; Wang, X. *ACS Nano* **2010,** 4, (5), 2822.
[204]. Xie, X. Y.; Zhang, C.; Wu, M. B.; Tao, Y.; Lv, W.; Yang, Q. H. *Chem. Commun.* **2013,** 49, (94), 11092.
[205]. Simon, P.; Gogotsi, Y. *Nat Mater* **2008,** 7, (11), 845.
[206]. Lang, X. Y.; Hirata, A.; Fujita, T.; Chen, M. W. *Nat Nanotechnol* **2011,** 6, (4), 232.
[207]. Yan, W. B.; Kim, J. Y.; Xing, W. D.; Donavan, K. C.; Ayvazian, T.; Penner, R. M. *Chem. Mater.* **2012,** 24, (12), 2382.
[208]. Yu, Z. N.; Duong, B.; Abbitt, D.; Thomas, J. *Adv. Mater.* **2013,** 25, (24), 3302.
[209]. Walter, M. G.; Warren, E. L.; McKone, J. R.; Boettcher, S. W.; Mi, Q. X.; Santori, E. A.; Lewis, N. S. *Chem. Rev.* **2010,** 110, (11), 6446.
[210]. Gomes Silva, C.; Juárez, R.; Marino, T.; Molinari, R.; García, H. *J. Am. Chem. Soc.* **2011,** 133, (3), 595.
[211]. Liu, Z. W.; Hou, W. B.; Pavaskar, P.; Aykol, M.; Cronin, S. B. *Nano Lett.* **2011,** 11, (3), 1111.
[212]. Tian, Y.; Tatsuma, T. *J. Am. Chem. Soc.* **2005,** 127, (20), 7632.
[213]. Furube, A.; Du, L.; Hara, K.; Katoh, R.; Tachiya, M. *J. Am. Chem. Soc.* **2007,** 129, (48), 14852.
[214]. Mubeen, S.; Hernandez-Sosa, G.; Moses, D.; Lee, J.; Moskovits, M. *Nano Lett.* **2011,** 11, (12), 5548.

[215]. Seh, Z. W.; Liu, S. H.; Low, M.; Zhang, S. Y.; Liu, Z. L.; Mlayah, A.; Han, M. Y. *Adv. Mater.* **2012,** 24, (17), 2310.
[216]. Liu, L. Q.; Ouyang, S. X.; Ye, J. H. *Angew Chem Int Edit* **2013,** 52, (26), 6689.
[217]. Pu, Y. C.; Wang, G. M.; Chang, K. D.; Ling, Y. C.; Lin, Y. K.; Fitzmorris, B. C.; Liu, C. M.; Lu, X. H.; Tong, Y. X.; Zhang, J. Z.; Hsu, Y. J.; Li, Y. *Nano Lett.* **2013,** 13, (8), 3817.
[218]. Ding, D. W.; Liu, K.; He, S. N.; Gao, C. B.; Yin, Y. D. *Nano Lett.* **2014,** 14, (11), 6731.
[219]. Zhang, X.; Liu, Y.; Lee, S. T.; Yang, S. H.; Kang, Z. H. *Energy Environ. Sci.* **2014,** 7, (4), 1409.
[220]. Linic, S.; Christopher, P.; Ingram, D. B. *Nat Mater* **2011,** 10, (12), 911.
[221]. Thomann, I.; Pinaud, B. A.; Chen, Z. B.; Clemens, B. M.; Jaramillo, T. F.; Brongersma, M. L. *Nano Lett.* **2011,** 11, (8), 3440.
[222]. Hou, W. B.; Cronin, S. B. *Adv. Funct. Mater.* **2013,** 23, (13), 1612.
[223]. Zheng, F. G.; Xu, J.; Fang, L.; Shen, M. R.; Wu, X. L. *Appl. Phys. Lett.* **2008,** 93, (17).
[224]. Qin, M.; Yao, K.; Liang, Y. C. *Appl. Phys. Lett.* **2008,** 93, (12).
[225]. Qin, M.; Yao, K.; Liang, Y. C.; Gan, B. K. *Appl. Phys. Lett.* **2007,** 91, (9).
[226]. Cao, D. W.; Wang, C. Y.; Zheng, F. G.; Dong, W.; Fang, L.; Shen, M. R. *Nano Lett.* **2012,** 12, (6), 2803.
[227]. Zhang, P.; Cao, D. W.; Wang, C. Y.; Shen, M. R.; Su, X. D.; Fang, L.; Dong, W.; Zheng, F. G. *Mater. Chem. Phys.* **2012,** 135, (2-3), 304.
[228]. Park, Y.; Choong, V.; Gao, Y.; Hsieh, B. R.; Tang, C. W. *Appl. Phys. Lett.* **1996,** 68, (19), 2699.
[229]. Yang, X. L.; Su, X. D.; Shen, M. R.; Zheng, F. G.; Xin, Y.; Zhang, L.; Hua, M. C.; Chen, Y. J.; Harris, V. G. *Adv. Mater.* **2012,** 24, (9), 1202.
[230]. Cao, D. W.; Wang, C. Y.; Zheng, F. G.; Fang, L.; Dong, W.; Shen, M. R. *J. Mater. Chem.* **2012,** 22, (25), 12592.
[231]. Cao, D. W.; Wang, Z. J.; Nasori; Wen, L. Y.; Mi, Y.; Lei, Y. *Angew Chem Int Edit* **2014,** 53, (41), 11027.
[232]. Choi, T.; Lee, S.; Choi, Y. J.; Kiryukhin, V.; Cheong, S. W. *Science* **2009,** 324, (5923), 63.
[233]. Voisin, C.; Del Fatti, N.; Christofilos, D.; Vallee, F. *J. Phys. Chem. B* **2001,** 105, (12), 2264.
[234]. Link, S.; El-Sayed, M. A. *J. Phys. Chem. B* **1999,** 103, (40), 8410.
[235]. Sun, C. K.; Vallee, F.; Acioli, L. H.; Ippen, E. P.; Fujimoto, J. G. *Phys Rev B* **1994,** 50, (20), 15337.
[236]. Demsar, J.; Kabanov, V. V.; Alexandrov, A. S.; Lee, H. J.; Bauer, E. D.; Sarrao, J. L.; Taylor, A. J. *Phys Rev B* **2009,** 80, (8).

Extended works

Besides the works shown in this dissertation, I also proficiently collaborated with my colleagues in other topics related to PEC and Batteries. The abstracts and the table of content figures of the respective papers are presented in this section to highlight the achieved results beyond the scope of this dissertation.

1. **Constructing well-defined AZO/TiO_2 core/shell nanocones with uniformly dispersed Au NPs for enhancing photoelectrochemical water splitting (with Yan Mi)**

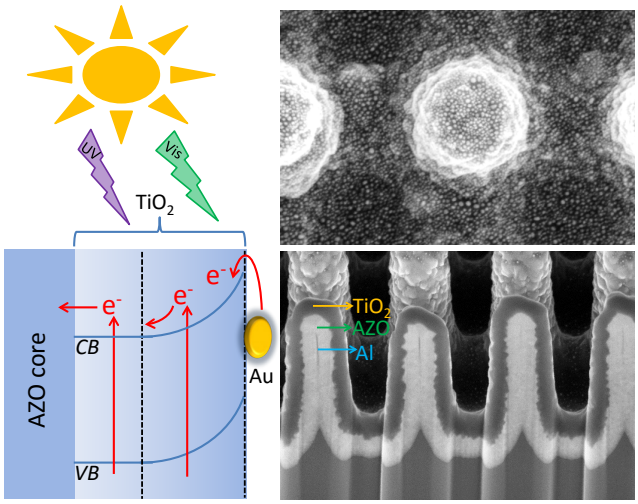

Constructing core/shell nanostructures with optimal structure and composition could maximize the solar light utilization. In this work, using an Al nanocone array as a substrate, well-defined regular array of AZO/TiO_2 core/shell nanocones with uniformly dispersed Au nanoparticles (AZO/TiO_2/Au NCA) is successfully realized through three sequential steps of atomic layer deposition, physical vapor deposition and annealing processes. By tuning the structural and compositional parameters, the advantages of light trapping and short carrier diffusion from the core/shell nanocone array, as well as the surface plasmon resonance and catalytic effects from the Au NPs can be maximally utilized. Accordingly, a remarkable PEC performance could be acquired and the photocurrent density of the AZO/TiO_2/Au NCA electrode reaches up to 1.1 mA/cm^2 at 1.23 V versus RHE under simulated sunlight illumination, which is five times of that from flat AZO/TiO_2 electrode (0.22 mA/cm^2). Moreover, the photoconversion of the AZO/TiO_2/Au NCA electrode approaches to 0.73% at 0.21 V versus RHE, which is one of the highest values with the lowest external potential that ever reported in Au/TiO_2 PEC composites. These results demonstrate a feasible route toward scalable fabrication of well-modulated core/shell nanostructures and can be easily applied to other metal/semiconductor composites for high-performance PEC electrodes *(Advanced Energy Material, accepted).*

2. Building of Anti-Restack 3D BiOCl Hierarchitecture by Ultrathin Nanosheets towards Enhanced Photocatalytic Activity (with Yan Mi)

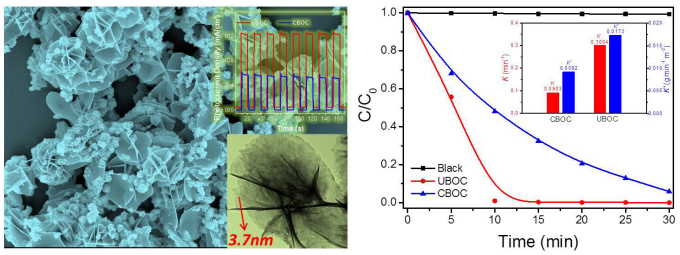

A characteristic anti-restack 3D BiOCl hierarchitecture constructed by ultrathin BiOCl nanosheets assembled substructures has been designed and synthesized via a facile hydrothermal route. The graphene-like ultrathin BiOCl nanosheets with thickness of about 3.7 nm expose the renowned energetically active (0 0 1) facet, enabling the fast separation and transport of photogenerated electron–hole pairs. Meanwhile, the multi-reflection of light and large surface area of the formed 3D nano-velvet substructures enhance the light harvest and molecule adsorption capability. Consequently, the resultants show a superior photocatalytic performance of 99% photodegradation and corresponding 74% mineralization for rhodamine B within 10 min, and an outstanding photocurrent response under solar light illumination. What is more, the unique microstructure efficiently overcomes the restack of ultrathin nanosheets. This work develops a feasible strategy that utilizes ultrathin nanosheets to design and synthesize anti-restack hierarchitectures for establishing efficacious photocatalytic and water splitting systems (*Applied Catalysis B: Environmental, 176, 331–337, 2015*).

3. Highly Ordered Three-Dimensional Ni-TiO_2 Nanoarrays as Sodium Ion Battery Anodes (with Dr. Yang Xu)

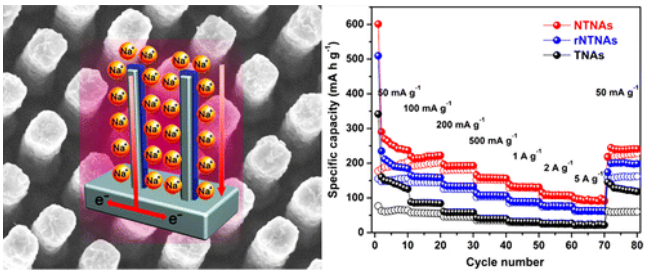

Sodium ion batteries (SIBs) represent an effective energy storage technology with potentially lower material costs than lithium ion batteries. Here, we show that the electrochemical performance of SIBs, especially rate capability, is intimately connected to the electrode design at the nanoscale by taking anatase TiO2 as an example. Highly ordered three-dimensional (3D) Ni-TiO_2 core–shell nanoarrays were fabricated using nanoimprited AAO templating technique and directly used as anode. The nanoarrays delivered a reversible capacity of ~200 mAh g^{-1} after 100 cycles at the current density of 50 mAh g^{-1} and were able to retain a capacity of ~95 mAh g^{-1} at the current density as

high as 5 A g^{-1} and fully recover low rate capacity. High ion accessibility, fast electron transport, and excellent electrode integrity were shown as great merits to obtain the presented electrochemical performance. Our work demonstrates the possibility of highly ordered 3D heterostructured nanoarrays as a promising electrode design for Na energy storage to alleviate the reliance on the materials' intrinsic nature and provides a versatile and cost-effective technique for the fabrication of such perfectly ordered nanostructures *(Chemical Material, 27, 4274–4280, 2015).*

4. Large-scale Highly Ordered Sb Nanorod Arrays Anode with High Capacity and Rate Capability for Sodium-Ion Batteries (with Liying Liang)

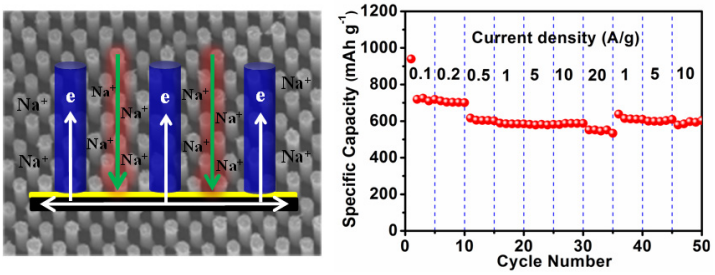

Na-ion batteries are a potential substitute to Li-ion batteries for energy storage devices. However, their poor electrochemical performance, especially capacity and rate capability, is the major bottleneck to future development. Here we propose a performance-oriented electrode structure, which is 1D nanostructure arrays with large-scale high ordering, good vertical alignment, and large interval spacing. Benefiting from these structural merits, a great enhancement in electrochemical performance could be achieved. Taking Sb as an example, we firstly report large-scale highly ordered Sb nanorod arrays with uniform large interval spacing (190 nm). In return for this electrode design, high ion accessibility, fast electron transport, and strong electrode integrity are presented here. Used as additive- and binder-free anodes for Na-ion batteries, Sb nanorod arrays showed a high capacity of 620 mA h g^{-1} at the 100th cycle with a retention of 84% up to 250 cycles at 0.2 A g^{-1}, and a superior rate capability for delivering reversible capacities of 579.7 and 557.7 mA h g^{-1} at 10 and 20 A g^{-1}, respectively. A full cell coupled by a P2-Na2/3Ni1/3Mn2/3O2 cathode and a Sb nanorod array anode was also constructed, which showed good cycle performance up to 250 cycles, high rate capability up to 20 A g^{-1}, and large energy density up to 130 Wh kg^{-1}. These excellent electrochemical performances shall pave the way for developing more applications of Sb nanorod arrays in energy storage devices *(Energy & Environmental Science, DOI: 10.1039/C5EE00878F, 2015).*

5. Template-directed construction of nanostructure arrays for highly-efficient energy storage and conversion (with Dr. Huaping Zhao)

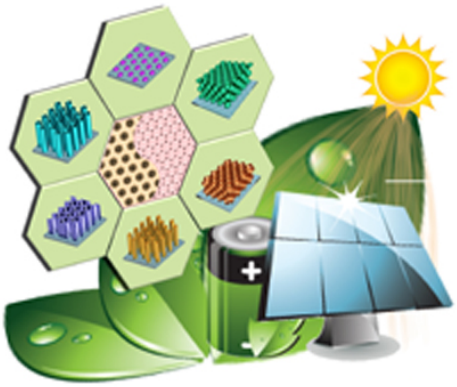

To ensure the future highly efficient utilization of various sustainable and renewable energy sources, nanostructured electrodes have become more and more important. This review provides a comprehensive summary of recent research progress in template-directed synthesis of nanostructured arrays for highly-efficient energy storage and conversion. We especially focus on nanostructure arrays based on porous anodic aluminum oxide (AAO) template and colloidal crystal template (CCT), because they possess numerous structural advantages resulting from the highly-ordered and highly-oriented structural features of AAO and CCT, such as nanoscale structural tunability, high regularity and predefined spatial orientation/alignment. All these advantages make AAO and CCT template-directed nanostructure arrays as attractive candidates for highly-efficient energy storage and conversion. This review starts with a brief introduction on template-directed construction of nanostructure arrays, including the fabrication and structural features of both the templates (AAO and CCT) and the corresponding as-achieved nanostructure arrays. Then, the advantages, the progress and the challenges of AAO and CCT template-directed nanostructure arrays for the construction of highly-efficient electrochemical energy storage and solar energy conversion devices are summarized, respectively, followed by present status and the prospects for future research *(Nano Energy, 13, 790-813, 2015).*

6. Switchable Charge-Transfer in the Photoelectrochemical Energy-Conversion Process of Ferroelectric $BiFeO_3$ Photoelectrodes (With Dr. Dawei Cao)

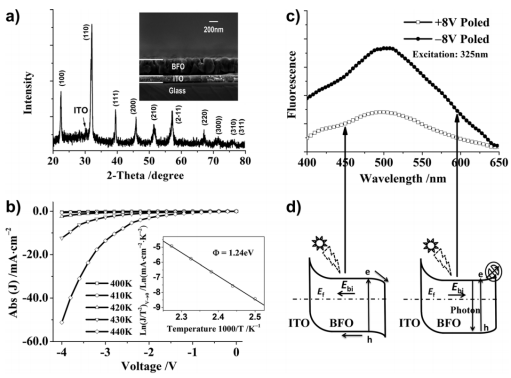

Instead of conventional semiconductor photoelectrodes, herein, we focus on BiFeO3 ferroelectric photoelectrodes to break the limits imposed by common semiconductors. As a result of their prominent ferroelectric properties, the photoelectrodes are able to tune the transfer of photo-excited charges generated either in

BiFeO3 or the surface modifiers by manipulating the poling conditions of the ferroelectric domains. At 0 V vs Ag/AgCl, the photocurrent could be switched from 0 $\mu A\,cm^{-2}$ to $10\mu A\,cm^{-2}$ and the open-circuit potential changes from 33 mV to 440 mV, when the poling bias of pretreatment is manipulated from −8 V to +8 V. Additionally, the pronounced photocurrent from charge injection of the excited surface modifiers could be quenched by switching the poling bias from +8 V to −8 V (*Angewandte Chemie International Edition, 126, 11207-11211, 2014*).

Scientific contributions

In total I have published and jointly published 16 papers in SCI-indexed international scientific journals during the period of my Ph.D., including 9 papers with impact factor higher than 8 (Small, Nano Energy, Chemistry of Materials, Energy & Environmental Science, Angewandte Chemie International Edition, ACS Nano) and 7 papers with impact factor between 3 and 8 (Applied Catalysis B: Environmental, Nanoscale, Chemistry - A European Journal, Dalton Transactions, Catalysis Today, Journal of Power Sources, Journal of Materials Chemistry C). The published papers were cited for more than 290 times during my PhD (Source: google scholar database).

I also gave 11 contributions at conferences, including 2 conference proceedings, 8 talks and 2 posters.

Cover stories

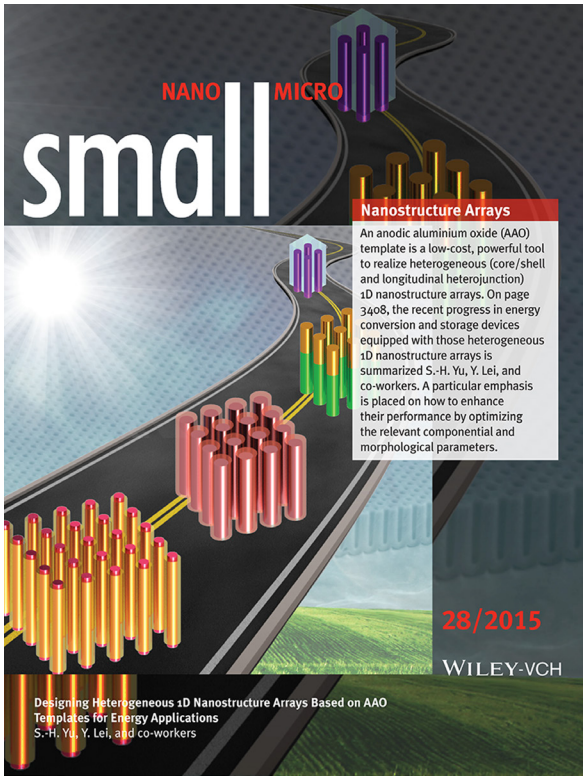

The paper 'Designing heterogeneous one-dimensional nanostructure arrays based on AAO template for energy applications' by Wen L.Y. and Lei.Y. was selected as the frontispiece.

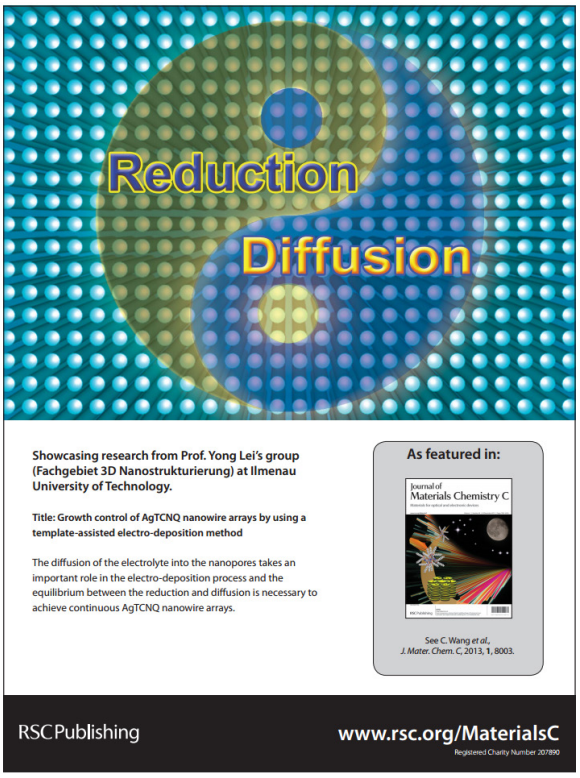

The paper 'Growth control of AgTCNQ nanowire arrays by using a template-assisted electro-deposition method' by Wang C.L., Wen L.Y. and Lei.Y. was selected as the Backside cover.

Publications in SCI-indexed Scientific Journals

1. Yan M.,[+] Wen L.Y.,[+] Xu R., Wang Z.J., Cao D.W., Fang Y.G., Lei Y.*, 'Constructing well-defined regular array of AZO/TiO_2 core/shell nanocones with uniformly dispersed Au NPs for enhancing photoelectrochemical water splitting', **Advanced Energy Material**. (impact factor 16.146), 6, 1501496, 2016 ([+]contributed equally).
2. Wang Z.J., Cao D.W., Wen L.Y., Xu R., Manuel O., Mi Y., Zhan Z.B., Nasori N., Demsar J., and Lei Y.*, 'Manipulation of charge transfer and transport in plasmonic-ferroelectric hybrids for photoelectrochemical applications', **Nature Communication** (impact factor 11.470), in press, (DOI: 10.1038/ncomms10348), 2016.
3. Wen L.Y., Wang Z.J., Yan M., Xu R., Yu S.H.*, Lei Y.*, 'Designing heterogeneous one-dimensional nanostructure arrays based on AAO template for energy applications', **Small** (IF 8.368), 11, 3408–3428, 2015 (was selected as the frontispiece).
4. Mi Y., Wen L.Y., Wang Z.J., Cao D.W., Fang Y.G., Lei Y. *,'Building of Anti-Restack 3D BiOCl Hierarchitecture by Ultrathin Nanosheets towards Enhanced Photocatalytic Activity', **Applied Catalysis B: Environmental** (IF 7.435), 176, 331-337, 2015.
5. Xu Y., Zhou M., Wen L.Y., Wang C.L., Zhao H.P., Mi Y., Liang L.Y., Fu Q., Wu M.H., Lei Y.*,'Highly ordered three-dimensional Ni-TiO_2 nanoarrays as sodium ion battery anodes', **Chemistry of Materials** (IF 8.354), 27, 4274-4280, 2015.
6. Zhao H.P., Zhou M., Wen L.Y., Lei Y.*, 'Template-Directed Construction of Nanostructure Arrays for Highly-Efficient Energy Storage and Conversion', **Nano Energy** (IF 10.325), 13, 790-813, 2015.
7. Liang L.Y., Xu Y., Wang C.L., Wen L.Y., Fang Y.G., Mi Y., Zhou M., Zhao H.P., Lei Y.*, 'Large-scale Highly Ordered Sb Nanorod Arrays Anode with High Capacity and Rate Capability for Sodium-Ion Batteries', **Energy & Environmental Science** (IF 20.523), in press, DOI: 10.1039/C5EE00878F, 2015.
8. Mi Y., Wen L.Y., Zhao H.P., Zhou Y.L., Grote F., Lei Y.*, 'Ultra-low mass loading of platinum nanoparticles on bacterial cellulose derived carbon nanofibers for efficient hydrogen evolution', **Catalysis Today** (IF 3.893), in press doi:10.1016/j.cattod.2015.08.019, 2015.

9. Chi D., Lu S.D., Xu R., Liu K., Cao D.W., Wen L.Y., Mi Y., Wang Z.J.*, Lei Y.*, Qu S.C.*, Wang Z.G., 'Fully understanding the positive roles of plasmonic nanoparticles in ameliorating the efficiency of organic solar cells', **Nanoscale** (IF 7.394), in press, DOI: 10.1039/C5NR04069H, 2015.
10. Wen L.Y., Mi Y., Wang C.L., Fang Y.G., Grote F., Zhao H.P., Zhou M., Lei Y.*, 'Cost-effective atomic layer deposition synthesis of Pt nanotube arrays: application for high performance supercapacitor', **Small** (IF 8.368), 10, 3162–3168, 2014 (It was reported by MaterialsViewsChina as the hot article. http://www.materialsviewschina.com/2014/08/yuan-zi-ceng-chen-ji-ji-shu-zhi-bei-gui-jin-shu-fu-za-na-mi-jie-gou-qu-de-jin-zhan-di-jia-gao-xiao-pt-na-mi-guan-he-cheng-ji-qi-ying-yong/).
11. Grote F., Wen L.Y., Lei Y.*, 'Nano-engineering of three-dimensional core/shell nanotube arrays for high performance supercapacitors', **Journal of Power Sources** (IF 6.217), 256, 37-42, 2014.
12. Mi Y., Zhou M., Wen L.Y., H.P. Zhao, Lei Y.*, 'High Efficient Visible-Light Driven Photocatalyst: Two Dimensional Square-like Bismuth Oxyiodine Nanosheets', **Dalton Transactions** (IF 4.197), 43, 9549–9556, 2014.
13. Wang C.L., Fang Y.G., Wen L.Y., Zhou M., Xu Y., Zhao H.P., De Cola L.*, Hu W.P.*, Lei Y.*, 'Vectorial diffusion for facile solution-processed self-assembly of insoluble semiconductors: a case study on metal phthalocyanines', **Chemistry - A European Journal** (IF 5.731), 20, 10990-10995, 2014.
14. Cao D.W., Wang Z.J. , Nasori, Wen L.Y., Mi Y., Lei Y.*, 'Switchable Charge-Transfer in the Photoelectrochemical Energy-Conversion Process of Ferroelectric $BiFeO_3$ Photoelectrodes', **Angewandte Chemie International Edition** (IF 11.261), 126, 11207-11211, 2014.
15. Zhou M., Bao J., Xu Y., Zhang J.J., Xie J.F., Guan M.L., Wang C.L., Wen L.Y., Lei Y.*, Xie Y.*, 'Photoelectrodes Based Upon Mo:$BiVO_4$ Inverse Opals for Photoelectrochemical Water Splitting', **ACS Nano** (IF 12.881), 8, 7088–7098, 2014
16. Wang C.L., Wen L.Y., Kups T., Mi Y., Vellacheri R., Fang Y.G., Schaaf P., Zhao H.P., Lei Y.*, 'Growth control of AgTCNQ nanowire arrays by using a template-assisted electro-deposition method', **Journal of Materials Chemistry C** (IF 4.696) (backside cover paper), 1, 8003-8006, 2013 (was selected as the inside cover).

17. Wong K.M., Fang Y.G., Devaux A., Wen L.Y., Huang J., De Cola L., Lei Y*., 'Assorted analytical and spectroscopic techniques for the optimization of the defect-related properties in size-controlled ZnO nanowires', **Nanoscale** (IF 7.394), 3, 4830-4839, 2011.
18. Wen L.Y., Wong K.M., Fang Y.G., Wu M.H., Lei Y.*, 'Fabrication and characterization of well-aligned, high density ZnO nanowire arrays and their realizations in Schottky device applications using a two-step approach', **Journal of Materials Chemistry** (IF 6.626), 21, 7090-7097, 2011 (It was selected as one of the hot articles in RSC bolg. http://blogs.rsc.org/jm/2011/05/10/hot-articles-on-nanowire-arrays-for-schottky-diodes-an-anticancer-bio-conjugate-and-a-flower-like-sensor/).
19. Wen L.Y., Shao Z.Z., Fang Y.G., Wong K.M., Lei Y.*, Bian L.F.*, Wilde G., 'Selective growth and piezoelectric propriety of vertical ZnO nanowires on the ultra-thin alumina membranes', **Applied Physics Letters** (IF 3.302), 97, 053106, 2010.
20. Wu M.H., Wen L.Y., Lei Y.*, Ostendorp S., Chen K., Wilde G., 'UTAM surface nano-patterning in fabricating quantum-sized nanodots', **Small** (IF 8.368), 6, 695-699, 2010 (It was selected as the inside cover).
21. Shao Z.Z.*, Wen L.Y., Wu D.M., Zhang X.A., Chang S.L., Qin S.L., 'Influence of carrier concentration on piezoelectric potential in a bent ZnO nanorod', **Journal of Applied Physics** (IF 2.183), 108, 124312, 2010.
22. Shao Z.Z.*, Wen L.Y., Wu D.M., Wang X.F., Zhang X.A., Chang S.L., 'A continuum model of piezoelectric potential generated in a bent ZnO nanorod', **Journal of Physics D-Applied Physics**, 43, 245403, 2010.
23. Shao Z.Z.*, Wen L.Y., Wu D.M., Zhang X.A., Chang S.L., Qin S.L., 'AFM analysis of piezoelectric nanogenerator based on n(+)-diamond/n-ZnO heterojunction', **Applied Surface Science**, 257 (11), 4919-4922, 2011.
24. Shao Z.Z.*, Wen L.Y., Wu D.M., Zhang X.A., Chang S.L., Qin S.L., 'Pt/ZnO Schottky nano-contact for piezoelectric nanogenerator', **Physica E-Low-Dimensional Systems & Nanostructures**, 43, 173-175, 2010.

Unpublished manuscripts

1. Wen L.Y., Xu R., Yan M., Lei Y.*, 'Building arbitrary binary nanostructure arrays with anodic aluminum oxide template', submitted to Nature Nanotechnology.

2. Yan M.,[+] Wen L.Y.,[+] Wang Z.J., Xu Y., Cao D.W., Xu R., Fang Y.G., Zhou Y.L., Lei Y.*, 'Two-dimensional Fe:BiOCl ultrathin nanosheet: Surface doping of Fenton reagent for high efficient photocatalysis', ([+]contributed equally), submitted to Nano Energy.

Conference contribution

1. Wen L.Y., Lei Y., 'Building ordered binary nanostructures with pre-patterned alumina template', the 2st International Conference & 4rd International MacroNano-Colloquium on the Challenges and Perspectives of Functional Nanostructures (CPFN), July 30-31, 2015, Ilmenau, Germany. **Talk.**
2. Wen L.Y., Lei Y., 'Large scale ordered binary nanopatterns via pre-patterned anodic aluminum oxide', 78th, Annual Conference of the DPG, Mar 31- April 4, 2014, Dresden, Germany. **Talk**.
3. Wen L.Y., Lei Y., 'Building Ordered Binary Nanostructures with Pre-patterned Alumina Template', the 1st International Conference & 3rd International MacroNano-Colloquium on the Challenges and Perspectives of Functional Nanostructures (CPFN), July 30-31, 2014, Ilmenau, Germany. **Talk.**
4. Grote F., Wen L.Y., Lei Y., 'Realizing Three-Dimensional Nanostructures Using Nano-Templates: Concept, Properties and High Performance Devices', 77th Annual Conference of the DPG, March 10-15, 2013, Regensburg, Germany. **Talk.**
5. Wen L.Y., Lei Y., 'Nano-engineered three-dimensional Pt/MnO_2 thin films for flexible, high performance supercapacitors', 77th Annual Conference of the DPG, Mar 10-15, 2013, Regensburg, Germany. **Talk.**
6. Wen L.Y., Lei Y., 'Template-Based Surface Nano-Patterning and device applications', IMAPS/ACerS 8th International Conference and Exhibition on Ceramic Interconnect and Ceramic Microsystems Technologies (CICMT 2012), April 16-19, 2012, Erfurt, Germany. **Talk and Conference Proceeding.**
7. Wen L.Y., Lei Y., 'Template-based surface nano-patterning to realize high performance devices', 76th Annual Conference of the DPG, Mar 25-30, 2012, Berlin, Germany.**Talk.**
8. Wong K.M., Wen L.Y., Fang Y.G., Grote F., Sun H., Lei Y., 'Fabrication and Characterization of Well-Aligned Zinc Oxide Nanowire Arrays and their realizations in Schottky-Device Applications', 75th Annual Conference of the DPG, March 13-18, 2011, Dresden, Germany. **Talk.**

9. Zhao H.P., Grote F., Wen L.Y., Lei Y., 'Anodic Aluminum Oxide (AAO) Template directed Nanostructure Arrays towards High-Performance Supercapacitor Devices', the 2st International Conference & 4rd International MacroNano-Colloquium on the Challenges and Perspectives of Functional Nanostructures (CPFN), July 30-31, 2015, Ilmenau, Germany. **Poster.**
10. Zhao H.P., Wen L.Y., Lei Y., 'Ideally Ordered Anodic Aluminum Oxide (AAO) Template: Preparation and Application', the 1st International Conference & 3rd International MacroNano-Colloquium on the Challenges and Perspectives of Functional Nanostructures (CPFN), July 30-31, 2014, Ilmenau, Germany. **Poster.**
11. Grote F., Wen L.Y., Lei Y., 'Template-assisted fabrication of self-supported 3D functional nanostructure arrays towards high performance devices', Mikro-Nano-Integration - Beiträge des 5. GMM-Workshops, 09/08/2014 - 10/09/2014, Ilmenau. **Conference Proceeding.**

Declaration

I hereby declare that this Ph.D. dissertation entitled “Binary Nano-structuring: Concept, Strategies, Features and Devices” was carried out by me for the degree of Doctor of Philosophy under the supervision of Prof. Dr. Yong Lei. All dates or information in this dissertation that have been directly or indirectly consulted or used from other sources are clearly stated. This dissertation has not been submitted, in part or in whole, for any other degree or examination in any other University. I have acknowledged all main sources of help, and I have made clear exactly what was done by others and what I have contributed when the work was done jointly with others. Some of the results may have been published in scientific journals or elsewhere. I am aware that the falsity of this declaration will be regarded as an attempt of deception and will cause the derogation of the doctoral procedure.

Ilmenau, 20. October. 2015

Liaoyong Wen